# The fate of pyruvate dictates cell growth by modulating cellular redox potential

Ashish G. Toshniwal[1], Geanette Lam[1], Alex J. Bott[1], Ahmad A. Cluntun[1, 5], Rachel Skabelund[1], Hyuck-Jin Nam[2], Dona R. Wisidagama[2], Carl S. Thummel[2] and Jared Rutter[1, 3, 4]

**Affiliations:**

[1] Department of Biochemistry, University of Utah, Salt Lake City, UT 84132, USA

[2] Department of Human Genetics, University of Utah, Salt Lake City, UT 84132, USA

[3] Howard Hughes Medical Institute, University of Utah School of Medicine, Salt Lake City, UT 84132, USA

[4] Lead Contact

[5] Present address: Department of Biochemistry & Molecular Biology, Rutgers Robert Wood Johnson Medical School, Piscataway, NJ 08854

## Abstract

Pyruvate occupies a central node in carbohydrate metabolism such that how it is produced and consumed can optimize a cell for energy production or biosynthetic capacity. This has been primarily studied in proliferating cells, but observations from the post-mitotic *Drosophila* fat body led us to hypothesize that pyruvate fate might dictate the rapid cell growth observed in this organ during development. Indeed, we demonstrate that augmented mitochondrial pyruvate import prevented cell growth in fat body cells *in vivo* as well as in cultured mammalian hepatocytes and human hepatocyte-derived cells *in vitro*. This effect on cell size was caused by an increase in the $NADH/NAD^+$ ratio, which rewired metabolism toward gluconeogenesis and suppressed the biomass-supporting glycolytic pathway. Amino acid synthesis was decreased, and the resulting loss of protein synthesis prevented cell growth. Surprisingly, this all occurred in the face of activated pro-growth signaling pathways, including mTORC1, Myc, and PI3K/Akt. These observations highlight the evolutionarily conserved role of pyruvate metabolism in setting the balance between energy extraction and biomass production in specialized post-mitotic cells.

## Introduction

Cells must appropriately allocate available nutrients to optimize their metabolic programs— for energy extraction and for the generation of building blocks that enable cell growth.

The balance between these processes not only maintains cellular health under varying nutritional conditions but also plays an important role in determining cell fate and function (Baker & Rutter, 2023; DeBerardinis & Thompson, 2012; Ghosh-Choudhary et al., 2020; Metallo & Vander Heiden, 2013). For example, hepatocyte metabolism changes considerably between fed and fasted conditions. In the fed state, hepatocytes use the majority of their nutrients to synthesize proteins, lipids, and glycogen, which results in increased cell size and liver biomass (Kast et al., 1988; Reinke & Asher, 2018; Sinturel et al., 2017). To meet the energy demands of other tissues during fasting, the liver undergoes a metabolic shift to produce glucose from biosynthetic precursors, thereby decreasing hepatocyte and liver size (Lang et al., 1998; Sinturel et al., 2017).

The metabolic pathways that support biosynthetic metabolism can be inappropriately activated in diseases such as cancer and heart failure to promote pathological growth. For example, many of the primary oncogenic adaptations in tumors prioritize anabolic metabolism over ATP production, which facilitates rapid cell proliferation (Lunt & Vander Heiden, 2011; Vander Heiden et al., 2009; Zhu & Thompson, 2019). Metabolic rewiring during heart failure similarly results in greater biosynthetic potential and less efficient ATP production, which in post-mitotic cardiomyocytes leads to increased cell size and insufficient cardiac pumping (Bornstein et al., 2024; Henry et al., 2024; Weiss et al., 2023).

The fate of pyruvate, which is primarily generated from glucose via glycolysis in the cytoplasm, is a critical node that can determine the balance between energetic and biosynthetic metabolism (Baker & Rutter, 2023; Yiew & Finck, 2022). In most differentiated cells, the majority of pyruvate is transported into the mitochondria via the mitochondrial pyruvate carrier (MPC) complex, a heterodimer composed of MPC1 and MPC2 proteins (Bricker et al., 2012; Herzig et al., 2012). Once in the mitochondria, pyruvate is converted to acetyl-CoA by the pyruvate dehydrogenase complex (PDH), fueling the tricarboxylic acid (TCA) cycle and supporting efficient ATP production. In cancer, stem, and other proliferative cells, more pyruvate is converted to lactate and exported from the cell, a process that regenerates $NAD^+$, a cofactor necessary for glycolytic flux (Baker & Rutter, 2023; Lunt & Vander Heiden, 2011; Zhu & Thompson, 2019). In some specialized cells, including hepatocytes, pyruvate is imported into mitochondria but converted to oxaloacetate, which can feed the TCA cycle but also serves as a precursor for glucose production via gluconeogenesis (Holecek, 2023b; Jitrapakdee et al., 2008). We and others have demonstrated that these alternative fates of pyruvate—energy generation, cell proliferation, or glucose production—differentially impact the metabolic and fate decisions of

65 multiple cell types in varying contexts (Bensard et al., 2020; Cluntun et al., 2021; Wei et al., 2022;
66 Yiew & Finck, 2022). Loss of MPC function, which shifts pyruvate metabolism toward lactate
67 production and thus expedites glycolysis and the production of biosynthetic precursors, has been
68 shown to increase cell proliferation in mouse and *Drosophila* intestinal stem cells as well as in
69 various tumors (Bensard et al., 2020; Schell et al., 2017; Zangari et al., 2020). MPC expression
70 is also reduced in human and mouse models of heart failure, and genetic deletion of the MPC in
71 cardiomyocytes is sufficient to induce hypertrophy and heart failure (Cluntun et al., 2021;
72 Fernandez-Caggiano et al., 2020; McCommis et al., 2020; Zhang et al., 2020). Conversely, MPC
73 overactivation or overexpression restricts intestinal stem cell proliferation and limits the growth of
74 cardiomyocytes under hypertrophic stimuli, with excess mitochondrial pyruvate fueling the TCA
75 cycle (Bensard et al., 2020; Schell et al., 2014; Schell et al., 2017). These observations suggest
76 that mitochondrial pyruvate metabolism is central to cell proliferation as well as the size and
77 specialized functions of post-mitotic cells.

78 The mechanisms regulating cell size include well-characterized cellular signaling
79 pathways and transcriptional programs (Grewal, 2009; Liu et al., 2022; Lloyd, 2013). The CDK4-
80 Rb pathway monitors cell size in proliferating cells by coupling cell growth with cell division
81 (Amodeo & Skotheim, 2016; Ginzberg et al., 2018; Tan et al., 2021; Zhang et al., 2022). In
82 response to insulin and other growth factors, the PI3K/Akt pathway activates mTORC1, leading
83 to increased biosynthesis of proteins, lipids, and nucleotides, and consequently, increased cell
84 size (Gonzalez & Hall, 2017; Gonzalez & Rallis, 2017; Saxton & Sabatini, 2017). The pro-growth
85 transcription factor Myc drives a gene expression program that enhances metabolic activity and
86 protein synthesis, resulting in larger cells (Baena et al., 2005; Dang, 1999; Iritani & Eisenman,
87 1999; Stine et al., 2015; van Riggelen et al., 2010). However, we only partially understand how
88 metabolic pathways regulate physiological (or pathophysiological) growth, particularly in cells that
89 have distinct and specialized roles in organismal metabolism.

90 Here, we investigated whether pyruvate metabolism influences biosynthetic capacity and
91 cell size, using the *Drosophila* fat body as a model of the mammalian liver. We found that MPC
92 overexpression and increased mitochondrial pyruvate transport restrict cell growth and limit
93 protein synthesis in larval fat body cells and in spheroids of human liver-derived cells. Higher MPC
94 expression resulted in smaller cells, not by increasing TCA cycle flux as observed in other cell
95 types, but instead by redirecting mitochondrial pyruvate metabolism towards gluconeogenesis. A
96 key driver of this metabolic rewiring is a reduced cellular redox state, which disrupts the
97 biosynthesis of TCA cycle-derived amino acids, such as aspartate and glutamate, ultimately

98 reducing protein synthesis. These observations highlight how cells with specialized functions, like
99 hepatocytes, employ distinct metabolic adaptations to respond to organismal demands under
100 varying nutritional conditions.
101

## 102 Results

### 103 Increased mitochondrial pyruvate transport reduces the size of *Drosophila* fat body cells

104 The *Drosophila* fat body is functionally analogous to mammalian white adipose tissue and
105 liver, serving as a buffer to store excess nutrients in fat droplets and glycogen and deploy them
106 to support the animal with fuel during times of fasting (Arrese & Soulages, 2010; Musselman et
107 al., 2013). During larval development, fat body cells halt cell division and dramatically increase in
108 size during the third instar stage (from 72 to 120 hours After Egg Laying (AEL)) (Edgar & Orr-
109 Weaver, 2001; Zheng et al., 2016) (Fig. 1a-c). As a first step to understand the metabolic
110 programs that enables this rapid cell growth, we performed RNA-sequencing of the *Drosophila*
111 fat body across this developmental period. We observed a time-dependent change in mRNAs
112 encoding proteins that have well-characterized roles in supporting cell growth, including
113 components of the insulin and mTORC1 signaling pathways and the Myc transcriptional network
114 which correlated with increased cell size (Supplementary Fig. 1a). Amongst metabolic genes, we
115 observed modest differences in those that function in amino acid synthesis and fatty acid
116 metabolism (Supplementary Fig. 1b). The abundances of mRNAs encoding proteins involved in
117 glycolysis, oxidative phosphorylation (OxPhos), and the TCA cycle were distinctly altered in fat
118 bodies during development (Supplementary Fig. 1b). Since pyruvate metabolism is the central
119 node connecting carbohydrate metabolism and the TCA cycle, we studied the abundances of
120 mRNAs that encode proteins that regulate pyruvate metabolism (Fig. 1d). We found that the
121 expression of genes that link pyruvate to the TCA cycle were reduced including, *Pyk,* the
122 *Drosophila* pyruvate kinase homolog, which converts phosphoenolpyruvate into pyruvate; *Mpc1*
123 and *Mpc2,* which encode the two subunits of the MPC, which transports pyruvate into the
124 mitochondrial matrix; as well as *Pdha* and *Dlat,* which encode subunits of PDH complex (Fig. 1e).
125 In contrast, some mRNAs encoding proteins that regulate pyruvate abundance were upregulated
126 such as *Pepck* and *Pepck2*, which make phosphoenolpyruvate from oxaloacetate
127 (Supplementary Fig. 1c). Based on these data, we hypothesized that the suppression of
128 mitochondrial pyruvate metabolism, which is gated by the action of the MPC, might support the
129 rapid cell growth observed in fat body cells.

130 To test this hypothesis, we prevented the downregulation of the MPC during larval
131 development (Fig. 1e) by ectopically expressing *Mpc1* and *Mpc2* (termed "MPC+" Supplementary
132 Fig. 2a, 2b). The sustained expression of the MPC (both *Mpc1* and *Mpc2*) throughout the fat body
133 significantly reduced the rate of cell growth compared to a GFP-expressing control
134 (Supplementary Fig. 2c). Given the important role of the fat body in controlling organismal growth,
135 we wanted to assess the cell-autonomous effects of MPC expression using mosaic analysis in
136 individual fat body cells (Supplementary Fig. 2d) (Ito et al., 1997). We generated GFP-labeled
137 clones with expression of the MPC (MPC+), which we confirmed by immunofluorescence
138 (Supplementary Fig. 2e, f). The MPC-expressing, GFP-positive cells were significantly smaller in
139 size compared with either mock clones (control) or neighboring GFP-negative cells within the
140 same tissue. *Mpc1* knock down (*Mpc1*-KD) clones, in contrast, were marginally larger (Fig. 1f-g).
141 These results demonstrate that sustained expression of the MPC in developing fat body cells is
142 sufficient to prevent cell growth in a cell-autonomous manner.
143 If the effects of MPC expression were related to the mitochondrial transport of pyruvate,
144 then limiting the production of pyruvate should mitigate these effects. Therefore, we measured
145 cell size in larvae raised on either a normal (9% sugar) diet or a diet with no added sugars, which
146 limits the production of pyruvate from glucose and fructose. Limiting dietary sugars significantly
147 reduced the size of control clones but increased the size of MPC-expressing clones. Notably, the
148 size of MPC-expressing fat body clones was comparable to that of control clones when larvae
149 were grown in sugar-limited medium, suggesting that limiting pyruvate synthesis abolishes the
150 effect of MPC expression on fat body cell size (Fig. 1h, i). *Mpc1*-KD clones were again larger than
151 control cells and their size was unaffected by the sugar-limited diet. Inhibiting MPC activity by
152 feeding larvae a normal diet supplemented with the MPC inhibitor UK5099 ameliorated the cell
153 size effects of MPC expression (Fig. 1j and Supplementary Fig. 2g). These results indicate that
154 pyruvate transport into mitochondria inversely correlates with the size gain in fat body cells. These
155 observations also suggest that the suppression of mitochondrial pyruvate import, and metabolism
156 is required for the rapid cell size expansion observed in the fat body during larval development.
157 The size of a cell is determined by its content of proteins, nucleic acids, and lipids
158 (Bjorklund, 2019; Lloyd, 2013; Schmoller & Skotheim, 2015). To understand how MPC expression
159 affects the abundance of these macromolecules, we dissected fat bodies from control and fat
160 body-wide MPC-expressing larvae at 120 hours AEL and quantified DNA, RNA, triacylgylcerides,
161 and protein. Control and MPC+ fat bodies had equivalent DNA content (Fig. 1k, Supplementary
162 Fig. 2h) and similar levels of EdU incorporation (Supplementary Fig 2o, p), suggesting that MPC

163 expression does not impact DNA endoreplication. RNA and lipid content were modestly
164 decreased in MPC+ fat bodies compared with control tissues (Fig. 1k, Supplementary Fig. 2i, j),
165 although the number of lipid droplets was higher with MPC expression (Supplementary Fig 2l-n).
166 In contrast, MPC expression dramatically decreased protein abundance in fat bodies (Fig. 1k,
167 Supplementary Fig. 2k), and reduced protein synthesis as assessed by staining for the puromycin
168 analog, O-propargyl-puromycin (OPP) (Deliu et al., 2017; Villalobos-Cantor et al., 2023) (Fig. 1l,
169 m). These data suggest that MPC-mediated mitochondrial pyruvate import decreases protein
170 synthesis, which likely contributes to the reduced size of MPC-expressing cells. Conversely, in
171 developing fly larvae, repression of the MPC and the subsequent decrease in mitochondrial
172 pyruvate appear to provide a metabolic mechanism to support a rapid expansion in cell size.
173

174 **Growth factor signaling pathways are hyperactivated in MPC expressing cells**

175 The best understood mechanisms that govern cell size involve conserved signaling and
176 transcriptional networks (Bjorklund, 2019; Grewal, 2009; Lang et al., 1998; Lloyd, 2013). For
177 example, the mTORC1 pathway coordinates both extracellular and intracellular growth regulatory
178 signals to dictate the synthesis and degradation of macromolecules, including proteins, lipids, and
179 nucleic acids (Gonzalez & Hall, 2017; Gonzalez & Rallis, 2017; Saxton & Sabatini, 2017).
180 mTORC1 increases protein synthesis through the phosphorylation of several proteins, including
181 S6 kinase (S6K) and 4EBP1 (Fig. 2a). Since MPC-expressing clones were smaller in size and
182 had reduced protein synthesis compared with control clones, we assessed mTORC1 activity in
183 the fat body using our mosaic expression system. As a control, we confirmed that *S6k* (the
184 *Drosophila* gene encoding S6K) over-expressing clones were larger in size and had elevated
185 phospho-S6 staining compared with wild-type clones (Fig. 2b, c). Surprisingly, MPC+ clones also
186 had elevated phospho-S6 staining (Fig. 2b, c), suggesting that despite their small size, these cells
187 have high mTORC1 activity. Over-expression of *Rheb*, which is an upstream activator of
188 mTORC1, resulted in clones that were larger than wild-type controls and which had increased
189 phospho-4EBP1 staining (Fig. 2d, e). Again, even though the MPC+ clones were smaller in size,
190 we observed robust p-4EBP1 staining, indicating that mTORC1 is hyperactive in these cells.

191 Gene set enrichment analysis of RNA-sequencing data from MPC-expressing fat bodies
192 showed enrichment for signatures associated with pro-growth signaling (Supplementary Fig. 3a).
193 We assessed markers of several of these pathways in MPC+ clones. In addition to the mTORC1
194 pathway, Myc increases cell growth by regulating the transcription of ribosome subunits and
195 biosynthetic metabolic genes. We found that MPC+ clones had an elevated abundance of the

196 Myc protein, both in the cytoplasm and nucleus, (Fig. 2f, g), suggesting that the growth-promoting
197 Myc transcriptional program is active in these cells. MPC+ clones also had reduced expression
198 of the transcription factor Foxo, consistent with its downregulation by pro-growth signaling
199 pathways (Supplementary Fig. 3b). Finally, we stained for phospho-eIF2$\alpha$ to assess the activity
200 of the integrated stress response, which restricts global protein synthesis. Starvation robustly
201 induced the integrated stress response in control clones, but MPC+ clones exhibited no evidence
202 of activation of this pathway under normal growth conditions (Fig. 2h, i). Collectively these data
203 indicate that conventional pro-growth pathways are activated in MPC-expressing clones, which is
204 incongruent with the small size of the clones. This suggests that mitochondrial pyruvate
205 metabolism controls cell size via alternative molecular mechanisms.
206 We next performed genetic epistasis analysis to better understand the relationship
207 between MPC expression and the mTORC1, PI3K, and Myc pathways. Activation of the PI3K or
208 mTORC1 pathways, via over-expression of *PI3K*, increased the size of control but not MPC-
209 expressing fat body cells (Supplementary Fig. 3c). Similarly, activation of mTORC1 via knock
210 down of its inhibitor, Tuberous Sclerosis Complex 1 (*Tsc1*), increased the size of control cells but
211 had no effect on MPC+ cell size (Supplementary Fig. 3d). Over-expression of *Myc*, on the other
212 hand, increased the size of control and MPC+ fat body clones to a similar degree (Supplementary
213 Fig. 3e). Knock down of *Myc* was sufficient to decrease cell size to a similar extent as MPC
214 expression; however, *Myc* knock down had no additional effect on cell size in MPC+ clones
215 (Supplementary Fig. 3f). These results suggest that neither mTORC1, PI3K, nor Myc are epistatic
216 to MPC and suggest that MPC likely acts independently of these canonical pathways to regulate
217 the size of fat body cells.
218
219 **Increased mitochondrial pyruvate transport reduces the size of HepG2 cells and spheroids**
220 Since the *Drosophila* fat body has many features reminiscent of the mammalian liver, we
221 tested whether MPC expression might similarly restrict cell size in cells derived from this tissue.
222 We engineered HepG2 cells, which were originally isolated from a hepatocellular carcinoma, to
223 express epitope tagged-MPC1 and MPC2 in a doxycycline-inducible manner. We observed
224 expression of ectopic MPC1 and MPC2 starting at four hours after doxycycline treatment, which
225 increased over the duration of the time course, peaking at 24 hours post-induction (Fig. 3a). We
226 stained doxycycline-treated cells with phalloidin and measured cell size using microscopy images
227 taken at two-hour intervals. Induction of MPC expression coincided with a significant reduction in
228 cell size, which was first apparent six hours post-doxycycline treatment and was sustained for the

229 remainder of the time course (Fig. 3b). Doxycycline had no effect on the size of control HepG2
230 cells (EV). Treatment with the MPC inhibitor UK5099 for 24 hours markedly increased the size of
231 control cells and partially reversed the small size phenotype of MPC-expressing cells (Fig. 3c).
232 We also assessed cell volume by analyzing a 3D reconstruction of confocal images of phalloidin-
233 stained HepG2 cells and found that the cell volume was lower in MPC+ cells (Supplementary Fig.
234 4a).

235 We have observed that the physiological consequences of altered pyruvate metabolism
236 are more apparent in cells grown in a three-dimensional culture environment (Schell et al., 2014;
237 Wei et al., 2022). Using our doxycycline-inducible cells, we found that MPC expression resulted
238 in spheroids that were significantly smaller than control spheroids as assessed by microscopy
239 (Fig. 3d, e). Cells from MPC-expressing spheroids were also smaller as shown by flow cytometry
240 (Fig. 3f, g). When compared with control (EV) spheroids, expression of MPC had no effect on the
241 number of cells per spheroid, on the cell cycle phase distribution, or on the number of apoptotic
242 or necrotic cells (Supplementary Fig. 4b, 4c, and 4d). These analyses suggest that the smaller
243 size observed in MPC expressing spheroids is not due to effects on cell proliferation or cell death.

244 Consistent with our observations in the *Drosophila* fat body, protein content was lower in
245 MPC-expressing HepG2 spheroids compared with EV controls, whereas there was no difference
246 in the abundances of DNA, RNA, or triacylgylcerides (Fig. 3h and Supplementary Fig. 4e-h). To
247 directly assess the effect of MPC expression on protein synthesis, we induced the MPC in HepG2
248 cells and treated cells acutely with a low concentration of puromycin to label nascent proteins.
249 We found that MPC expression decreased the incorporation of the amino acid analog L-
250 homopropargylglycine (HPG) (Shen et al., 2021; Tom Dieck et al., 2012) into nascent proteins,
251 as assessed by fluorescence microscopy (Fig. 3i, j). Protein synthesis was similarly reduced in
252 MPC-expressing HepG2 spheroids (Fig. 3k, l). These observations were further supported by the
253 decreased abundance of the short-lived, destabilized GFP (d2GFP) (Li et al., 1998; Pavlova et
254 al., 2020) in MPC-expressing HepG2 spheroids compared with controls. This reduction in the
255 level of d2GFP was prevented by treatment with the MPC inhibitor UK5099 (Fig. 3m). Together
256 these data suggest that increased transport of pyruvate into mitochondria, mediated by MPC
257 expression, reduces protein synthesis and cell size in both fly and mammalian models.

258

259 **Excess mitochondrial pyruvate promotes gluconeogenesis**

260 We have previously shown that loss of the MPC reduces the contribution of glucose and
261 pyruvate to the TCA cycle (Bensard et al., 2020; Cluntun et al., 2021). To investigate how MPC

262 expression impacts carbohydrate metabolism in HepG2 cells, we performed metabolic tracing
263 using $^{13}$C-glucose (Fig. 4a). We observed that MPC expression reduced the labeling fraction of
264 the glycolytic intermediates 3-phosphoglycerate (Supplementary Fig. 5a) and pyruvate
265 (Supplementary Fig. 5b), as well as alanine (Supplementary Fig. 5c), which is derived from
266 pyruvate, all of which suggests a reduction in glycolysis in these cells. Once imported into
267 mitochondria, glycolytic-derived pyruvate has two major fates: conversion to acetyl-CoA by PDH
268 or to oxaloacetate by pyruvate carboxylase (PC). These fates can be differentiated by assessing
269 the abundances of M+2 (derived from PDH) and M+3 (derived from PC) TCA cycle intermediates
270 (Fig. 4a). We found that both M+2 and M+3 isotopomers of TCA cycle intermediates were
271 modestly increased following MPC expression (Fig. 4b and 4c; Supplementary Fig. 5d-g). The
272 fact that we observe increases in TCA cycle intermediates despite decreased glycolytic labeling
273 in pyruvate suggests that the apparent labeling through PDH and PC might be underestimating
274 the effect on metabolic flux through these enzymes. Thus, it appears that MPC expression
275 increases the activity of both enzymes that utilize pyruvate. Typically, when TCA cycle flux is
276 increased, one observes an increase in activity of the electron transport chain (ETC) to oxidize
277 the resulting NADH. However, MPC expression had no impact on ETC activity as assessed by
278 measuring oxygen consumption (Fig. 4d). The implications of elevated NADH production without
279 a concomitant increase in NADH oxidation will be discussed in Fig. 5.
280 To probe the impact of increased flux through the PC and PDH reactions, we conducted
281 genetic epistatic analysis in fat body cells. We found that *Drosophila* fat body clones in which we
282 over-expressed *Pcb* (the *Drosophila* gene encoding pyruvate carboxylase) were significantly
283 smaller than controls and were equivalent in size to MPC+ clones (Fig. 4e, f). Clones expressing
284 both the MPC and *Pcb* were even smaller (Fig. 4e, f). Conversely, knock down of *Pcb* (*Pcb*-KD)
285 in MPC-expressing fat body clones completely rescued the cell size phenotype (Fig. 4e, f and
286 Supplementary Fig. 6a). Knock down of *Pcb* in MPC-expressing HepG2 cells also eliminated the
287 small cell size phenotype (Supplementary Fig. 6b). These data suggested that the small size of
288 cells expressing the MPC is likely due to increased flux through the PC reaction. Consistent with
289 this, knock down of the PDH-E1 (*Drosophila* gene *Pdha*) or PDH-E2 (*Drosophila* gene *Dlat*)
290 subunits of PDH, which should divert mitochondrial pyruvate, so it is preferentially used by PC,
291 also resulted in smaller fat body cells (Supplementary Fig. 6c-d). In contrast, activating PDH by
292 knocking down the inhibitory PDH kinases (mammalian PDKs, *Drosophila* gene *Pdk*) (Stacpoole,
293 2017; Wang et al., 2021), which should promote the flux of pyruvate through PDH and away from
294 PC, rescued cell size in MPC-expressing fat body clones (Supplementary Fig. 6c, d). Similarly, in

295 MPC-expressing HepG2 cells, activation of PDH via treatment with the PDK inhibitors DCA and
296 AZD7545 was sufficient to restore cell size (Supplementary Fig. 6e) (Stacpoole, 2017; Wang et
297 al., 2021). These analyses suggest that the reduction in cell size observed with MPC expression
298 is due to PC-mediated metabolism of pyruvate.

299 The product of PC, oxaloacetate, has three major metabolic fates: 1) feeding the TCA
300 cycle via citrate synthase as discussed above, 2) conversion to aspartate by glutamatic-
301 oxaloacetic transaminase 2 (GOT2), and 3) conversion to phosphoenolpyruvate by PEPCK2
302 leading to gluconeogenesis, synthesis of glucose (Jitrapakdee et al., 2008; Kiesel et al., 2021).
303 Sustained expression of the MPC in fat bodies increased the concentration of glucose in this
304 tissue (Fig. 4g) as well as in larval circulation (known as hemolymph) (Fig. 4h), suggesting that
305 MPC expression increases glucose production in fat body cells. Next, we tested whether
306 PEPCK2-mediated gluconeogenesis was elevated in these cells compared with controls. We
307 used $^{13}$C-lactate to trace the $^{13}$C-labeling of phosphoenolpyruvate and resultant glucose synthesis
308 via gluconeogenesis (Fig. 4i). We found that the relative abundance of M+3 phosphoenolpyruvate
309 was higher in MPC-expressing cells compared with controls (Fig. 4j), suggesting increased
310 activity of PEPCK2. The gluconeogenic pathway employs a series of biochemical reactions to
311 convert phosphoenolpyruvate into glucose, which is then excreted from the cell. This production
312 of M+6 glucose from lactate was also higher in MPC-expressing HepG2 cells (Fig. 4k). To test
313 whether gluconeogenesis contributes to the small size phenotype of MPC-expressing cells, we
314 knocked down enzymes in the pathway (*Drosophila* phosphoenol carboxykinase, *Pepck2,* and
315 fructose bisphosphatase, *Fbp*) and assessed cell size in *Drosophila* and HepG2 models.
316 Knockout of PEPCK2 in MPC-expressing HepG2 cells resulted in smaller spheroids (Fig. 4l) and
317 cells (Supplementary Fig. 6f). Knock down of either *Pepck2* or *Fbp* partially rescued the size
318 defect in MPC-expressing *Drosophila* fat body clones (Fig. 4n, o Supplementary Fig. 6g), and
319 *Pepck2* knock down also increased protein synthesis in these clones (Fig. 4p, q). Collectively,
320 these data suggest that the cell size and protein synthesis phenotypes observed in MPC-
321 expressing cells require PC-mediated gluconeogenesis, and this relationship is found in both the
322 *Drosophila* fat body and in HepG2 cells.
323

324 **A redox imbalance impairs protein synthesis and cell growth in MPC-expressing cells**

325 We were intrigued by the observation that MPC expression exerted its impact on cell size
326 through PC and not via increased flux through PDH. We did not observe any differences in the
327 abundances of PDH1a, phosphorylated (inactive) PDH1a, PC, PEPCK2, or G6PC proteins in

328 MPC-expressing HepG2 cells (Supplementary Fig. 7a, b). We therefore hypothesized that the
329 shift in pyruvate metabolism in response to MPC expression might be driven by changes in the
330 abundances of enzyme cofactors, metabolite regulators, or cellular redox balance. PC and PDH
331 show reciprocal regulation by such factors: PC utilizes ATP as a substrate and is allosterically
332 activated by acetyl-CoA, whereas PDH is inhibited by ATP, acetyl CoA, and NADH (Chai et al.,
333 2022; Sugden & Holness, 2011) (Supplementary Fig. 7c). In addition, several reactions in
334 gluconeogenesis require ATP or NADH (Hausler et al., 2006; Siess et al., 1977) (Supplementary
335 Fig. 7c). Upon induction of MPC expression in HepG2 cells, we observed increased abundance
336 of acetyl-CoA (Supplementary Fig. 7d), a higher ATP to ADP ratio (Supplementary Fig. 7e), a
337 greater abundance of NADH without an increase in $NAD^+$, and thus an increase in the cellular
338 NADH/$NAD^+$ ratio (Supplementary Fig. 7f-h). To determine how MPC expression impacts the
339 subcellular distribution of redox factors, we separated cytoplasmic and mitochondrial fractions
340 from control or MPC-expressing *Drosophila* fat bodies and measured the NADH/$NAD^+$ ratio. We
341 found that MPC expression increased the NADH/$NAD^+$ ratio in both the cytoplasm and
342 mitochondria (Fig. 5a). We observed a similar increase in the NADH/ $NAD^+$ ratio in both fractions
343 in MPC-expressing HepG2 spheroids (Fig. 5b). These results suggest that the increased
344 abundances of acetyl-CoA, ATP, and NADH in MPC-expressing cells could promote the rewiring
345 of mitochondrial pyruvate metabolism through PC and support gluconeogenesis.

346 To test the hypothesis that ATP or NADH concentrations might affect cell size in MPC-
347 expressing *Drosophila* fat body clones or HepG2 cells, we utilized pharmacological or genetic
348 modulation of these molecules. Treatment with gramicidin, which decreases the ATP to ADP ratio
349 (Xue et al., 2022), did not alter the size of MPC-expressing HepG2 cells (Supplementary Fig. 7i).
350 We used several orthogonal approaches to reduce the cellular NADH/$NAD^+$ ratio in the MPC-
351 expressing systems and measured their effect on cell size. Co-expression of the *Drosophila*
352 nicotinamide mononucleotide adenylyl transferase (*Nmnat)*, which increases $NAD^+$ biosynthesis,
353 almost normalized the small size phenotype of MPC-expressing clones in the *Drosophila* fat body
354 (Fig. 5c, d). We observed a similar rescue of cell size following expression of the *Ciona intestinalis*
355 alternate Complex I enzyme NADH dehydrogenase (NDX) (Gospodaryov et al., 2020) or the yeast
356 NADH dehydrogenase (NDI) (Sanz et al., 2010), both of which oxidize NADH to $NAD^+$ without
357 concomitant proton translocation and energy capture (Fig. 5e, f). Expression of NDI in HepG2
358 cells also mitigated the effect of MPC expression on spheroid size (Supplementary Fig. 7j, k), as
359 did treatment with duroquinone (Merker et al., 2006) (Supplementary Fig. 7l), which oxidizes
360 NADH to $NAD^+$. To extend these investigations to three dimensional culture, we supplemented

361 the growth medium of MPC-expressing HepG2 spheroids with the $NAD^+$ precursors nicotinamide
362 riboside (NR) or nicotinamide mononucleotide (NMN), both of which recovered spheroid size (Fig.
363 5g, h).
364 Since MPC expression reduced protein synthesis in both *Drosophila* fat bodies and
365 HepG2 cells, we tested how cellular redox status might contribute to this phenotype in both
366 systems. Expression of NDX, which lowers the $NADH/NAD^+$ ratio, increased translation in MPC-
367 expressing *Drosophila* fat body clones (Fig. 5i, j). In HepG2 spheroids, boosting $NAD^+$
368 biosynthesis by supplementing growth media with NR or NMN partially rescued the abundance
369 of destabilized GFP (Fig. 5k). These results suggest that the elevated $NADH/ NAD^+$ ratio in MPC-
370 expressing cells limits protein synthesis and that normalizing that ratio increases protein synthesis
371 and cell size.
372
373 **Reduced amino acid abundance impairs size of MPC-overexpressing cells**
374 Given the reduced protein synthesis observed upon MPC expression, we assessed amino
375 acid concentrations in HepG2 using steady-state metabolomics. We found that MPC expression
376 reduced the abundance of most amino acids (Fig. 6a). To test whether the low abundances of
377 amino acids contribute to the smaller size of MPC-expressing cells, we supplemented the growth
378 media of HepG2 spheroids with excess non-essential amino acid (NEAAs)—either two or three
379 times the recommended dilution of a commercially available amino acid cocktail that includes
380 glycine, L-alanine, L-asparagine, L-aspartate, L-glutamate, L-proline, and L-serine. MPC-
381 expressing spheroids grown with excess NEAAs were comparable in size to controls (Fig. 6b, c).
382 In parallel, we provided *Drosophila* larvae with food containing excess (5x) amino acids from 72
383 to 120 hours AEL, which partially rescued cell size in MPC-expressing fat body clones (Fig. 6d,
384 e). To genetically augment intracellular amino acids, we expressed the amino acid importer
385 *slimfast* (Colombani et al., 2003) in control or MPC-expressing fat body clones and found that it
386 prevented the decrease in cell size (Fig. 6f, g).
387 To determine which amino acid(s) contribute to the cell size effects of MPC expression,
388 we cultured control and MPC-expressing HepG2 cells in media supplemented with an excess of
389 each individual amino acid from the NEAA cocktail. Treatment with excess glycine, L-alanine, or
390 L-serine had no effect on cell size (Fig. 6h). However, the size of MPC-expressing cells was
391 normalized by supplementation with L-aspartate, L-glutamate, or L-proline (Fig. 6h), all of which
392 are derived from TCA cycle intermediates. Supplementation with either L-aspartate or L-
393 glutamate also rescued the small size phenotype of MPC-expressing HepG2 spheroids

394 (Supplementary Fig. 8a, b). Increasing L-aspartate uptake by over-expressing the aspartate
395 transporter SLC1A3 also recovered size of HepG2 spheroids (Supplementary Fig. 8c, d). In
396 addition, treatment with excess (3x) NEAA partially restored the abundance of d2GFP in MPC-
397 expressing HepG2 spheroids (Supplementary Fig. 8e), suggesting rescued protein synthesis.
398 Like glutamate and proline, aspartate is derived from a TCA cycle intermediate,
399 specifically via transamination of oxaloacetate by glutamic-oxaloacetate transaminase 2 (GOT2).
400 Since GOT2 and PEPCK2 both use oxaloacetate as a substrate, we hypothesized that knocking
401 down GOT2 might phenocopy MPC expression by driving PEPCK2-mediated conversion of
402 oxalacetate into phosphoenolpyruvate and suppressing aspartate biosynthesis. Knock down of
403 *Got2* (the *Drosophila* gene encoding GOT2) reduced cell size in *Drosophila* fat body clones and
404 phenocopied MPC-expressing cells (Fig. 6i, j). Similarly, both GOT2 knock out and MPC-
405 expressing HepG2 cells were smaller than EV(Supplementary Fig. 8f). Expression of the MPC in
406 these GOT2 knock down systems had no significant impact on cell size (Fig. 6i, j and
407 Supplementary Fig. 8f), suggesting that the effects of MPC expression and GOT2 knock down
408 act similarly to limit amino acid synthesis and cell size. We next performed the reciprocal
409 experiment by over-expressing *Got2* to favor the production of aspartate from oxaloacetate. *Got2*
410 expression normalized cell size in both MPC-expressing fat body clones and in HepG2 spheroids
411 (Fig. 6i, j and Supplementary Fig. 8g, h). The efflux of aspartate from mitochondria into the
412 cytoplasm is a critical component of the malate-aspartate shuttle, which is a major redox shuttle
413 in human cells. To test whether increasing the abundance of aspartate would ameliorate the high
414 $NADH/NAD^+$ ratio observed in MPC-expressing cells, we supplemented growth media with
415 exogenous aspartate and assessed cellular redox status. We found that excess aspartate
416 reduced the cellular $NADH/NAD^+$ ratio in these cells such that it was comparable with control cells
417 (Fig. 6k). We observed similar results when we treated these cells with NMN or UK5099 (Fig. 6k).
418 Moreover, all these treatments increased protein synthesis in MPC-expressing cells (Fig. 6l, m).
419
420 **Mitochondrial pyruvate import reduces the size of rat primary hepatocytes**
421 Although HepG2 cells exhibit some features of hepatocytes, they are a transformed,
422 immortalized, and proliferative hepatocellular carcinoma cell line. We wanted to test whether the
423 MPC expression phenotypes that we observed in *Drosophila* fat bodies and HepG2 cells could
424 be recapitulated in a more physiologically relevant mammalian model. We chose primary rat
425 hepatocytes, which have been used extensively to interrogate hepatocyte cell metabolism and
426 signaling and also have the advantage of being genetically tractable. We expressed MPC1 and

427 MPC2 in cultured primary rat hepatocytes (Fig. 7a), and, consistent with our results in other
428 systems, we found that expression of MPC reduced cell size (Fig. 7b, c) and decreased protein
429 synthesis (Fig. 7d). MPC-expressing primary hepatocytes also had a higher NADH to $NAD^+$ ratio
430 in both the cytoplasmic and mitochondrial fractions (Fig. 7f). We assessed gluconeogenesis in
431 primary hepatocytes by quantifying glucose in the culture media following incubation with the
432 gluconeogenic precursors, pyruvate, and lactate. Glucose production was higher in MPC-
433 expressing hepatocytes compared with controls (Fig. 7e). Treatment with UK5099 eliminated this
434 effect and reduced glucose production to a similar rate in both cells (Fig. 7e). These results
435 demonstrate that augmented mitochondrial pyruvate in hepatocytes, and related cells in
436 *Drosophila*, drives a metabolic program that results in an increased NADH/$NAD^+$ ratio. This
437 scenario results in accelerated gluconeogenesis, decreased protein synthesis, and educed cell
438 size.
439

440 **Discussion**

441 We investigated whether pyruvate metabolism influences biosynthetic capacity and cell
442 size in the *Drosophila* fat body and in HepG2 spheroids. During the third instar phase of
443 *Drosophila* larval growth, when cells are rapidly expanding in size, we observed a profoundly
444 decreased expression of the MPC in liver-like fat body cells. We found that this rewiring of
445 pyruvate metabolism is essential for cell growth as forced maintenance of MPC expression
446 resulted in dramatically smaller cells. By combining *Drosophila* genetic analyses and
447 metabolomics studies in HepG2 cells and spheroids, we demonstrated that excess mitochondrial
448 pyruvate elevates the cellular NADH/$NAD^+$ ratio and redirects carbohydrate metabolism to favor
449 gluconeogenesis over glycolysis (Fig. 7g). This shift reduces the availability of oxaloacetate for
450 aspartate and glutamate biosynthesis, triggering a broader imbalance in amino acid abundances
451 within the cell. We conclude that altering the fate of pyruvate to support biomass accumulation is
452 required for the cell size expansion that occurs during fat body development. We speculate that
453 this phenomenon also applies to the mammalian liver, which is the closest analog of the
454 *Drosophila* fat body, as both HepG2 cells and primary rat hepatocytes show similar effects
455 following ectopic MPC expression.

456 Why does simply reorienting the metabolism of pyruvate have this profound effect on cell
457 growth? Our data suggest that a central mediator of the phenotype is an elevated NADH/$NAD^+$
458 ratio, which likely results from MPC expression driving an acceleration of the TCA cycle, as
459 evidenced by an increase in the abundances of M+2 isotopomers of TCA cycle intermediates.

460 Although the increase in labeled succinate, fumarate, and malate is modest, it occurs despite a
461 reduction in glycolytic labeling. This suggests that less labeled pyruvate feeds the TCA in MPC-
462 expressing cells compared with controls and that we are likely underestimating the actual increase
463 in flux. The TCA cycle generates NADH and appears to do so more actively in cells with
464 ectopically expressed MPC. However, our oxygen consumption data suggest that the oxidative
465 phosphorylation system in these cells does not have the capacity to increase its activity in
466 response to the enhanced availability of mitochondrial pyruvate and an increased $NADH/NAD^+$
467 ratio. As a result, the increased TCA cycle flux and limited ETC activity together elevate the
468 $NADH/NAD^+$ ratio in both the mitochondria and cytoplasm, disrupting cellular redox balance
469 leading to a rewiring of cellular metabolism.

470 This redox situation causes two distinct but related perturbations that appear to both
471 contribute to decreased cell growth. First, we observed a clear depletion of amino acids and
472 evidence of decreased synthesis of amino acids that are primarily derived from TCA cycle
473 intermediates (aspartate, glutamate, and proline). A reduced $NAD^+$ pool impairs the capacity of
474 cells to synthesize aspartate (Birsoy et al., 2015; Sullivan et al., 2015; Sullivan et al., 2018), which
475 is used to synthesize glutamate and proline and which plays a crucial role in maintaining redox
476 balance in both the mitochondria and cytoplasm (Alkan et al., 2018; Holecek, 2023a; Lieu et al.,
477 2020; Wei et al., 2020; Yoo et al., 2020). Replenishing any of these TCA cycle-derived amino
478 acids via genetic or nutritional increases in their availability was sufficient to reverse the effect of
479 ectopic MPC expression on cell size. Thus, amino acid depletion is a key driver of the small size
480 phenotype. Second, the increased $NADH/NAD^+$ ratio also drives a particular metabolic program
481 that favors the conversion of mitochondrial pyruvate to oxaloacetate and a subsequent increase
482 in gluconeogenesis. This program is enforced by allosteric regulation via NADH, acetyl-CoA, and
483 ATP, which act on PC and several enzymes of glycolysis and gluconeogenesis. It also appears
484 to be important for the small size of MPC-expressing cells since loss of any of several steps along
485 the gluconeogenic pathway, particularly PC and PEPCK2, mitigates or eliminates the cell size
486 phenotype observed with ectopic MPC expression in fat body cells and HepG2 spheroids. It is
487 important to note that gluconeogenesis is a critical function of these cells, and its rate is carefully
488 controlled in response to varying physiological stimuli. Surprisingly, constitutive MPC expression
489 is sufficient to supersede the control enacted by physiological and hormonal signals and enact
490 the loss of biomass and impaired cell size.

491 We have previously shown that loss of the MPC enhanced the stem cell identity and
492 proliferation of intestinal stem cells, whereas ectopic MPC expression had the opposite effect

493 (Bensard et al., 2020; Schell et al., 2017). Such observations are consistent with our findings that
494 MPC expression inversely correlates with biomass accumulation. More recent data demonstrated
495 that enhanced MPC activity prevented the increase in cell size that occurs in cardiomyocytes in
496 response to hypertrophic signaling (Cluntun et al., 2021; Fernandez-Caggiano et al., 2020). In
497 these cases, the fate of mitochondrial pyruvate that determines cell growth is its oxidation in the
498 TCA cycle. In contrast, our studies of hepatocytes and related cells described herein, demonstrate
499 that the fate of pyruvate that suppresses growth in cell size is not oxidation by the TCA cycle, but
500 rather the production of glucose, which starts with its conversion to oxaloacetate by PC in the
501 mitochondria. Cardiomyocytes have low expression of PC compared with liver, where this enzyme
502 (as well as others including PEPCK2) serves a vital role during fasting by producing glucose,
503 which fuels the brain and other organs that require glucose for their survival and function (Hatting
504 et al., 2018; Petersen et al., 2017; Rui, 2014). This is an example of how the unique metabolic
505 physiology of specialized cells plays a critical role in maintaining organismal homeostasis.

506 One conclusion from the data presented herein is that a cell's metabolic program plays a
507 decisive role in determining the growth of that cell. It was striking how rapidly expression of the
508 MPC impacted cell size in the HepG2 model. Essentially, as soon as MPC over-expression
509 became detectable, the population of cells started to show a decrease in size. Notably, the
510 decrease in cell size following ectopic MPC expression occurred despite the upregulation of
511 multiple pro-growth signaling networks. It is unclear why these networks are hyperactivated in this
512 context as there is no evidence from our data indicating any nutrients are in excess abundance.
513 We hypothesize that there may be regulators of cell size that recognize when cells are
514 inappropriately small and engage these pathways to increase cell size. mTORC1, PI3K, and Myc
515 pathways typically promote biomass accumulation and increased cell size but fail to do so when
516 mitochondrial pyruvate is elevated. MPC expression reduced the abundance of amino acids, and
517 this appears to play a dominant role to impair protein synthesis and prevent the cell growth effects
518 expected following hyperactivation of the mTORC1 and Myc pathways. Thus, our data suggest
519 that the metabolic fate of pyruvate can override canonical pathways that mediate cell size—such
520 as mTORC1 signaling.

521 We demonstrate that the appropriate partitioning of pyruvate metabolism maintains the
522 redox state of a cell to support the accumulation of biomass that is necessary for its specialized
523 function. Increased mitochondrial pyruvate metabolism in cells from the fly "liver-like" fat body
524 disrupts these processes, causes cells to perform excess gluconeogenesis, and prevents cell
525 growth. As a result, the *Drosophila* larvae became hyperglycemic and experience developmental

526 delay. The abundances of MPC1 and MPC2 are upregulated in mouse livers during starvation
527 and in high-fat diet conditions, which correlates with increased rates of gluconeogenesis in both
528 circumstances. Conversely, loss of the MPC in liver impairs gluconeogenesis (Gray et al., 2015;
529 McCommis et al., 2015; Yiew & Finck, 2022). Moreover, liver dysfunction in diabetes and hepatic
530 steatosis are driven by reductive stress and an elevated $NADH/NAD^+$ ratio (Goodman et al., 2020;
531 Jokinen & Luukkonen, 2024). We are intrigued by the possibility that the fate of pyruvate might
532 have profound consequences on the redox state and gluconeogenic capacity of the mammalian
533 liver, including by functioning as part of the metabolic milieu that drives unrestrained
534 gluconeogenesis in diabetes. Our discovery that mitochondrial pyruvate regulates the cellular
535 redox state, thereby controlling biosynthesis, offers insights for developing therapeutic strategies
536 for these and other diseases.
537

538 **Methods**

539 ***Drosophila* Strains and Handling**

540 *Drosophila melanogaster* stocks were maintained at 25°C on semi-defined fly food composed of
541 20 g agar, 80 g baker's yeast, 30 g sucrose, 60 g glucose, 0.5 g MgSO4, 0.5 g CaCl2, 11 ml
542 tegosept and 6 ml propionic acid. This was base medium for all *Drosophila* experiments, but
543 specific fly food modifications are mentioned in text and figure legends. To induce clones in fat
544 bodies, synchronized eggs were transferred to 29°C for 4 days until dissection. For experiments
545 involving genetic manipulation of all fat body cells, *tubGal80*$^{ts20}$ was used to restrict activity of *CG-*
546 *Gal4* at 18°C for 120 hours (57 hours equivalent time at 25°C) and larvae were shifted to 29°C till
547 dissection at specified time points.
548 Following fly stocks were procured from Bloomington stock center *UAS-MPC1-P2A-MPC2*
549 (28812582)*, CG-Gal4; tubGal80*$^{ts20}$*, hs-Flp1.22 (*BDSC, #77928), *Act>CD2>Gal4, UAS-GFP*
550 (BDSC, #4413), *Act>CD2>Gal4, UAS-RFP* (BDSC, #30558), *UAS-S6K*$^{STDETE}$ (BDSC, #6914),
551 *UAS-Rheb*$^{PA}$ (BDSC, #9689), *UAS-Myc*$^{OE}$ (BDSC, #9675), *UAS-Myc*$^{RNAi}$ (BDSC, #25783), *UAS-*
552 *PI3K93E*$^{.Excel}$ (BDSC, #8287), *UAS-PI3K93E*$^{A2860C}$ (BDSC, #8288), *UAS-TSC1*$^{RNAi}$ (BDSC,
553 #31314), *UAS-hPC* (BDSC, #77928), *UAS-PC*$^{RNAi}$ (BDSC, #56883), *UAS-PEPCK2*$^{RNAi}$ (BDSC,
554 #36915), *UAS-FBPase*$^{RNAi}$ (BDSC, #51871), *UAS-Pdk*$^{RNAi}$ (BDSC, #35142), *UAS-NMNAT*
555 (BDSC, #37002), *UAS-CintNDX* (BDSC, #93883), *UAS-ScerNDI1* (BDSC, #93878), *UAS-Slif*
556 (BDSC, #52661), *UAS-GOT2*$^{RNAi}$ (BDSC, #78778). From VDRC *UAS-MPC1*$^{RNAi(KK)}$ *and from NIG*
557 *UAS-Pdha*$^{RNAi}$*, UAS-Dlat*$^{RNAi}$ *(PDH E2)* were purchased.

558 **Generation of Overexpression and CRISPR Mutant fly stock**

559 *Pc* and *Pepck2* deletion fly stocks were generated using CRISPR-Cas9 as described (Gratz et
560 al., 2014). We targeted specific nucleotide sequences of the genes of interest through homology-
561 directed recombination using two guide RNAs and inserted a dsRed construct that expresses in
562 adult eyes to facilitate the selection of mutant flies. We deleted exon 1 to exon 5 using guide
563 RNAs for *Pc-KO*: 5′ guide ATACATTTAAGTCCTAGGC; 3′ guide TCGATTGATCCTGGAAACA.
564 *Pepck2-KO*, being a single exon coding sequence, we generated complete deletion by using
565 guides 5′ guide AAAGGGTGCACATCTGTGA; 3′ guide TTTGGGGCGTGGCCTAGAC. The
566 plasmids were injected into y[1] M{GFP[E.3xP3]=vas-Cas9.RFP}ZH-2A w[1118] (BDSC, #55821)
567 fly stock embryos (Bestgene) and one *Pc-KO* and five *Pepck2-KO* flies were picked up, confirmed
568 for the dsRed expression in adult eyes and used in subsequent experiments.

569 To overexpress *Got2*, *Got2* cDNA was amplified from RNA extracted from larval fat bodies using
570 primer 5' GAATTC ATGAGTAGAACCATTATTATGACGCTTAAGGAC, 3' CTCGAG
571 CTTGGTAACCTTGTGTATGCTCTCAGCCAGG. The cDNA was then cloned into a pUAST-aatB
572 plasmid using EcoRI and XhoI restriction enzymes, and the construct was injected into
573 pBac{yellow[+]-attp-9A}VK00005 (BDSC, #9725) embryos to obtain the insertion

574 **Mosaic Analysis and Phalloidin Staining for Cell Size Analysis**

575 Fat body clones were induced by the leaky expression of heat shock flippase 1.22 during
576 embryonic stages, and the 2D size of fat body cells was analyzed at 120 hours after egg laying
577 (AEL) using fluorescence microscopy. Cell size analysis was conducted as reported earlier
578 (Toshniwal et al., 2019). Fat bodies were dissected from larvae at the specified time points in 1X
579 PBS buffer (pH 7.2, Invitrogen, #10010049) and fixed in 8% paraformaldehyde (Sigma Aldrich, #
580 P6148) for 1 hour at room temperature (RT). The tissues were then washed twice with 0.1% PBT
581 (0.1% Triton X-100 (Sigma Aldrich, # X100) in 1X PBS buffer) for 10 minutes each. Subsequently,
582 the tissues were incubated with Rhodamine Phalloidin (Thermo Scientific, # R418) at a 1:400
583 dilution in 1X PBS buffer for 2 hours at room temperature (RT). After staining, the tissues were
584 washed once with 0.1% PBT and then with 1X PBS before being mounted in DAPI-supplemented
585 VectaShield (Vector Labs, #H1200). Representative images were captured using a Laser
586 Scanning Confocal Microscope (LSM 880, Carl Zeiss). For cell size analysis, images were
587 captured with a fluorescence microscope (Carl Zeiss, Axio Vision) at 20X magnification, focusing
588 on a plane where all nuclei were in focus. The 2D areas of fat body cells were measured using
589 FIJI software. Cell membranes stained with Rhodamine Phalloidin were traced using the freehand

590 tool, and the area of approximately 20-25 GFP-positive cells from fat bodies collected from about
591 five animals was measured as one replicate. All cell size analyses were conducted in a blinded
592 manner.

593 **Immunofluorescence on Fat Body Clones**

594 Larval fat bodies at 120 hours after egg laying (AEL) at 29°C were dissected in 1X PBS buffer
595 (pH 7.2), fixed in 8% paraformaldehyde for 1 hour at room temperature (RT), and then washed
596 three times in 0.1% PBT (0.1% Triton X-100 in 1X PBS buffer) for 10 minutes each. The tissues
597 were blocked in 10% normal goat serum (NGS, Jackson ImmunoResearch Laboratories, #005-
598 000-121) in 0.1% PBT for 1 hour at RT, followed by incubation with primary antibodies overnight
599 at 4°C. Secondary antibody incubation was performed for 2 hours at RT. Following three to four
600 washes in 0.3% PBT (10 minutes each) at RT, the tissues were mounted in DAPI-supplemented
601 Vectashield (Vector Laboratories, #H1200). Images were captured using a Laser Scanning
602 Confocal Microscope (LSM 880, Carl Zeiss).

603 **Image Acquisition and Analysis**

604 For all experiments, confocal images were captured using the same laser power and identical
605 settings, with z-stacks of the dissected tissue taken at 1 µm intervals along the Y-axis. The images
606 were analyzed using Fiji software, where a similar number of z-stacks focusing on the nuclei were
607 projected at mean intensities. Using the freehand tool, cell membranes were outlined, and the
608 mean fluorescence intensity (mean gray value) for each cell was recorded. To account for
609 background fluorescence, the average mean gray values of the background (measured from
610 regions of interest [ROI] of the same size) were subtracted from the recorded mean gray values
611 of the cells. The resulting mean gray values, adjusted for background fluorescence, were then
612 normalized, and the percent normalized mean gray values (with standard deviation, SD) of GFP-
613 negative and GFP-positive cells were plotted.

614 **Measurement of Protein Synthesis in Fat Bodies**

615 Protein synthesis in *Drosophila* fat bodies was analyzed using the Click-iT Plus OPP Alexa Fluor
616 594 kit (Molecular Probes, #C10457). Fat bodies were dissected at 120 hours AEL in Shields and
617 Sang M3 Insect Media (SSM3, Sigma, #S8398) and incubated with 5 mM O-propargyl-puromycin
618 (OPP) in SSM3 media for 30 minutes at RT. Tissues were then washed three times with 1X PBS
619 for 10 minutes each and fixed in 8% paraformaldehyde for 1 hour at RT. After fixation, the tissues
620 were washed twice with 0.1% PBT (0.1% Triton X-100 in 1X PBS) supplemented with 0.5% bovine
621 serum albumin (BSA) for 10 minutes each. The OPP was developed for 30 minutes at RT using

622 the Click-iT reaction mixture, which included 88 µl of OPP Reaction Buffer, 20 µl of Copper (III)
623 Sulfate (component D), 2.5 µl of component B, and 100 µl of Buffer Additive (component E),
624 following the manufacturer's instructions. The tissues were then washed twice in Reaction Rinse
625 Buffer for 10 minutes each, followed by two washes in 0.1% PBT supplemented with 0.5% BSA
626 for 10 minutes each at RT. After a final wash in 1X PBS, the fat bodies were mounted in DAPI-
627 supplemented Vectashield. Images were captured using a confocal microscope (LSM 880, Zeiss).

628 **LipidTOX Staining in Larval Fat Body Tissues**

629 At 120 hours AEL, 3rd instar larvae were dissected in 1X PBS. The fat bodies were fixed in 8%
630 paraformaldehyde for 1 hour at room temperature. After fixation, tissues were rinsed twice with
631 1X PBS. They were then incubated for 30 minutes in a 1:100 dilution of LipidTOX Red (Invitrogen,
632 #H34351) in PBS, followed by two additional rinses with PBS. The tissues were mounted in DAPI-
633 supplemented Vectashield and imaged using a confocal microscope. To quantify lipid droplet size,
634 the diameters of lipid droplets from 35 fat body clones were measured using FIJI software.

635 **EdU Incorporation in Fat Bodies**

636 At 120 hours AEL, fat bodies were dissected in 1X PBS and incubated with 5 µM 5-ethyl-2'-
637 deoxyuridine (EdU) in 1X PBS for 30 minutes at room temperature. The tissues were then washed
638 three times with 1X PBS for 10 minutes each, followed by fixation in 8% paraformaldehyde for 1
639 hour at room temperature. After fixation, the tissues were washed with 0.1% PBT supplemented
640 with 0.5% bovine serum albumin. EdU detection was performed using Click-iT Plus EdU Alexa
641 Fluor 594 (Molecular Probes, #C10639) for 30 minutes at room temperature, according to the
642 manufacturer's instructions. Following development, the fat bodies were mounted in DAPI-
643 supplemented Vectashield. Images were captured using a confocal microscope (LSM 880, Zeiss).

644 **RNA Isolation and RNA Sequencing**

645 To collect fat body tissues, $w^{1118}$ flies were mated at 25°C. The following day, flies were starved
646 for one hour, and eggs were collected every 2 hours. The first collection was discarded, and the
647 subsequent two collections were incubated at 25°C. After 20 hours, early hatched 1st instar larvae
648 were discarded, and 1st instar larvae collected over a 2-hour period were kept at 25°C. Fat bodies
649 from 10 male larvae at the specified time points were dissected and preserved in 1X PBS. For
650 RNA isolation from MPC-overexpressing fat bodies at 120 hours AEL, RNA was extracted and
651 purified using the NucleoSpin RNA kit (Takara Bio USA, Inc., #740955.50) with on-column DNA
652 digestion, as per the manufacturer's instructions. Four independent samples for each time point
653 were prepared for sequencing.

654 Library preparation for poly(A)-selected RNAs was carried out using the Illumina RNA TruSeq
655 Stranded mRNA Library Prep Kit with oligo-dT selection. Sequencing was performed using the
656 Illumina NovaSeq Reagent Kit v1.5 (150 bp paired-end reads) at the High-Throughput Genomics
657 Core Facility at the University of Utah. The raw sequencing data were analyzed using the
658 BDGP6.28 genome and gene feature files. Differentially expressed genes were identified using
659 DESeq2 version 1.30.0 with a 5% false discovery rate. RNA quality control, library preparation,
660 and sequencing were performed by the University of Utah Huntsman Cancer Institute High
661 Throughput Genomics and Bioinformatics Shared Resource. RNA-seq data from this study are
662 available at NCBI GEO.

663 **QPCR**

664 500 ng RNA was used to make cDNA using Superscript II reverse transcriptase (Molecular
665 Probes, #18064-022), dNTP (Molecular Probes, #18427-088) and oligodT (Molecular Probes,
666 #18418012). QPCR analyses were performed on cDNA as described using PowerUp SYBR
667 Green Master Mix (Applied Biosystems, #2828831) on QuantStudio 7 Flex (Applied Biosystems)
668 instrument. Fold changes in transcript level were determined using the ΔΔCt method. Transcript
669 levels were normalized to *rp49*. Each experiment was performed using 4–5 independent samples.
670 Following primers were used to do qPCR. List of primers is provided in Appendix 3

671 **Hemolymph Glucose and fat body glucose measurement**

672 Glucose concentrations in larval hemolymph and fat bodies were measured as previously
673 described (Ugrankar-Banerjee et al., 2023). To isolate hemolymph, 10 third instar larvae were
674 selected from culture tubes, thoroughly washed to remove any food residues, and then dried.
675 Hemolymph was collected by bleeding the larvae on a parafilm strip using Dumont 5 forceps (Fine
676 Science Tools, #11254-20). Two microliters of the colorless hemolymph were transferred to a 96-
677 well plate and mixed with 200 µl of Autokit Glucose reagent (Wako, #997-03001). For measuring
678 intercellular glucose, fat bodies were dissected from 10 larvae per genotype and homogenized in
679 approximately 300 microliters of ice-cold 1X PBS using a 29G1/2 syringe. The lysates were
680 inactivated at 70°C for 10 minutes, then centrifuged at maximum speed at 4°C. Thirty microliters
681 of the lysate were mixed with 170 µl of Autokit Glucose reagent. The plates were incubated at
682 37°C for 30 minutes, and absorbance was measured at 600 nm. Glucose concentrations were
683 determined based on the absorbance values recorded for glucose standards.

684 **HepG2 Cells – Knock down and Overexpression Strategies**

685 HepG2 cells were purchased from ATCC and maintained in EMEM supplemented with 10% FBS
686 and 1% PenStrep at 37°C in a 5% $CO_2$ atmosphere.
687 For inducible overexpression of human MPC1 and MPC2, the HA-MPC2-P2A-T2A-MPC1-FLAG
688 sequence was cloned into the pLVX-TetOne-Zeocin vector. Lentiviral particles were generated
689 using Gag-Pol, pMD2.G, and VSVG packaging plasmids.
690 Viral particles were produced by co-transfecting 293T cells with the respective packaging
691 plasmids using polyethylenimine (PEI, Sigma, #765090) as the transfection reagent at a 3:1 mass
692 ratio of PEI to DNA. The virus-containing medium was collected 48 hours post-transfection,
693 filtered through a 0.45 µm filter, and added to HepG2 cells cultured in normal medium, along with
694 polybrene (Sigma, #P1240000) at a concentration of 10 µg/ml. Transduced cells were selected
695 with 10 µg/ml Zeocin (Gibco, #R25001) for 1 week, and the level of overexpression was assessed
696 by western blotting.
697 For PC over-expression, PC coding sequence was amplified from mRNA isolated from HepG2
698 cells using primers 5' GAATTC ATGCTGAAGTTCCGAACAGTCCATGGG, 3' GGATCC
699 CTCGATCTCCAGGATGAGGTCGTCACC and cloned into pLenti-CMV-Blast. Similarly, SLC1A3
700 cDNA was amplified with primers 5' GGATCC ATGACTAAAAGCAATGGAGAAGAGC, 3'
701 CTACATCTTGGTTTCAATGTCGATGG and GOT2 coding sequence was amplified using
702 primers 5' GGATCC ATGGCCCTGCTGCACTCCGG, 3' TCTAGA
703 CTTGGTGACCTGGTGAATGGCATGG and cloned in pLenti-CMV-Blast (addgene, #17486). The
704 coding sequences of NDI (addgene, #72876) and d2GFP (addgene, #115665) were also cloned
705 into pLenti-CMV-Blast vector. Cells were selected on 3 µg/ml blasticidin (Gibco, A1113903) for 3
706 days. To generate knock out cells, following gRNAs were used. PCg5e-
707 GAAGCCTATCTCATCGGCCG *CGG,* PCg6e- CGAAGTCCGCTCGCTCAGAG *AGG*,
708 PEPCK2g2e-ATCTCCACTAAGCACTCGCA *GGG*, PEPCK2g3e-
709 CATGCGTATTATGACCCGAC *TGG*, GOT2ga- GAGTGGCCGGGTAAGCTGAGCAG *AGG*,
710 GOT2gb-GGAGTGGACCCGCTCCGGAACAG *TGG*. The guides were annealed and clones in
711 lentiCRISPRv2 with blasticidin (addgene, #83480) resistance using BsmBI.

712 **HepG2 Cells and 2D Cell Size Analysis**

713 HepG2 cells were cultured on 12 mm coverslips in a 24-well plate at a low density of 10,000 cells
714 per well in Human Plasma-Like Medium (Gibco, #A4899101) supplemented with 10% FBS
715 (Sigma, F0926) and 1% PenStrep (Thermo, #15140). The next day, treatments were initiated as
716 described in the figure legends, including 1 µg/ml doxycycline (Sigma, #D5207), 10 µM UK5099

717 (Sigma, PZ0160-5MG), 10 mM glycine (Sigma, #G7403), 5 mM alanine (Sigma, #A7469), 5 mM
718 asparagine (Sigma, #A4159), 5 mM aspartic acid (Sigma, #A7219), 5 mM glutamic acid (Sigma,
719 #G8415), 5 mM proline (Sigma, #P5607), 5 mM serine (Sigma, #S4311), 10 µM AZD7545
720 (MedChemExpress, #HY-16082), 1 mM dichloroacetate (Sigma, #347795), 100 nM duroquinone
721 (Sigma, #D223204), and 2 nM gramicidin (Sigma, #G5002).
722 For time-course experiments in Figure 3, cells were fixed at 2, 4, 6, 8, 10, 12, 18, and 24 hours
723 after doxycycline treatment using 4% paraformaldehyde in 1X PBS for 20 minutes at RT. For all
724 other experiments, cells were fixed 24 hours after doxycycline treatment. Following fixation, cells
725 were washed once with 0.1% PBT (0.1% Triton X-100 in 1X PBS) for 10 minutes and incubated
726 with Rhodamine Phalloidin at a 1:400 dilution in 1X PBS buffer for 20 minutes at RT. After a
727 couple of washes in 1X PBS, cells were mounted in DAPI-supplemented VectaShield.
728 Images were captured using a fluorescence microscope (Carl Zeiss, Axio Vision) focusing on the
729 plane of the cellular nuclei at 20X magnification, where all nuclei were in focus, and the 2D area
730 of HepG2 cells was measured using FIJI software. All cell size analyses were conducted in a
731 blinded manner.
732 For 3D cell volume analysis, images were captured using a Laser Scanning Confocal Microscope
733 (LSM 880, Carl Zeiss). The red fluorescence signal was used for 3D reconstruction, and cell
734 volume was measured using an ImageJ Macro code in FIJI.

735 **Measurement of Protein Synthesis in HepG2 Cells**

736 HepG2 cells were cultured in either 2D monolayers or spheroid forms. At the desired time point,
737 cells were treated with 20 µg/ml puromycin (Sigma, #P4512) in Human Plasma-Like Medium
738 (HPLM) for 30 minutes at 37°C. Following treatment, cells were washed with 1X PBS, and proteins
739 were extracted using 1X RIPA buffer at 4°C. Protein concentrations were quantified, and 15 µg
740 of total protein was separated by SDS-PAGE using standard methods. Proteins were then
741 transferred onto a nitrocellulose membrane, and puromycin-labeled peptides were detected using
742 an anti-puromycin [3RH11] antibody (Kerafast, #EQ0001) followed by incubation with an
743 appropriate secondary antibody.
744 Protein synthesis in HepG2 cells was also analyzed using the Click-iT HPG Alexa Fluor 594 kit
745 (Molecular Probes, #C10429). HepG2 cells were grown on 12 mm coverslips at a density of
746 10,000 cells per well and treated with 1 µg/ml doxycycline for 24 hours. Cells were then incubated
747 with 50 µM L-homopropargylglycine (HPG) in methionine-free DMEM (Gibco, #21013024) for 30

748 minutes at 37°C. After incubation, cells were washed twice with 1X PBS for 2 minutes each and
749 fixed in 4% paraformaldehyde for 20 minutes at room temperature.
750 For OPP staining, appropriately fixed cells were washed twice with 0.1% PBT (0.1% Triton X-100
751 in 1X PBS) supplemented with 0.5% bovine serum albumin (BSA) for 10 minutes each. HPG was
752 detected using the Click-iT reaction mixture, which included 88 µl of OPP Reaction Buffer, 20 µl
753 of copper solution (component D), 2.5 µl of component B, and 100 µl of Buffer Additive
754 (component E), following the manufacturer's instructions. Cells were washed twice in Reaction
755 Rinse Buffer for 10 minutes each, followed by two washes in 0.1% PBT supplemented with 0.5%
756 BSA for 10 minutes each at room temperature. After a final wash in 1X PBS, the coverslips were
757 mounted in DAPI-supplemented Vectashield. Images of the cells were captured using a confocal
758 microscope (LSM 880, Zeiss).

759 **Analysis of Spheroids**

760 HepG2 cells were cultured in ultra-low attachment 96-well plates (Costar, #7007) at a density of
761 10,000 cells per well in Human Plasma-Like Medium (HPLM) supplemented with 10% FBS and
762 1% penicillin-streptomycin. Treatments were applied as specified in the figure legends, including
763 1 µg/ml doxycycline, 5 mM aspartate, 5 mM glutamate, 10 µM UK5099, MEM non-essential amino
764 acids (Gibco, #11140050), 100 nM nicotinamide riboside (Sigma, #SMB00907), and 10 µM NMN
765 (Sigma, #N3501). Cells were incubated for 6 days at 37°C with CO2 and O2. Brightfield images
766 of the spheroids were captured using a Zeiss Axio Observer Z1 microscope, and spheroid size
767 was measured using FIJI software.
768 To quantify cell numbers, 12 spheroids from each condition (EV or MPC+) were pooled,
769 dissociated by trypsinization, and the number of cells was counted using a CellQuant system (Bio-
770 Rad).
771 For cell cycle analysis, cells were stained using Vybrant® DyeCycle™ Violet stain (Molecular
772 Probes, #V35003). After pooling and dissociating 12 spheroids from each condition (EV or
773 MPC+), cells were centrifuged and resuspended in 200 µL of 5 µM Vybrant® DyeCycle™ Violet
774 stain in EMEM supplemented with 10% FBS. The staining was performed by incubating the cells
775 at 37°C for 30 minutes, protected from light. Samples were analyzed using a BD Celesta flow
776 cytometer with ~405 nm excitation and ~440 nm emission. The resulting FCS files were
777 processed in FlowJo software, where the forward scatter of singlets was recorded, and median
778 data were used to plot graphs. Vybrant dye staining was employed to assess the distribution of
779 cells in the G1, S, and G2/M phases.

780 For apoptosis detection, an Annexin V/PI staining kit (Molecular Probes, #V13241) was used, with
781 5 µM camptothecin (MedChemExpress, #HY-16560) serving as a positive control. Sixteen
782 spheroids were collected, dissociated with trypsin as described above, and resuspended in 200
783 µL of 1X annexin-binding buffer. Cells were incubated with 1 µl of Alexa Fluor™ 488 Annexin V
784 (Component A) and 0.2 µl of 100 µg/ml PI working solution at room temperature for 15 minutes.
785 Stained cells were then analyzed using a BD Canto flow cytometer, measuring fluorescence
786 emission at 530 nm and 575 nm (or equivalent) with 488-nm excitation.

787 **Biomolecule Separation and Measurement**

788 For this experiment, biomolecules were extracted and measured from both *Drosophila* larvae fat
789 bodies and HepG2 cell spheroids. Fat bodies were dissected from 10 male larvae at 120 hours
790 after egg laying (AEL) and collected in 150 µl of 1X PBS. The samples were lysed by performing
791 three freeze-thaw cycles. A total of 24 spheroids were homogenized in 150 µl of
792 radioimmunoprecipitation assay (RIPA) buffer (50 mM Tris-HCl, 1% NP-40, 0.5% sodium
793 deoxycholate, 0.1% SDS, 150 mM NaCl, and 2 mM EDTA).
794 Lysates were centrifuged at 7500 × g for 5 minutes to remove debris. The resulting supernatant
795 was used for the following measurements. Triglyceride Measurement- For triglyceride analysis,
796 30 µL of the supernatant was incubated for 10 minutes at 75°C. Following this, 10 µl of
797 homogenate from the spheroids or 2 µL from fat bodies was added to 200 µl of Triglycerides
798 Reagent (Thermo Fisher Scientific, #TR22421). The mixture was incubated for 10 minutes at
799 37°C in 96-well microplates with gentle shaking. Absorbance was measured at 550 nm using the
800 Synergy Neo2 multimode plate reader (BioTek).
801 Protein Measurement- Protein concentrations were determined by mixing 2 µl of the supernatant
802 with 200 µl of BCA Protein Assay Reagent (Thermo Scientific, #23225). The mixture was
803 incubated for 30 minutes at 37°C with gentle shaking in 96-well microplates. Absorbance was
804 measured at 560 nm.
805 RNA and DNA Separation**-** The remaining 100 µl of the supernatant was processed for RNA and
806 DNA separation using TRIzol reagent (1 ml; Invitrogen, # 15596026). To separate RNA, 0.2 ml of
807 chloroform was added to the sample, followed by centrifugation at 12,000 × g for 15 minutes at
808 4°C. The RNA in the interphase was purified using 75% ethanol, following standard methods, and
809 quantified using a NanoDrop spectrophotometer. DNA was extracted from the organic phase by
810 adding 100% ethanol, followed by isopropanol precipitation. The resulting pellets were washed
811 with 0.3 M guanidine hydrochloride in 95% ethanol, resuspended in 0.1 M sodium citrate in 10%

812 ethanol (pH 8.5), and washed with 75% ethanol. Finally, the DNA pellets were resuspended in
813 0.1 ml of 8 mM NaOH by pipetting. The pH was adjusted to 7.2 with HEPES, and the DNA was
814 quantified using a NanoDrop spectrophotometer.

815 **Measurement Of NADH/NAD$^+$ Protocol**

816 For HepG2 cells, 1x10$^6$ cells treated with 1ug/ml dox for 24 hours were scraped in 1.5 ml tube.
817 For NADH/NAD$^+$ ratio analysis from spheroids, 18 spheroids were treated with 1ug/ml dox for 6
818 days were resuspended in 1mL 1XPBS. Scraped cells or pooled spheroids were centrifuged
819 (13,500x*g*, 10 s, 4°C) and tresuspended in 250 ul lysis buffer. Fat bodies from male 10 larvae
820 were dissected in 1X PBS and resuspended in lysis buffer provided with kit. To separate
821 cytoplasmic and mitochondrial fractions by rapid subcellular fractionation, lysates were
822 centrifuged (13,500x*g*, 10 s, 4°C) and the supernatant was collected for the cytosolic fraction,
823 while the remaining pellet contained the mitochondria. Mitochondrial pellet was resuspended in
824 100 ul lysis buffer.
825 NADH to NAD+ ratios were measured using Amplite Fluorimetric NAD$^+$/NADH ratio assay kit (AAT
826 Bioquest, #15263) as directed by instructions provided. Briefly, 25uL of cytoplasmic or
827 mitochondrial fractions were mixed with either NADH or NAD$^+$ extraction solution. Samples were
828 incubated at 37°C for 15 minutes. Later 25ul of either NAD$^+$ or NADH extraction was added which
829 was followed by incubation with 75ul mix of NADH sensor buffer and NAD$^+$/NADH recycling
830 enzyme for 1 hour at RT. Fluorescence intensity was recoded at 540 nm excitation and 590 nm
831 emission.

832 **Protein Extraction and Western Blotting**

833 HepG2 cells were directly scraped into RIPA supplemented with protease and phosphatase
834 inhibitors (Roche Molecular, #04906845001). For spheroids, 18 spheroids were pooled, washed
835 with 1X PBS, and then incubated in RIPA buffer with the protease and phosphatase inhibitor
836 cocktail. After 45 minutes on ice with vertexing every 15 minutes, lysates were centrifuged at
837 16,000xg for 15 minutes at 4°C to remove insoluble material.
838 Protein concentration was measured using the Bicinchoninic Acid (BCA) protein assay (Thermo
839 Fisher Scientific, 23225). Samples were mixed with 4x sample loading buffer and heated at 95°C
840 for 5 minutes. Protein samples (15 $\mu$g) were separated on SDS-polyacrylamide gel
841 electrophoresis (SDS-PAGE) at 20 mA per gel, transferred onto a 0.45 $\mu$m nitrocellulose
842 membrane (GE Healthcare) using the Mini Trans-Blot module (Bio-Rad) at 120 V for
843 approximately 2 hours.

844 The membrane was blocked with 5% non-fat milk (Serva) in Tris-buffered saline with 0.05%
845 Tween 20 (TBS-T) for 1 hour. It was then incubated overnight with primary antibodies diluted in
846 TBS-T. The next day, the membrane was washed with TBS-T and incubated with fluorophore-
847 conjugated secondary antibodies in TBS-T for 1 hour. Following additional washes with TBS-T,
848 fluorescence was detected using the Odyssey CLx imaging system (LI-COR Biosciences) and
849 analyzed using FIJI software. Antibodies used are listed in Appendix 1.

850 **Steady-State Metabolomic Studies**

851 10 million HepG2 cells with MPC+ and EV control expression were grown in 2D culture were
852 treated with 1ug/ml dox in HPLM supplemented with 10% HPLM. After 24 hours, culture medium
853 was collected and quenched with 1:4 volume of 100% methanol. Cells were washed and
854 quenched with 1 ml of 80% methanol in water. Cell lysates were then subjected to three rapid
855 freeze-thaw cycles and then spun at 16,000x*g* for 10 min at 4°C. The supernatants were
856 evaporated using a SpeedVac concentrator. Each sample or treatment were with 4 to 5 replicates.

857 **$^{13}$C-glucose tracing for M+3 vs M+2 ratio of TCA cycle metabolism**

858 10 million HepG2 cells with MPC+ and EV control expression were grown in 2D culture and were
859 treated with 1ug/ml dox in HPLM. After 24 hours, culture medium was changed to $^{13}$C-glucose
860 tracing media: glucose-free HPLM supplemented with 4.5g/L $^{13}$C glucose and 10% dialyzed FBS.
861 0 hour, 1 hour, 2 hours, and 4 hours later, cells were washed and quenched with 1 ml of 80%
862 methanol in water. Cells were scrapped out in Methanol and lysates were then subjected to three
863 rapid freeze-thaw cycles and then spun at 16,000x*g* for 10 min at 4°C. The supernatants were
864 evaporated using a SpeedVac concentrator.

865 **$^{13}$C-Lactate Tracing for Gluconeogenesis Assay**

866 10 million HepG2 cells with MPC+ and EV control expression were grown in 2D culture were
867 treated with 1ug/ml dox in DMEM without glucose, without glutamine (Gibco, #A1443001) with
868 10% dialyzed FBS. After 16 hours, culture medium was replaced with 6 ml of 1ug/ml dox in DMEM
869 without glucose, without glutamine and without FBS. 3 hours later, culture medium was replaced
870 with 6 ml of 1ug/ml dox and 20mM lactate (Sigma, #490040) containing DMEM without glucose
871 or glutamine or FBS. After 4 hours, 300 µl culture medium was collected and quenched with 1:4
872 volume of 100% methanol. Cells were washed and quenched with 1 ml of 80% methanol in water.
873 Cell lysates were then subjected to three rapid freeze-thaw cycles and then spun at 16,000x*g* for
874 10 min at 4°C. The supernatants were evaporated using a SpeedVac concentrator. Each cell
875 types had 4 to 5 replicates.

876 **Gas Chromatography-Mass Spectrometry Derivatization**

877 Dried metabolites were derivatized and prepared for Gas chromatography following standard
878 methods. Dried samples were resuspended in 30 µl of anhydrous pyridine with methoxamine
879 hydrochloride (10 mg/ml) and incubated at RT overnight. Next day, the samples were heated at
880 70°C for 15 min and centrifuged at 16,000*g* for 10 min. The supernatant was transferred to a pre-
881 prepared gas chromatography–mass spectrometry autoinjector vial with 70 µl of *N*-(*tert*-
882 butyldimethylsilyl)-*N*-methyltrifluoroacetamide (MTBSTFA) derivatization reagent. The samples
883 were incubated at 70°C for 1 hour, after which aliquots of 1 µl were injected for analysis. Samples
884 were analyzed using either an Agilent 6890 or 7890 gas chromatograph coupled to an Agilent
885 5973N or 5975C Mass Selective Detector, respectively. The observed distributions of mass
886 isotopologues of glucose, pyruvate, citrate, succinate, aspartate, glutamate, malate, fumarate,
887 phosphoenolpyruvate were corrected for natural abundance.

888 **Liquid chromatography-mass spectrometry**

889 Following standard methods, dried metabolites were resuspended in 100 µl of 0.03% formic acid
890 in analytical-grade water, vortexed, and centrifuged to remove insoluble material. 20 µl of
891 supernatant was collected and injected to AB SCIEX QTRAP 5500 liquid chromatography/triple
892 quadrupole mass spectrometer (Applied Biosystems SCIEX). Chromatogram review and peak
893 area integration were performed using MultiQuant (version 2.1, Applied Biosystems SCIEX). The
894 peak area for acetyl CoA, ADP, ATP, $NAD^+$, NADH was normalized against the total ion count of
895 that sample.

896 **Oxygen consumption rate**

897 Oxygen consumption rates (OCR) were measured using an XFe96 Extracellular Flux Analyzer
898 (Agilent) according to the manufacturer's instructions. Cells were plated at a density of 60,000
899 cells per well in Seahorse microplates (Agilent) and allowed to adhere for 6 hours. MPC was
900 induced with 1 µg/ml doxycycline overnight. Afterward, the cell culture media was removed and
901 replaced with Seahorse assay media, which consisted of DMEM supplemented with 4 mM
902 glutamine. OCR was assessed under basal conditions and following sequential injections of 1
903 mM glucose, oligomycin (2 µM), FCCP (0.5 µM), and a mix of rotenone plus antimycin A (2 µM
904 each). Immediately after the measurements, cells were lysed in RIPA buffer, and the protein
905 concentration was used to normalize the OCR data.

906 **Primary Hepatocyte Cultures and Analysis**

907 Rat primary hepatocytes (Lonza, #RWCP01) were thawed and plated in a 24-well plate at a
908 density of 0.16 million cells per well in Hepatocyte Plating Medium (Lonza, #MP100). Four hours
909 post-plating, the medium was replaced with Hepatocyte Basal Medium (HBM) supplemented with
910 BCM SingleQuots (Lonza, #CC-4182), including Bovine Pituitary Extract (BPE), Insulin,
911 Hydrocortisone, Gentamicin/Amphotericin-B (GA), Transferrin, and human Epidermal Growth
912 Factor (hEGF).
913 Twenty-four hours after plating, the hepatocytes were transfected with 1 µg of either pT3.GFP or
914 pT3.MPC2Flag-P2AT2A-MPC1HA using Lipofectamine 3000 (Invitrogen, #L3000001). Forty-
915 eight hours post-transfection, cells were lysed in 1X RIPA buffer, and Western blot analysis was
916 performed to confirm the overexpression of MPC1 and MPC2.
917 Forty-eight hours post-transfection, hepatocytes were fixed in 4% paraformaldehyde in 1X PBS.
918 Following several washes with 0.1% PBT, cells were incubated in 5% BSA and stained with anti-
919 MPC1 antibody overnight at 4°C. MPC1 was detected using a secondary anti-rabbit Alexa Fluor
920 antibody. Cells were also stained with Phalloidin Red. Coverslips were mounted in DAPI-
921 supplemented Vectashield, and images were captured using an LSM 880 confocal microscope.
922 Cell area marked by Phalloidin Red was quantified using differential interference contrast filter
923 and analyzed with FIJI software.
924 For protein synthesis measurement, hepatocytes were incubated with 20 µg/ml puromycin for 30
925 minutes. Puromycin-tagged peptides were visualized by immunostaining with rabbit anti-
926 puromycin antibody (1:500) and mouse anti-Flag M2 antibody (1:1000, Sigma, F1800), followed
927 by the appropriate secondary antibodies. Images were captured with the LSM 880 confocal
928 microscope. Puromycin intensity was measured using FIJI, and the percent change in puromycin
929 intensity in Flag-positive cells was compared to Flag-negative cells.
930 Gluconeogenesis was assessed using lactate and pyruvate as substrates. Forty-eight hours post-
931 transfection, hepatocytes were incubated in low-glucose DMEM with 1 mM sodium pyruvate and
932 4 mM glutamine without FBS. After 16 hours, hepatocytes were treated with 200 ng glucagon in
933 no-glucose DMEM without FBS for 3 hours. Cells were then cultured in media with 20 mM lactate
934 and 2 mM pyruvate, with and without 10 µM UK5099, for 2 and 4 hours. Glucose levels in the
935 media were measured using the Amplex Red Glucose Assay Kit (Invitrogen, #A22189) according
936 to the manufacturer's instructions. Glucose production per cell per hour was plotted on a graph.
937 The compartmentalized NADH to $NAD^+$ ratio in hepatocytes was quantified 48 hours post-
938 transfection using the Amplite Fluorimetric $NAD^+$/NADH Ratio Assay Kit as described previously.
939

940 ## Figure Legends
941
942 **Figure 1: Increased mitochondrial pyruvate transport reduces size of *Drosophila* fat body**
943 **cells.**
944 **a-b. a**) A schematic representation of *Drosophila* developmental stages with specified time points
945 (hours after egg laying (AEL) at 25°C) at which larvae were dissected to collect fat bodies. **b)**
946 Representative images of larval fat bodies at the indicated times (hours AEL) stained with
947 rhodamine phalloidin to visualize cell membranes and DAPI to visualize DNA. The scale bar
948 represents 25 µm.
949 **c.** Quantification of fat body cell area based on rhodamine phalloidin stained cell membranes at
950 the indicated time points. Data are presented as mean ± standard deviation (s.d.) from six
951 biological replicates, with each replicate averaging the size of 50 randomly selected cells from fat
952 bodies dissected from five male larvae.
953 **d-e. d)** A schematic of pyruvate metabolism. In the cytoplasm, pyruvate is a product of glycolysis,
954 synthesized by Pyruvate Kinase (Pyk) or from lactate via Lactate Dehydrogenase (LDH). Pyruvate
955 is transported into mitochondria by the Mitochondrial Pyruvate Carrier (MPC) complex. Within
956 mitochondria, pyruvate is converted into acetyl-CoA by Pyruvate Dehydrogenase (PDH) or into
957 oxaloacetate by Pyruvate Carboxylase (PC), both of which are substrates for the TCA cycle.
958 PEPCK2 converts oxaloacetate into phosphoenolpyruvate. **e)** *Pyk*, *Mpc1*, *Mpc2, Pdha* and *Dlat*
959 transcripts were quantified from larval fat bodies collected at the indicated times.
960 **f-g. f)** Representative confocal microscope images of phalloidin- and DAPI-stained fat bodies with
961 flip-out Gal4 clones expressing MPC1-P2A-MPC2 (MPC+), marked with GFP at 120 hours AEL.
962 The images at the bottom show magnified insets of GFP-positive cells in control and MPC
963 expressing clones. **g)** Quantification of GFP-positive clonal cell area with the indicated genetic
964 manipulations- control, MPC+ and *Mpc1*-KD. Data are presented as mean ± s.d. from six
965 biological replicates, with each set averaging the size of 20 clonal cells from fat bodies collected
966 from five male larvae.
967 **h-i. h)** Images showing control and MPC+ clones from larvae fed on no sugar diet. **I)**
968 Quantification of the area of control, MPC+ and *Mpc1*-KD fat body clonal cells from larvae fed on
969 a diet containing either 9% sugar or no sugar.
970 **j.** Quantification of the area of MPC+ fat body clonal cells from larvae fed a diet supplemented
971 with or without 20 µM UK5099.

972 **k.** Fold change of the abundances of the indicated macromolecules in fat bodies expressing MPC
973 (MPC+) in all fat body cells using CG-Gal4. The abundance of each individual macromolecule is
974 normalized to that of the respective macromolecular abundance in GFP expressing, control fat
975 bodies. Data are represented as mean ± s.d. from three biological replicates with fat bodies
976 collected from 10 larvae at 120 hours AEL.
977 **l-m. l**) Representative images of fat body clones stained with O-propargyl-puromycin (OPP, 20
978 µM for 30 minutes), showing control and MPC expressing GFP-positive cells. The top panels
979 show GFP-positive clones and OPP staining in red, while the bottom panels show respective OPP
980 channel. Arrows indicate cells with the specified genetic manipulation. The scale bar represents
981 20 µm. **M)** Quantification of OPP fluorescence intensity of control or MPC+ fat body cells
982 compared to neighboring non clonal cell. Data are presented as mean ± s.d. from six biological
983 replicates, with each set averaging the size of 20 clonal cells from fat bodies collected from five
984 male larvae.
985 Unpaired t-tests or one-way ANOVA tests were performed to evaluate the statistical significance
986 of the data, with p-values mentioned in the graphs where significance was noted.
987
988 **Supplementary Figure 1: Transcriptomic changes in fat body during larval development**
989 **(related to Main Figure 1).**
990 **a.** A heatmap displaying changes in mRNA abundance of genes encoding mitochondrial proteins
991 and enzymes involved in various metabolic pathways in wild type- $w^{1118}$ fat bodies collected at the
992 specified time points. Right. Clustered hallmarks are indicated by a color gradient corresponding
993 to relative gene expression levels.
994 **b.** A heatmap illustrating transcriptomic changes in signaling pathways in $w^{1118}$ fat body cells
995 during *Drosophila* larval development.
996 **c**. Quantification of *Pepck* and *Pepck2* transcripts from larval fat bodies collected at the indicated
997 times.
998
999 **Supplementary Figure 2 – Increased mitochondrial pyruvate transport reduces size of**
1000 ***Drosophila* fat body cells. (Related to Main Figure 1)**
1001 **a.** Schematic representation of experimental time course using temperature-sensitive $Gal80^{ts20}$ to
1002 control Gal4 expression. At 18°C, $Gal80^{ts20}$ is active, inhibiting Gal4 expression; at 29°C, $Gal80^{ts20}$
1003 is inactive, allowing Gal4 expression. The temperature switch occurs towards the end of the 2nd

1004 instar stage so that MPC expression construct is induced temporally only during the 3rd instar
1005 stage. Fat bodies were collected at the specified time points.
1006 **b.** Quantification of *Mpc1* and *Mpc2* transcripts from fat bodies of CG-Gal4>MPC+ versus CG-
1007 Gal4>GFP or control larvae, dissected at the indicated times after the induction of Gal4 activity.
1008 **c.** Quantification of fat body cell area in MPC+ (CG-Gal4>MPC+) versus control (CG-Gal4>GFP)
1009 larvae at the indicated times after Gal4 induction. Data are presented as mean ± s.d. from six
1010 biological replicates, with each replicate representing the average size from 50 randomly selected
1011 cells from fat bodies dissected from five male larvae.
1012 **d.** Schematics illustrating the use of the Ay-Gal4 cassette to generate clones with MPC
1013 expression. Clones are generated by leaky expression of hs-flp1.22-flippase, which binds to
1014 specific FRT sites in chromatin, leading to the excision of the spacer *'yellow'* gene and positioning
1015 of the *actin5C* promoter next to the Gal4 coding sequence. This is followed by Gal4 expression in
1016 the cell and subsequent expression of UAS-GFP or UAS-MPC1-P2A-MPC2 constructs. Due to
1017 the leaky and random expression of the flippase, GFP-marked mosaicism occurs in only 1-5% of
1018 fat body cells.
1019 **e-f.** Representative images of fat bodies with MPC expression and control clones, showing
1020 increased abundance of (**e)** MPC1 and (**f)** MPC2 proteins. Arrows indicate cells with the specified
1021 genetic manipulation. The scale bar represents 20 µm.
1022 **g.** Representative images of fat bodies with MPC+ and control clones dissected from larvae fed
1023 on a diet supplemented with 20 µM UK5099. Arrows indicate cells with the specified genetic
1024 manipulation. The scale bar represents 20 µm.
1025 **h-k.** The abundances of **(h)** DNA, **(i)** RNA, **(j)** triacylglycerides (TAGs), and **(k)** protein in fat bodies
1026 where MPC is expressed in all fat body cells using CG-Gal4 driver. The abundance of each
1027 individual macromolecule is normalized to that of the control. Data are represented as mean ±
1028 s.d. from three biological replicates with fat bodies collected from ten larvae at 120 hours AEL.
1029 **l-n. l)** Representative images of MPC+ and control fat body clones showing lipid droplets stained
1030 with LipidTox in red. The area in square is presented in high-magnification insets below to show
1031 lipid distribution in the clonal cells. The scale bar represents 25 µm. **m)** Quantification of lipid
1032 droplets relative to cell size in MPC+ versus control cells. **n)** The data are presented as the
1033 number of lipid droplets per cell area and the fraction of cell area covered by lipid droplets.
1034 **o-p. o)** Representative EdU-stained confocal images of MPC+ and control fat body cells, showing
1035 replicating DNA. Arrows indicate cells with the specified genetic manipulation. The scale bar
1036 represents 20 µm. **p)** Quantification of total EdU fluorescence intensity in GFP-positive cells

1037 compared to neighboring GFP-negative cells in MPC+ versus control clones. Data are presented
1038 as mean ± s.d.
1039 Unpaired t-tests were performed to evaluate the statistical significance of the data, with p-values
1040 noted in the graph if significance was observed.
1041
1042 **Figure 2: mTORC1 and Myc pathways are hyperactivated in MPC overexpressing fat body**
1043 **cells.**
1044 **a**. Schematic of the mTORC1 pathway. The mTORC1 pathway is activated by pro-growth signals
1045 such as insulin, leading to the phosphorylation of S6 kinase (S6K) and 4EBP. S6K phosphorylates
1046 ribosomal protein S6, while 4EBP phosphorylation inactivates 4EBP and releases elongation
1047 factor eIF4E. These events increase ribosomal assembly and elongation rates, thereby enhancing
1048 protein synthesis.
1049 **b-c**. **b)** Representative images of fat body clones with *S6k* over-expression, control clones, and
1050 MPC+ clones, stained for phosphorylated S6 (p-S6) in red (top panels) and white (bottom panels).
1051 Arrows indicate clonal cells with the specified genetic manipulation. The scale bar represents 20
1052 µm. **c)** Quantification of total p-S6 fluorescence intensity in GFP-positive cells compared to
1053 neighboring GFP-negative cells in MPC+ versus control clones. Data are presented as mean ±
1054 s.d. with statistical significance as scored with One-way Annova test.
1055 **d-e**. **d)** Representative images of fat body clones with *Rheb* over-expression, control clones, and
1056 MPC+ clones stained for phosphorylated 4EBP (p-4EBP) in red (top panels) and white (bottom
1057 panels). Arrows indicate clonal cells with the specified genetic manipulation. The scale bar
1058 represents 20 µm. **e)** Quantification of total p-4EBP fluorescence intensity in MPC+ versus control
1059 clones with statistical significance as scored with One-way Annova test.
1060 **f-g. f**) Representative images of fat body clones with *Myc* knockdown, control clones, and MPC+
1061 clones stained for Myc protein in red (top panels) and white (bottom panels). Arrows indicate
1062 clonal cells with the specified genetic manipulation. The scale bar represents 20 µm. **g)**
1063 Quantification of total Myc fluorescence intensity in MPC+ versus control clones with statistical
1064 significance as scored with One-way ANOVA test.
1065 **h-i**. **h)** Representative images of fat body clones from starved wild type, control clones, and MPC+
1066 clones, stained for phosphorylated eIF2α (p-eIF2α) in red (top panels) and white (bottom panels).
1067 Arrows indicate clonal cells with the specified genetic manipulation. The scale bar represents 20
1068 µm. **i)** Quantification of total p-eIF2α fluorescence intensity in MPC+ versus control clones with
1069 statistical significance as scored with One-way ANOVA test. Data are presented as mean ± s.d.

1070 One-way ANOVA tests were performed to evaluate the statistical significance of the data, with p-
1071 values noted in the graph if significance was observed.
1072
1073 **Supplementary Figure 3: mTORC1 and Myc pathways are hyperactivated in MPC**
1074 **overexpressing fat body cells. (Related to Main Figure 2)**
1075 **a**. Representative images of fat body clones with PI3K-DN (dominant-negative) expression,
1076 control clones, and MPC+ clones stained for dFoxo in red (top panels) and white (bottom panels).
1077 Arrows indicate clonal cells with the specified genetic manipulations. The scale bar represents 20
1078 µm.
1079 **b**. Transcriptomic analysis of MPC+ fat bodies compared to control, represented as Hallmarks
1080 from GSEA (Gene Set Enrichment Analysis).
1081 **c-d**. Quantification of the area of MPC+ cells with or without *PI3K* over-expression **(c),** and with
1082 or without *Tsc1* knock down **(d).** Data are presented as mean ± s.d. from five biological replicates,
1083 where each data point represents the average size of 20 clones from fat bodies collected from
1084 five male larvae.
1085 **e-f**. Quantification of cell area in MPC+ clones with *Myc* over-expression **(e)** or *Myc* knockdown
1086 **(f).** Data are presented as mean ± s.d. from five biological replicates, where each data point
1087 represents the average size of 20 clones from fat bodies collected from five male larvae.
1088
1089 **Figure 3: Increased mitochondrial pyruvate transport reduces size of HepG2 spheroids.**
1090 **a.** Western blots showing inducible expression of MPC1 and MPC2 at 2-hour intervals following
1091 treatment with 1 µg/ml doxycycline. Citrate synthase and tubulin were used as loading controls.
1092 Both endogenous and epitope tag bands are shown.
1093 **b.** Quantification of the 2D area of HepG2 cells with MPC expression (MPC+) or empty vector
1094 (EV) fixed and stained with rhodamine phalloidin at the indicated times after doxycycline
1095 treatment. Data are presented as mean ± s.d. from five biological replicates, with each replicate
1096 representing the average size of 25 randomly selected cells.
1097 **c.** Quantification of the 2D area of MPC+ or EV HepG2 cells treated with 10 µM UK5099. Data
1098 are presented as mean ± s.d. from five biological replicates, with each replicate representing the
1099 average size of 25 randomly selected cells.
1100 **d-e. d)** Representative brightfield images of HepG2 spheroids with empty vector (EV) or MPC
1101 expression (MPC+) treated with 1 µg/ml doxycycline for six days. The scale bar represents 200

1102 µm. **e)** Quantification of spheroid area from images of MPC+ or EV HepG2 spheroids, with or
1103 without doxycycline treatment. Data are presented as mean ± s.d. from 30 technical replicates.
1104 **f-g. f)** Forward scatter (FSC) of cells dissociated from MPC+ (red) or EV spheroids with cell count
1105 normalized to mode. **g)** Median FSC of MPC+ HepG2 spheroids treated with or without 1 µg/ml
1106 doxycycline. Data are presented as mean ± s.d. from three biological replicates.
1107 **h.** Fold change in macromolecules—DNA, TAGs, RNA, and protein—fractionated from EV or
1108 MPC+ HepG2 spheroids normalized to that in EV HepG2 cells.
1109 **i-j. i)** Representative images showing L-Homopropargylglycine (HPG)-labeled newly synthesized
1110 proteins in EV or MPC+ HepG2 cells. The top panels show HPG staining, and the lower panels
1111 show nuclei stained with DAPI. The scale bar represents 20 µm. **j)** Quantification of HPG
1112 fluorescence intensity is presented as mean ± s.d. from 35 cells, for both EV and MPC+ cells.
1113 **k-l. k)** Western blot analysis of nascent protein synthesis using a puromycin incorporation assay
1114 (20 µg/ml puromycin for 30 minutes) in either EV or MPC+ HepG2 spheroids (protein lysates from
1115 16 spheroids loaded in each lane). **l)** Quantification of 70 kD band intensity in puromycin blot
1116 normalized with tubulin band intensity and represented as mean ± s.d. from three independent
1117 experiments.
1118 **m.** Relative accumulation of destabilized GFP (d2GFP) in EV or MPC+ HepG2 spheroids treated
1119 with or without 1 µg/ml doxycycline ± 10 µM UK5099. Data are presented as mean ± s.d. from
1120 three biological replicates.
1121 Unpaired t-tests, one-way, or two-way ANOVA tests were performed to evaluate the statistical
1122 significance of the data, with p-values noted in the graph if significance was observed.
1123
1124 **Supplementary Figure 4: MPC overexpression reduces size of HepG2 cells in 2D and**
1125 **spheroid culture (Related to Main Figure 3).**
1126 **a**. Quantification of cell volume from confocal images of HepG2 cells expressing MPC (MPC+) or
1127 an empty vector (EV). Data is presented as mean ± s.d. from 22 EV cells and 25 MPC+ cells.
1128 **b**. Quantification of the number of cells per spheroid in EV or MPC+ HepG2 cells with or without
1129 doxycycline treatment. Data is presented as mean ± s.d. from 18 technical replicates.
1130 **c**. Cell cycle profiles of MPC+ HepG2 spheroids treated with or without doxycycline treatment.
1131 Data is presented as mean ± s.d. from three biological replicates.
1132 **d**. Annexin/Propidium Iodide (PI) analysis of MPC+ HepG2 cells cultured with or without
1133 doxycycline. Data is presented as mean ± s.d. from three biological replicates.

1134 **e-h**. Concentrations of **(e)** DNA, **(f)** RNA, **(f)** triacylglcyerides (TAGs) and **(g)** protein measured
1135 for 18 MPC+ and 18 EV HepG2 cells. Data is shown as mean ± s.d. from three biological
1136 replicates.
1137 Unpaired t-tests and one-way ANOVA tests were performed to evaluate the statistical significance
1138 of the data, with p-values mentioned in the graph if significance is noted.
1139
1140 **Figure 4: Increased mitochondrial pyruvate metabolism promotes gluconeogenesis via**
1141 **Pyruvate Carboxylase to suppress protein synthesis.**
1142 **a.** Schematic illustration of the $^{13}$C-glucose tracing strategy used to measure the activity of
1143 Pyruvate Dehydrogenase (PDH) and Pyruvate Carboxylase (PC). TCA metabolites labeled with
1144 two heavy carbons ($^{13}$C or M+2 TCA pool) result from PDH activity, whereas M+3 TCA metabolites
1145 result from PC activity. PDH is inhibited by PDK-mediated phosphorylation. DCA and AZD7545
1146 are inhibitors of PDK.
1147 **b.** Fractional enrichment of M+2 succinate in empty vector (EV; red) and MPC expressing (MPC+;
1148 blue) HepG2 cells at the indicated times after $^{13}$C-glucose tracing. MPC expression was induced
1149 for 24 hours by treatment with 1 $\mu$g/ml doxycycline and media was changed to $^{12}$C-glucose. The
1150 change in M+2 succinate is significant (by two-way ANOVA test) at one hour after $^{13}$C glucose
1151 incubation.
1152 **c.** Fractional enrichment of M+3 succinate in EV (red) and MPC+ (blue) HepG2 at the indicated
1153 times after $^{13}$C-glucose tracing. MPC expression was induced for 24 hours by treatment with 1
1154 µg/ml doxycycline. The change in M+3 succinate is significant (by two-way ANOVA test) at four
1155 hours after $^{13}$C-glucose incubation.
1156 **d.** Rate of oxygen consumption (OCR) in EV and MPC+ HepG2 cells.
1157 **e-f. e)** Representative images of phalloidin- and DAPI-stained fat body cells. Arrows indicate GFP-
1158 positive clones with MPC expression (MPC+), *Pcb* knock down with MPC expression (MPC+,
1159 *Pcb*-KD) or *Pcb* overexpression (*Pcb*+). The scale bar represents 20 $\mu$m. **f)** Quantification of the
1160 area of GFP-positive clones with control, MPC+, *Pcb* over-expression (*Pcb*+), *Pcb* and MPC co-
1161 expression (MPC+, *Pcb*+), *Pcb* knock down (*Pcb*-KD) and *Pcb* knock down with MPC expression
1162 ( MPC+, *Pcb*-KD) shown as mean ± s.d. of five biological replicates, with each group representing
1163 the analysis of 20 the indicated clonal cells.
1164 **g-h.** Concentration of glucose in the fat body **(g)** and hemolymph **(h)** of larva with fat body-specific
1165 expression MPC or control. Data is presented as mean ± s.d. of three biological replicates
1166 analyzed by unpaired t-tests.

1167 **i-k**. **i)** Schematic illustration of the strategy to analyze gluconeogenesis from $^{13}$C-lactate. Cells
1168 convert $^{13}$C-lactate into $^{13}$C-pyruvate, which is transported into mitochondria by the MPC. PC
1169 converts $^{13}$C-pyruvate (M+3) into oxaloacetate (M+3). PEPCK2 converts oxaloacetate (M+3) into
1170 phosphoenolpyruvate (M+3), which is converted into M+6 glucose and excreted from cells. **j)**
1171 Relative abundances of M+3 phosphoenolpyruvate (PEP) in EV and MPC+ HepG2 cells and **k)**
1172 M+6 glucose in their respective media following treatment with 20 mM $^{13}$C-lactate for four hours.
1173 Data is presented as mean ± s.d. of three biological replicates, each with an average of three
1174 technical replicates.
1175 **l-m. l)** Representative brightfield images of EV, MPC+, and PC knockout (KO) or PEPCK2 KO
1176 with or without MPC expression HepG2 spheroids. The scale bar represents 200 $\mu$m. **m)**
1177 Quantification of spheroid area is presented as mean ± s.d. of 30 technical replicates.
1178 **n-o. n)** Representative images of phalloidin- and DAPI-stained of fat body cells. Arrows indicate
1179 GFP-positive clones with MPC expression (MPC+), and *Pepck2* knockdown with MPC expression
1180 (MPC+, *Pepck2*-KD). The scale bar represents 20 $\mu$m. **o)** Quantification of the area of GFP-
1181 positive clones with MPC+, *Pepck2* knock down (*Pepck2*-KD), *Pepck2* knock down with MPC+
1182 (MPC+, *Pepck2*-KD), *Fbp* knock down (*Fbp*-KD), *Fbp* knock down with MPC+ (MPC+, *Fbp*-KD).
1183 Data is presented as mean ± s.d. of five biological replicates, with each group analyzing 20 clonal
1184 cells of the mentioned genetic manipulations.
1185 **n-o. n)** Representative images of fat body clones stained with OPP (red). Arrows indicate GFP-
1186 positive clones with MPC expression (MPC+), *Pcb* knockdown with MPC expression (MPC+, *Pcb*-
1187 KD), or *Pepck2* knockdown with MPC expression (MPC+, *Pepck2*-KD). The scale bar represents
1188 20 $\mu$m. **o)** Quantification of OPP intensity in the indicated clones compared with adjacent wild-
1189 type cells. Data is presented as mean ± s.d.
1190 Unpaired t-tests, one-way ANOVA tests, or two-way ANOVA tests were performed to evaluate
1191 the statistical significance of the data, with p-values mentioned in the graph if significance is noted.
1192
1193 **Supplementary Figure 5: Surge of mitochondrial pyruvate reduced glycolysis and**
1194 **promotes gluconeogenesis via Pyruvate Carboxylase (Related to Main Figure 4).**
1195 **a-c.** Fractional enrichment of M+3 3-phosphoglyceric acid **(a)**, M+3 pyruvate **(b)**, and M+3 alanine
1196 **(c)** in empty vector (EV; red) and MPC expressing (MPC+; blue)) HepG2 cells at the indicated
1197 times after $^{13}$C glucose tracing.
1198 **d-e.** Fractional enrichment of M+2 fumarate **(d)** and M+2 malate **(e)** in EV (red) and MPC+ (blue)
1199 HepG2 cells.

1200 **f-g.** Fractional enrichment of M+3 fumarate **(f)** and M+3 malate **(g)** in EV (red) and MPC+ (blue)
1201 HepG2 cells. A two-way ANOVA test showed significant differences at four hours after $^{13}C$ glucose
1202 tracing.
1203
1204 **Supplementary Figure 6: Surge of mitochondrial pyruvate promotes gluconeogenesis via**
1205 **Pyruvate Carboxylase to suppress protein synthesis (Related to Main Figure 4).**
1206 **a.** Quantification of the area of GFP-positive fat body clones with control, MPC expression
1207 (MPC+), *Pcb* knockout (*Pcb KO*), or MPC expression with *Pcb* knockout (MPC+, *Pcb* KO). Data
1208 is presented as mean ± s.d. of five biological replicates, with each group analyzing 20 clonal cells
1209 of the indicated genetic manipulations.
1210 **b.** Quantification of the areas of HepG2 cells with MPC+ with or without pyruvate carboxylase
1211 (PC) knockout using two independent sgRNA guides (PCg5 and PCg6). Western blots show the
1212 efficiency of PC knockout. Data is presented as mean ± s.d. of five biological replicates, each
1213 representing 25 randomly selected cells for each indicated genotype.
1214 **c-d. c)** Representative images of phalloidin- and DAPI-stained fat body cells. Arrows indicate
1215 GFP-positive clones with MPC expression (MPC+), *Pdha* knock down (*Pdha*-KD), or MPC
1216 expression with *Pdk* knock down (MPC+, *Pdk*-KD). The scale bar represents 20 $\mu$m. Right. **d)**
1217 Quantification of the areas of GFP-positive clones with control, MPC+, *Pdha* knock down (*Pdha*-
1218 KD), *Pdha*-knock down with MPC expression (MPC+, *Pdha*- KD), *Dlat* knock down (*Dlat*-KD), *Dlat*
1219 knock down with MPC expression (MPC+, *Dlat*-KD); *Pdk* knock down (*Pdk*-KD), and *Pdk* knock
1220 down with MPC expression (MPC+, *Pdk*-KD). Data is presented as mean ± s.d. of five biological
1221 replicates, with 20 clonal cells analyzed for each of the indicated genetic manipulations.
1222 **e.** Quantification of the areas of MPC+ HepG2 cells treated with the PDK inhibitors AZD7545 (10
1223 $\mu$M) or dichloroacetate (1 mM). Data is presented as mean ± s.d. of five biological replicates, with
1224 25 randomly selected cells analyzed for each of the indicated groups.
1225 **f.** Quantification of the areas of MPC+, PEPCK2 knock out HepG2 cells. Western blots show the
1226 efficiency of PEPCK2 knockout. Data is presented as mean ± s.d. of five biological replicates with
1227 25 randomly selected cells analyzed for each of the indicated groups.
1228 **g.** Quantification of the area of GFP-positive control; MPC+; *Pepck2 KO*; and MPC+, *Pepck2 KO*
1229 fat body clonal cells. Data is presented as mean ± s.d. of five biological replicates, with 20 clonal
1230 cells analyzed for each of the indicated genetic manipulations.

1231 Unpaired t-tests, one-way ANOVA tests, or two-way ANOVA tests were performed to evaluate
1232 the statistical significance of the data, and p-values are mentioned in the graph if significance is
1233 noted.
1234
1235 **Figure 5: Redox imbalance impedes protein synthesis and cell growth from elevated**
1236 **pyruvate metabolism in mitochondria.**
1237 **a.** NADH/$NAD^+$ ratios from the cytoplasmic and mitochondrial fractions of control and MPC-
1238 expressing (MPC+) fat bodies. Data is presented as mean ± s.d. of six biological replicates.
1239 **b.** NADH/$NAD^+$ ratios from the cytoplasmic and mitochondrial fractions of empty vector (EV) and
1240 MPC-expressing (MPC+) HepG2 spheroids. Data is presented as mean ± s.d. of six biological
1241 replicates.
1242 **c-d. c)** Representative images of phalloidin- and DAPI-stained fat bodies. Arrows indicate GFP-
1243 positive cells with either MPC+ or MPC and *Nmnat* co-expression (MPC+, *Nmnat*+). The scale
1244 bar represents 20 $\mu$m. **d)** Quantification of the areas of GFP-positive cells with control, MPC+,
1245 *Nmnat* overexpression (*Nmnat*+), MPC and *Nmnat* co-expression (MPC+, *Nmnat*+). Data is
1246 presented as mean ± s.d. of five biological replicates, with 20 clonal cells analyzed for each of the
1247 indicated genetic manipulations.
1248 **e-f. e)** Representative images of Phalloidin and DAPI-stained fat body tissues. Arrows indicate
1249 GFP-positive cells showing MPC expression (MPC+); NDI and MPC expression (MPC+, NDI+);
1250 and NDX and MPC expression (MPC+, NDX+). The scale bar represents 20 $\mu$m. **f)** Quantification
1251 of the area of GFP-positive cells with control, MPC+, NDI expression (NDI+), NDI and MPC
1252 expression (MPC+, NDI+), NDX expression (NDX+), NDX and MPC co-expression (MPC+,
1253 NDX+). Data is presented as mean ± s.d. of five biological replicates, with 20 clonal cells analyzed
1254 for each of the indicated genetic manipulations.
1255 **g-h. g)** Representative bright field images of EV or MPC+ HepG2 spheroids cultured with $NAD^+$
1256 supplements (100 nM nicotinamide riboside or 1 $\mu$M NMN) as indicated. The scale bar represents
1257 200 $\mu$m. **h)** Quantification of spheroid area is presented as mean ± s.d. of 30 technical replicates.
1258 **i-j. i)** Representative images MPC+ or MPC+, NDI+ GFP-positive clones and of fat body cells
1259 stained with OPP (bottom). Clonal cells are mapped with dotted lines. The scale bar represents
1260 20 $\mu$m. **j)** Fold change in OPP intensity of 35 GFP-positive cells compared with adjacent wild-type
1261 cells. Data is presented as mean ± s.d.
1262 **k.** Relative accumulation of destabilized GFP (d2GFP) in spheroids of EV or MPC+ HepG2 cells
1263 treated with $NAD^+$ supplements (100 nM nicotinamide riboside or 1 $\mu$M NMN) as indicated.

1264 Unpaired t-tests, one-way ANOVA tests, or two-way ANOVA tests were performed to assess the
1265 statistical significance of the data, with p-values indicated in the graph where significance was
1266 observed.
1267
1268 **Supplementary Figure 7: Redox imbalance impedes protein synthesis and cell growth from**
1269 **elevated pyruvate metabolism in mitochondria. (related to main figure 5)**
1270 **a-b. a)** A schematic illustration of mitochondrial pyruvate metabolism and gluconeogenesis.
1271 Following are the abbreviations: PEP- phosphoenolpyruvate, F1,6BP- fructose-1, 6-
1272 bisphosphate, F6P- fructose-6-phosphate, G6P- glucose-6-phosphate, F6Pase- fructose
1273 bisphosphatase and G6PC- glucose-6-phosphatase **b)** Western blot analysis shows the
1274 expression levels of phosphorylated PDH (p-PDH), total PDH, G6PC, PEPCK2, PC, and tubulin
1275 in MPC-overexpressing (MPC+) HepG2 cells treated with 1 $\mu$g/ml doxycycline at the indicated
1276 time points.
1277 **c.** Schematic illustrating the regulation of PDH, PC, and gluconeogenesis by a network of
1278 cofactors and substrates. Following are the abbreviations: 1,3 BPG- 1,3-bisphosphoglycerate,
1279 G3P- glucose-3-phosphate, PGK- phosphoglycerate kinase, GAPDH- glyceraldehyde-3-
1280 phosphate dehydrogenase.
1281 **d.** Fold enrichment of acetyl-CoA in EV and MPC+ HepG2 cells. Data is presented as mean ±
1282 s.d. of three biological replicates using unpaired t-tests.
1283 **e.** The ratio of ATP to ADP in EV and MPC+ HepG2 cells. Data is presented as mean ± s.d. of
1284 three biological replicates using unpaired t-tests.
1285 **f-h.** Cellular concentrations of NADH **(f)** and $NAD^+$ **(g)** and NADH/$NAD^+$ ratios **(h)** in EV and MPC+
1286 HepG2 cells 24 hours after treatment with 1 $\mu$g/ml doxycycline. Data is presented as mean ± s.d.
1287 of three biological replicates using unpaired t-tests.
1288 **i.** Quantification of the areas of MPC+ HepG2 cells cultured with 2 nM gramicidin. Data is
1289 presented as mean ± s.d. of five biological replicates, with 25 randomly selected cells analyzed
1290 for each of the indicated groups.
1291 **j-k. j)** Representative bright field images of EV or MPC+ HepG2 spheroids with NDI expression
1292 (NDI+). The scale bar represents 200 $\mu$m. **k)** Quantification of spheroid areas is presented as
1293 mean ± s.d. of 30 technical replicates. Western blots show the efficiency of MPC expression.
1294 **l.** Quantification of the area of MPC-expressing HepG2 cells cultured with or without 100 nM
1295 duroquinone. Data is presented as average ± s.d. of five biological replicates, with each group

1296 consisting of 25 randomly selected cells. Data is presented as mean ± s.d. of three biological
1297 replicates.
1298 Unpaired t-tests, one-way ANOVA, or two-way ANOVA tests were performed to assess the
1299 statistical significance, with p-values indicated in the graph where significance was noted.
1300
1301 **Figure 6: Reduced amino acid abundance impairs size of MPC overexpressing cells.**
1302 **a.** A heat map of the abundances of amino acids in empty vector (EV) and MPC expressing
1303 (MPC+) HepG2 cells cultured under standard conditions. Color codes indicate relative
1304 abundances for each amino acid: Blue (low), Green (similar), and Yellow (high).
1305 **b-c. b)** Representative bright field images of EV or MPC+ HepG2 spheroids cultured with 2x or
1306 3x the recommended concentration of non-essential amino acids cocktail (NEAA). The scale bar
1307 represents 200 $\mu$m. **c)** Quantification of spheroid areas from EV and MPC+ HepG2 spheroids
1308 cultured with 2x or 3x NEAA. Data is presented as mean ± s.d. of 30 technical replicates.
1309 **d-e**. **d)** Representative images of phalloidin- and DAPI-stained fat body cells from animals fed a
1310 standard diet or a diet supplemented with 5x NEAA. Arrows indicate GFP-positive clones with
1311 MPC expression (MPC+). The scale bar represents 20 $\mu$m. **e)** Quantification of the area of MPC+
1312 fat body clonal cells. Data is presented as mean ± s.d. of five biological replicates, with each data
1313 point representing the average size of 20 clones collected from five male larvae.
1314 **f-g. f)** Representative images of phalloidin- and DAPI-stained fat body cells. Arrows indicate GFP-
1315 positive MPC+ clones and MPC+ and *slimfast* over-expression (MPC+, *Slif*+). The scale bar
1316 represents 20 $\mu$m. **g)** Quantification of the area of GFP-positive clones with control, MPC
1317 expression, *Slimfast* over-expression (*Slif*+) and MPC+ clones with *Slimfast* over-expression
1318 (MPC+, *Slif*+). Data presented as mean ± s.d. of five biological replicates, with each 20 clonal
1319 cells analyzed for each of the indicated genetic manipulations.
1320 **h.** Quantification of the cell areas of EV or MPC+ HepG2 cells cultured under standard conditions
1321 or with excess of the indicated amino acid—10 mM glycine, 5 mM alanine, 5 mM serine, 5 mM
1322 asparagine, 5 mM aspartic acid, 5 mM glutamic acid or 5 mM proline. Data is presented as mean
1323 ± s.d. of five biological replicates.
1324 **i-j. i)** Representative images of phalloidin- and DAPI-stained fat body cells. Arrows indicated GFP-
1325 positive cells with MPC expression (MPC+), *Got2* knock down (*Got2* KD), and *Got2* over-
1326 expression with MPC expression (MPC+, *Got2*+). **j)** Quantification of the area of GFP-positive
1327 clones with control, MPC expression (MPC+), *Got2* knock down (*Got2*-KD), *Got2* knock down
1328 with MPC expression (MPC+, *Got2*-KD), *Got2* over-expression (*Got2*+) and *Got2* over-expression

1329 with MPC expression (MPC+, *Got2*+). Data is presented as mean ± s.d. of five biological
1330 replicates, with each 20 clonal cells analyzed for each of the specified genetic manipulations.
1331 **k.** NADH/$NAD^+$ ratio in cells treated with 10 $\mu$M UK5099, 1 $\mu$M NMN, or 5 mM aspartate. Data is
1332 presented as mean ± s.d. of three biological replicates.
1333 **l-m. l)** Western blot analysis of puromycin-labeled (20 $\mu$g/ml puromycin for 30 minutes) nascent
1334 protein in EV or MPC+ HepG2 cells cultured with 10 $\mu$M UK5099, 1 $\mu$M NMN, or 5 mM aspartate.
1335 **m)** Quantification of intensities of puromycin labeling in EV and MPC+ cell lysates.
1336 Unpaired t-tests and one-way ANOVA tests were performed to evaluate the statistical significance
1337 of the data, and p-values are noted in the graph if significance is observed.
1338
1339 **Supplementary Figure 8: Reduced Aspartate/ Glutamate abundance impairs size of MPC**
1340 **overexpressing cells.**
1341 **a-b. a)** Representative bright field images of empty vector (EV) or MPC over-expressing (MPC+)
1342 HepG2 spheroids cultured with either 5 mM aspartate (Asp) or 5 mM glutamate (Glu). The scale
1343 bar represents 200 $\mu$m. **b)** Quantification of spheroid area is presented as mean ± s.d. of 30
1344 technical replicates.
1345 **c-d. c)** Representative bright field images of EV or MPC+ HepG2 spheroids with SLC1A3
1346 overexpression (SLC13A+). The scale bar represents 200 $\mu$m. **d)** Quantification of spheroid area
1347 is presented as mean ± s.d. of 30 technical replicates. Western blots show the efficiency of MPC
1348 expression.
1349 **e.** Quantification of d2GFP in EV or MPC+ HepG2 spheroids cultured under standard conditions
1350 or with three times the recommended concentration of non-essential amino acids cocktail (3X
1351 NEAA).
1352 **f.** Quantification of the areas of EV and MPC+ HepG2 cells and HepG2 cells GOT2 knock out
1353 (GOT2-KO) with or without MPC expression. Data is presented as mean ± s.d. of five biological
1354 replicates, with 25 randomly selected cells analyzed per replicate.
1355 **g-h**. **g)** Representative bright field images of EV, MPC+, GOT2+, and MPC+, GOT2+ HepG2
1356 spheroids. The scale bar represents 200 $\mu$m. **h)** Quantification of spheroid areas is presented as
1357 mean ± s.d. of 30 technical replicates. Western blots show the efficiency of GOT2 over-
1358 expression.
1359 Unpaired t-tests and one-way ANOVA tests were performed to evaluate the statistical significance
1360 of the data, and p-values are noted in the graph if significance is observed.
1361

1362 **Figure 7: Increased mitochondrial pyruvate transport rewires metabolism and redox status**
1363 **to reduce protein synthesis and cell size in rat primary hepatocytes.**
1364 **a.** Western blot analysis of MPC overexpression in cultured rat primary hepatocytes.
1365 **b.** Representative confocal images of rat primary hepatocytes expressing exogenous GFP or
1366 MPC. DIC images and DAPI staining of nuclei are also shown. Cell boundaries are marked with
1367 dotted lines. The scale bar represents 20 $\mu$m.
1368 **c.** Quantification of the areas of GFP and MPC expressing primary hepatocytes. Data is presented
1369 as mean ± s.d. of six biological replicates, with 20 hepatocytes analyzed for GFP and MPC+.
1370 **d.** Fluorescence intensity of puromycin-labeled nascent proteins in GFP and MPC+ primary
1371 hepatocytes. Data is presented as mean ± s.d. of six biological replicates, with 20 hepatocytes
1372 analyzed for each condition.
1373 **e.** Quantification of glucose in the culture media of primary hepatocytes transfected with GFP or
1374 MPC constructs, conditioned with 20 mM lactate and 2 mM pyruvate for four hours. 10 $\mu$M UK5099
1375 was used to inhibit MPC's downstream impact on gluconeogenesis. Data is presented as mean
1376 ± s.d. of 3 biological replicates.
1377 **f.** $NADH/NAD^+$ ratios in the cytoplasmic and mitochondrial fractions of GFP or MPC+ primary
1378 hepatocytes. Data is presented as mean ± s.d. of three biological replicates.
1379 **g.** Schematics illustrating the metabolic consequences of excess mitochondrial pyruvate in
1380 hepatocytes. Under normal conditions, mitochondrial pyruvate fuels the TCA cycle, maintaining
1381 redox balance and generating sufficient amino acids for cellular homeostasis. However, when
1382 mitochondrial pyruvate transport is increased and excess pyruvate is metabolized, both
1383 mitochondrial and cytoplasmic redox states are altered. This excess pyruvate enhances the
1384 activities of pyruvate carboxylase (PC), pyruvate dehydrogenase (PDH), and the TCA cycle,
1385 leading to an elevated $NADH/NAD^+$ ratio. The oxaloacetate produced by PC is converted into
1386 phosphoenolpyruvate via PEPCK2, promoting gluconeogenesis. This shift reduces the availability
1387 of aspartate and related amino acids necessary for protein synthesis, ultimately resulting in a
1388 reduction in cell size without impacting the canonical cell growth signaling pathways.
1389

1390 ## References

1391 Alkan, H. F., Walter, K. E., Luengo, A., Madreiter-Sokolowski, C. T., Stryeck, S., Lau, A. N., Al-
1392 Zoughbi, W., Lewis, C. A., Thomas, C. J., Hoefler, G., Graier, W. F., Madl, T., Vander
1393 Heiden, M. G., & Bogner-Strauss, J. G. (2018). Cytosolic Aspartate Availability Determines
1394 Cell Survival When Glutamine Is Limiting. *Cell Metab*, *28*(5), 706-720 e706.
1395 https://doi.org/10.1016/j.cmet.2018.07.021

1396 Amodeo, A. A., & Skotheim, J. M. (2016). Cell-Size Control. *Cold Spring Harb Perspect Biol*, *8*(4),
1397 a019083. https://doi.org/10.1101/cshperspect.a019083
1398 Arrese, E. L., & Soulages, J. L. (2010). Insect fat body: energy, metabolism, and regulation. *Annu*
1399 *Rev Entomol*, *55*, 207-225. https://doi.org/10.1146/annurev-ento-112408-085356
1400 Baena, E., Gandarillas, A., Vallespinos, M., Zanet, J., Bachs, O., Redondo, C., Fabregat, I.,
1401 Martinez, A. C., & de Alboran, I. M. (2005). c-Myc regulates cell size and ploidy but is not
1402 essential for postnatal proliferation in liver. *Proc Natl Acad Sci U S A*, *102*(20), 7286-7291.
1403 https://doi.org/10.1073/pnas.0409260102
1404 Baker, S. A., & Rutter, J. (2023). Metabolites as signalling molecules. *Nat Rev Mol Cell Biol*, *24*(5),
1405 355-374. https://doi.org/10.1038/s41580-022-00572-w
1406 Bensard, C. L., Wisidagama, D. R., Olson, K. A., Berg, J. A., Krah, N. M., Schell, J. C., Nowinski,
1407 S. M., Fogarty, S., Bott, A. J., Wei, P., Dove, K. K., Tanner, J. M., Panic, V., Cluntun, A.,
1408 Lettlova, S., Earl, C. S., Namnath, D. F., Vazquez-Arreguin, K., Villanueva, C. J., . . .
1409 Rutter, J. (2020). Regulation of Tumor Initiation by the Mitochondrial Pyruvate Carrier. *Cell*
1410 *Metab*, *31*(2), 284-300 e287. https://doi.org/10.1016/j.cmet.2019.11.002
1411 Birsoy, K., Wang, T., Chen, W. W., Freinkman, E., Abu-Remaileh, M., & Sabatini, D. M. (2015).
1412 An Essential Role of the Mitochondrial Electron Transport Chain in Cell Proliferation Is to
1413 Enable Aspartate Synthesis. *Cell*, *162*(3), 540-551.
1414 https://doi.org/10.1016/j.cell.2015.07.016
1415 Bjorklund, M. (2019). Cell size homeostasis: Metabolic control of growth and cell division. *Biochim*
1416 *Biophys Acta Mol Cell Res*, *1866*(3), 409-417.
1417 https://doi.org/10.1016/j.bbamcr.2018.10.002
1418 Bornstein, M. R., Tian, R., & Arany, Z. (2024). Human cardiac metabolism. *Cell Metab*, *36*(7),
1419 1456-1481. https://doi.org/10.1016/j.cmet.2024.06.003
1420 Bricker, D. K., Taylor, E. B., Schell, J. C., Orsak, T., Boutron, A., Chen, Y. C., Cox, J. E., Cardon,
1421 C. M., Van Vranken, J. G., Dephoure, N., Redin, C., Boudina, S., Gygi, S. P., Brivet, M.,
1422 Thummel, C. S., & Rutter, J. (2012). A mitochondrial pyruvate carrier required for pyruvate
1423 uptake in yeast, Drosophila, and humans. *Science*, *337*(6090), 96-100.
1424 https://doi.org/10.1126/science.1218099
1425 Chai, P., Lan, P., Li, S., Yao, D., Chang, C., Cao, M., Shen, Y., Ge, S., Wu, J., Lei, M., & Fan, X.
1426 (2022). Mechanistic insight into allosteric activation of human pyruvate carboxylase by
1427 acetyl-CoA. *Mol Cell*, *82*(21), 4116-4130 e4116.
1428 https://doi.org/10.1016/j.molcel.2022.09.033
1429 Cluntun, A. A., Badolia, R., Lettlova, S., Parnell, K. M., Shankar, T. S., Diakos, N. A., Olson, K.
1430 A., Taleb, I., Tatum, S. M., Berg, J. A., Cunningham, C. N., Van Ry, T., Bott, A. J., Krokidi,
1431 A. T., Fogarty, S., Skedros, S., Swiatek, W. I., Yu, X., Luo, B., . . . Drakos, S. G. (2021).
1432 The pyruvate-lactate axis modulates cardiac hypertrophy and heart failure. *Cell Metab*,
1433 *33*(3), 629-648 e610. https://doi.org/10.1016/j.cmet.2020.12.003
1434 Colombani, J., Raisin, S., Pantalacci, S., Radimerski, T., Montagne, J., & Leopold, P. (2003). A
1435 nutrient sensor mechanism controls Drosophila growth. *Cell*, *114*(6), 739-749.
1436 https://doi.org/10.1016/s0092-8674(03)00713-x
1437 Dang, C. V. (1999). c-Myc target genes involved in cell growth, apoptosis, and metabolism. *Mol*
1438 *Cell Biol*, *19*(1), 1-11. https://doi.org/10.1128/MCB.19.1.1
1439 DeBerardinis, R. J., & Thompson, C. B. (2012). Cellular metabolism and disease: what do
1440 metabolic outliers teach us? *Cell*, *148*(6), 1132-1144.
1441 https://doi.org/10.1016/j.cell.2012.02.032
1442 Deliu, L. P., Ghosh, A., & Grewal, S. S. (2017). Investigation of protein synthesis in Drosophila
1443 larvae using puromycin labelling. *Biol Open*, *6*(8), 1229-1234.
1444 https://doi.org/10.1242/bio.026294

1445 Edgar, B. A., & Orr-Weaver, T. L. (2001). Endoreplication cell cycles: more for less. *Cell*, *105*(3),
1446 297-306. https://doi.org/10.1016/s0092-8674(01)00334-8
1447 Fernandez-Caggiano, M., Kamynina, A., Francois, A. A., Prysyazhna, O., Eykyn, T. R.,
1448 Krasemann, S., Crespo-Leiro, M. G., Vieites, M. G., Bianchi, K., Morales, V., Domenech,
1449 N., & Eaton, P. (2020). Mitochondrial pyruvate carrier abundance mediates pathological
1450 cardiac hypertrophy. *Nat Metab*, *2*(11), 1223-1231. https://doi.org/10.1038/s42255-020-
1451 00276-5
1452 Ghosh-Choudhary, S., Liu, J., & Finkel, T. (2020). Metabolic Regulation of Cell Fate and Function.
1453 *Trends Cell Biol*, *30*(3), 201-212. https://doi.org/10.1016/j.tcb.2019.12.005
1454 Ginzberg, M. B., Chang, N., D'Souza, H., Patel, N., Kafri, R., & Kirschner, M. W. (2018). Cell size
1455 sensing in animal cells coordinates anabolic growth rates and cell cycle progression to
1456 maintain cell size uniformity. *Elife*, *7*. https://doi.org/10.7554/eLife.26957
1457 Gonzalez, A., & Hall, M. N. (2017). Nutrient sensing and TOR signaling in yeast and mammals.
1458 *EMBO J*, *36*(4), 397-408. https://doi.org/10.15252/embj.201696010
1459 Gonzalez, S., & Rallis, C. (2017). The TOR Signaling Pathway in Spatial and Temporal Control
1460 of Cell Size and Growth. *Front Cell Dev Biol*, *5*, 61.
1461 https://doi.org/10.3389/fcell.2017.00061
1462 Goodman, R. P., Markhard, A. L., Shah, H., Sharma, R., Skinner, O. S., Clish, C. B., Deik, A.,
1463 Patgiri, A., Hsu, Y. H., Masia, R., Noh, H. L., Suk, S., Goldberger, O., Hirschhorn, J. N.,
1464 Yellen, G., Kim, J. K., & Mootha, V. K. (2020). Hepatic NADH reductive stress underlies
1465 common variation in metabolic traits. *Nature*, *583*(7814), 122-126.
1466 https://doi.org/10.1038/s41586-020-2337-2
1467 Gospodaryov, D. V., Strilbytska, O. M., Semaniuk, U. V., Perkhulyn, N. V., Rovenko, B. M.,
1468 Yurkevych, I. S., Barata, A. G., Dick, T. P., Lushchak, O. V., & Jacobs, H. T. (2020).
1469 Alternative NADH dehydrogenase extends lifespan and increases resistance to
1470 xenobiotics in Drosophila. *Biogerontology*, *21*(2), 155-171.
1471 https://doi.org/10.1007/s10522-019-09849-8
1472 Gratz, S. J., Ukken, F. P., Rubinstein, C. D., Thiede, G., Donohue, L. K., Cummings, A. M., &
1473 O'Connor-Giles, K. M. (2014). Highly specific and efficient CRISPR/Cas9-catalyzed
1474 homology-directed repair in Drosophila. *Genetics*, *196*(4), 961-971.
1475 https://doi.org/10.1534/genetics.113.160713
1476 Gray, L. R., Sultana, M. R., Rauckhorst, A. J., Oonthonpan, L., Tompkins, S. C., Sharma, A., Fu,
1477 X., Miao, R., Pewa, A. D., Brown, K. S., Lane, E. E., Dohlman, A., Zepeda-Orozco, D.,
1478 Xie, J., Rutter, J., Norris, A. W., Cox, J. E., Burgess, S. C., Potthoff, M. J., & Taylor, E. B.
1479 (2015). Hepatic Mitochondrial Pyruvate Carrier 1 Is Required for Efficient Regulation of
1480 Gluconeogenesis and Whole-Body Glucose Homeostasis. *Cell Metab*, *22*(4), 669-681.
1481 https://doi.org/10.1016/j.cmet.2015.07.027
1482 Grewal, S. S. (2009). Insulin/TOR signaling in growth and homeostasis: a view from the fly world.
1483 *Int J Biochem Cell Biol*, *41*(5), 1006-1010. https://doi.org/10.1016/j.biocel.2008.10.010
1484 Hatting, M., Tavares, C. D. J., Sharabi, K., Rines, A. K., & Puigserver, P. (2018). Insulin regulation
1485 of gluconeogenesis. *Ann N Y Acad Sci*, *1411*(1), 21-35.
1486 https://doi.org/10.1111/nyas.13435
1487 Hausler, N., Browning, J., Merritt, M., Storey, C., Milde, A., Jeffrey, F. M., Sherry, A. D., Malloy,
1488 C. R., & Burgess, S. C. (2006). Effects of insulin and cytosolic redox state on glucose
1489 production pathways in the isolated perfused mouse liver measured by integrated 2H and
1490 13C NMR. *Biochem J*, *394*(Pt 2), 465-473. https://doi.org/10.1042/BJ20051174
1491 Henry, J. A., Couch, L. S., & Rider, O. J. (2024). Myocardial Metabolism in Heart Failure with
1492 Preserved Ejection Fraction. *J Clin Med*, *13*(5). https://doi.org/10.3390/jcm13051195

1493 Herzig, S., Raemy, E., Montessuit, S., Veuthey, J. L., Zamboni, N., Westermann, B., Kunji, E. R.,
1494 & Martinou, J. C. (2012). Identification and functional expression of the mitochondrial
1495 pyruvate carrier. *Science*, *337*(6090), 93-96. https://doi.org/10.1126/science.1218530
1496 Holecek, M. (2023a). Aspartic Acid in Health and Disease. *Nutrients*, *15*(18).
1497 https://doi.org/10.3390/nu15184023
1498 Holecek, M. (2023b). Roles of malate and aspartate in gluconeogenesis in various physiological
1499 and pathological states. *Metabolism*, *145*, 155614.
1500 https://doi.org/10.1016/j.metabol.2023.155614
1501 Iritani, B. M., & Eisenman, R. N. (1999). c-Myc enhances protein synthesis and cell size during B
1502 lymphocyte development. *Proc Natl Acad Sci U S A*, *96*(23), 13180-13185.
1503 https://doi.org/10.1073/pnas.96.23.13180
1504 Ito, K., Awano, W., Suzuki, K., Hiromi, Y., & Yamamoto, D. (1997). The Drosophila mushroom
1505 body is a quadruple structure of clonal units each of which contains a virtually identical set
1506 of neurones and glial cells. *Development*, *124*(4), 761-771.
1507 https://doi.org/10.1242/dev.124.4.761
1508 Jitrapakdee, S., St Maurice, M., Rayment, I., Cleland, W. W., Wallace, J. C., & Attwood, P. V.
1509 (2008). Structure, mechanism and regulation of pyruvate carboxylase. *Biochem J*, *413*(3),
1510 369-387. https://doi.org/10.1042/BJ20080709
1511 Jokinen, M. J., & Luukkonen, P. K. (2024). Hepatic mitochondrial reductive stress in the
1512 pathogenesis and treatment of steatotic liver disease. *Trends Pharmacol Sci*, *45*(4), 319-
1513 334. https://doi.org/10.1016/j.tips.2024.02.003
1514 Kast, A., Nishikawa, J., Yabe, T., Nanri, H., & Albert, H. (1988). Circadian rhythm of liver
1515 parameters (cellular structures, mitotic activity, glycogen and lipids in liver and serum)
1516 during three consecutive cycles in phenobarbital-treated rats. *Chronobiol Int*, *5*(4), 363-
1517 385. https://doi.org/10.3109/07420528809067782
1518 Kiesel, V. A., Sheeley, M. P., Coleman, M. F., Cotul, E. K., Donkin, S. S., Hursting, S. D., Wendt,
1519 M. K., & Teegarden, D. (2021). Pyruvate carboxylase and cancer progression. *Cancer*
1520 *Metab*, *9*(1), 20. https://doi.org/10.1186/s40170-021-00256-7
1521 Lang, F., Busch, G. L., Ritter, M., Volkl, H., Waldegger, S., Gulbins, E., & Haussinger, D. (1998).
1522 Functional significance of cell volume regulatory mechanisms. *Physiol Rev*, *78*(1), 247-
1523 306. https://doi.org/10.1152/physrev.1998.78.1.247
1524 Li, X., Zhao, X., Fang, Y., Jiang, X., Duong, T., Fan, C., Huang, C. C., & Kain, S. R. (1998).
1525 Generation of destabilized green fluorescent protein as a transcription reporter. *J Biol*
1526 *Chem*, *273*(52), 34970-34975. https://doi.org/10.1074/jbc.273.52.34970
1527 Lieu, E. L., Nguyen, T., Rhyne, S., & Kim, J. (2020). Amino acids in cancer. *Exp Mol Med*, *52*(1),
1528 15-30. https://doi.org/10.1038/s12276-020-0375-3
1529 Liu, S., Tan, C., Tyers, M., Zetterberg, A., & Kafri, R. (2022). What programs the size of animal
1530 cells? *Front Cell Dev Biol*, *10*, 949382. https://doi.org/10.3389/fcell.2022.949382
1531 Lloyd, A. C. (2013). The regulation of cell size. *Cell*, *154*(6), 1194-1205.
1532 https://doi.org/10.1016/j.cell.2013.08.053
1533 Lunt, S. Y., & Vander Heiden, M. G. (2011). Aerobic glycolysis: meeting the metabolic
1534 requirements of cell proliferation. *Annu Rev Cell Dev Biol*, *27*, 441-464.
1535 https://doi.org/10.1146/annurev-cellbio-092910-154237
1536 McCommis, K. S., Chen, Z., Fu, X., McDonald, W. G., Colca, J. R., Kletzien, R. F., Burgess, S.
1537 C., & Finck, B. N. (2015). Loss of Mitochondrial Pyruvate Carrier 2 in the Liver Leads to
1538 Defects in Gluconeogenesis and Compensation via Pyruvate-Alanine Cycling. *Cell Metab*,
1539 *22*(4), 682-694. https://doi.org/10.1016/j.cmet.2015.07.028
1540 McCommis, K. S., Kovacs, A., Weinheimer, C. J., Shew, T. M., Koves, T. R., Ilkayeva, O. R.,
1541 Kamm, D. R., Pyles, K. D., King, M. T., Veech, R. L., DeBosch, B. J., Muoio, D. M., Gross,

R. W., & Finck, B. N. (2020). Nutritional modulation of heart failure in mitochondrial pyruvate carrier-deficient mice. *Nat Metab*, *2*(11), 1232-1247. https://doi.org/10.1038/s42255-020-00296-1

Merker, M. P., Audi, S. H., Bongard, R. D., Lindemer, B. J., & Krenz, G. S. (2006). Influence of pulmonary arterial endothelial cells on quinone redox status: effect of hyperoxia-induced NAD(P)H:quinone oxidoreductase 1. *Am J Physiol Lung Cell Mol Physiol*, *290*(3), L607-619. https://doi.org/10.1152/ajplung.00302.2005

Metallo, C. M., & Vander Heiden, M. G. (2013). Understanding metabolic regulation and its influence on cell physiology. *Mol Cell*, *49*(3), 388-398. https://doi.org/10.1016/j.molcel.2013.01.018

Musselman, L. P., Fink, J. L., Ramachandran, P. V., Patterson, B. W., Okunade, A. L., Maier, E., Brent, M. R., Turk, J., & Baranski, T. J. (2013). Role of fat body lipogenesis in protection against the effects of caloric overload in Drosophila. *J Biol Chem*, *288*(12), 8028-8042. https://doi.org/10.1074/jbc.M112.371047

Pavlova, N. N., King, B., Josselsohn, R. H., Violante, S., Macera, V. L., Vardhana, S. A., Cross, J. R., & Thompson, C. B. (2020). Translation in amino-acid-poor environments is limited by tRNA(Gln) charging. *Elife*, *9*. https://doi.org/10.7554/eLife.62307

Petersen, M. C., Vatner, D. F., & Shulman, G. I. (2017). Regulation of hepatic glucose metabolism in health and disease. *Nat Rev Endocrinol*, *13*(10), 572-587. https://doi.org/10.1038/nrendo.2017.80

Reinke, H., & Asher, G. (2018). Liver size: Waning by day, Waxing by Night. *Hepatology*, *67*(1), 441-443. https://doi.org/10.1002/hep.29506

Rui, L. (2014). Energy metabolism in the liver. *Compr Physiol*, *4*(1), 177-197. https://doi.org/10.1002/cphy.c130024

Sanz, A., Soikkeli, M., Portero-Otin, M., Wilson, A., Kemppainen, E., McIlroy, G., Ellila, S., Kemppainen, K. K., Tuomela, T., Lakanmaa, M., Kiviranta, E., Stefanatos, R., Dufour, E., Hutz, B., Naudi, A., Jove, M., Zeb, A., Vartiainen, S., Matsuno-Yagi, A., . . . Jacobs, H. T. (2010). Expression of the yeast NADH dehydrogenase Ndi1 in Drosophila confers increased lifespan independently of dietary restriction. *Proc Natl Acad Sci U S A*, *107*(20), 9105-9110. https://doi.org/10.1073/pnas.0911539107

Saxton, R. A., & Sabatini, D. M. (2017). mTOR Signaling in Growth, Metabolism, and Disease. *Cell*, *168*(6), 960-976. https://doi.org/10.1016/j.cell.2017.02.004

Schell, J. C., Olson, K. A., Jiang, L., Hawkins, A. J., Van Vranken, J. G., Xie, J., Egnatchik, R. A., Earl, E. G., DeBerardinis, R. J., & Rutter, J. (2014). A role for the mitochondrial pyruvate carrier as a repressor of the Warburg effect and colon cancer cell growth. *Mol Cell*, *56*(3), 400-413. https://doi.org/10.1016/j.molcel.2014.09.026

Schell, J. C., Wisidagama, D. R., Bensard, C., Zhao, H., Wei, P., Tanner, J., Flores, A., Mohlman, J., Sorensen, L. K., Earl, C. S., Olson, K. A., Miao, R., Waller, T. C., Delker, D., Kanth, P., Jiang, L., DeBerardinis, R. J., Bronner, M. P., Li, D. Y., . . . Rutter, J. (2017). Control of intestinal stem cell function and proliferation by mitochondrial pyruvate metabolism. *Nat Cell Biol*, *19*(9), 1027-1036. https://doi.org/10.1038/ncb3593

Schmoller, K. M., & Skotheim, J. M. (2015). The Biosynthetic Basis of Cell Size Control. *Trends Cell Biol*, *25*(12), 793-802. https://doi.org/10.1016/j.tcb.2015.10.006

Shen, Y., Liu, W., Zuo, J., Han, J., & Zhang, Z. C. (2021). Protocol for visualizing newly synthesized proteins in primary mouse hepatocytes. *STAR Protoc*, *2*(3), 100616. https://doi.org/10.1016/j.xpro.2021.100616

Siess, E. A., Brocks, D. G., Lattke, H. K., & Wieland, O. H. (1977). Effect of glucagon on metabolite compartmentation in isolated rat liver cells during gluconeogenesis from lactate. *Biochem J*, *166*(2), 225-235. https://doi.org/10.1042/bj1660225

1591 Sinturel, F., Gerber, A., Mauvoisin, D., Wang, J., Gatfield, D., Stubblefield, J. J., Green, C. B.,
1592 Gachon, F., & Schibler, U. (2017). Diurnal Oscillations in Liver Mass and Cell Size
1593 Accompany Ribosome Assembly Cycles. *Cell*, *169*(4), 651-663 e614.
1594 https://doi.org/10.1016/j.cell.2017.04.015
1595 Stacpoole, P. W. (2017). Therapeutic Targeting of the Pyruvate Dehydrogenase
1596 Complex/Pyruvate Dehydrogenase Kinase (PDC/PDK) Axis in Cancer. *J Natl Cancer Inst*,
1597 *109*(11). https://doi.org/10.1093/jnci/djx071
1598 Stine, Z. E., Walton, Z. E., Altman, B. J., Hsieh, A. L., & Dang, C. V. (2015). MYC, Metabolism,
1599 and Cancer. *Cancer Discov*, *5*(10), 1024-1039. https://doi.org/10.1158/2159-8290.CD-15-
1600 0507
1601 Sugden, M. C., & Holness, M. J. (2011). The pyruvate carboxylase-pyruvate dehydrogenase axis
1602 in islet pyruvate metabolism: Going round in circles? *Islets*, *3*(6), 302-319.
1603 https://doi.org/10.4161/isl.3.6.17806
1604 Sullivan, L. B., Gui, D. Y., Hosios, A. M., Bush, L. N., Freinkman, E., & Vander Heiden, M. G.
1605 (2015). Supporting Aspartate Biosynthesis Is an Essential Function of Respiration in
1606 Proliferating Cells. *Cell*, *162*(3), 552-563. https://doi.org/10.1016/j.cell.2015.07.017
1607 Sullivan, L. B., Luengo, A., Danai, L. V., Bush, L. N., Diehl, F. F., Hosios, A. M., Lau, A. N.,
1608 Elmiligy, S., Malstrom, S., Lewis, C. A., & Vander Heiden, M. G. (2018). Aspartate is an
1609 endogenous metabolic limitation for tumour growth. *Nat Cell Biol*, *20*(7), 782-788.
1610 https://doi.org/10.1038/s41556-018-0125-0
1611 Tan, C., Ginzberg, M. B., Webster, R., Iyengar, S., Liu, S., Papadopoli, D., Concannon, J., Wang,
1612 Y., Auld, D. S., Jenkins, J. L., Rost, H., Topisirovic, I., Hilfinger, A., Derry, W. B., Patel, N.,
1613 & Kafri, R. (2021). Cell size homeostasis is maintained by CDK4-dependent activation of
1614 p38 MAPK. *Dev Cell*, *56*(12), 1756-1769 e1757.
1615 https://doi.org/10.1016/j.devcel.2021.04.030
1616 Tom Dieck, S., Muller, A., Nehring, A., Hinz, F. I., Bartnik, I., Schuman, E. M., & Dieterich, D. C.
1617 (2012). Metabolic labeling with noncanonical amino acids and visualization by
1618 chemoselective fluorescent tagging. *Curr Protoc Cell Biol*, *Chapter 7*, 7 11 11-17 11 29.
1619 https://doi.org/10.1002/0471143030.cb0711s56
1620 Toshniwal, A. G., Gupta, S., Mandal, L., & Mandal, S. (2019). ROS Inhibits Cell Growth by
1621 Regulating 4EBP and S6K, Independent of TOR, during Development. *Dev Cell*, *49*(3),
1622 473-489 e479. https://doi.org/10.1016/j.devcel.2019.04.008
1623 Ugrankar-Banerjee, R., Tran, S., Bowerman, J., Kovalenko, A., Paul, B., & Henne, W. M. (2023).
1624 The fat body cortical actin network regulates Drosophila inter-organ nutrient trafficking,
1625 signaling, and adipose cell size. *Elife*, *12*. https://doi.org/10.7554/eLife.81170
1626 van Riggelen, J., Yetil, A., & Felsher, D. W. (2010). MYC as a regulator of ribosome biogenesis
1627 and protein synthesis. *Nat Rev Cancer*, *10*(4), 301-309. https://doi.org/10.1038/nrc2819
1628 Vander Heiden, M. G., Cantley, L. C., & Thompson, C. B. (2009). Understanding the Warburg
1629 effect: the metabolic requirements of cell proliferation. *Science*, *324*(5930), 1029-1033.
1630 https://doi.org/10.1126/science.1160809
1631 Villalobos-Cantor, S., Barrett, R. M., Condon, A. F., Arreola-Bustos, A., Rodriguez, K. M., Cohen,
1632 M. S., & Martin, I. (2023). Rapid cell type-specific nascent proteome labeling in Drosophila.
1633 *Elife*, *12*. https://doi.org/10.7554/eLife.83545
1634 Wang, X., Shen, X., Yan, Y., & Li, H. (2021). Pyruvate dehydrogenase kinases (PDKs): an
1635 overview toward clinical applications. *Biosci Rep*, *41*(4).
1636 https://doi.org/10.1042/BSR20204402
1637 Wei, P., Bott, A. J., Cluntun, A. A., Morgan, J. T., Cunningham, C. N., Schell, J. C., Ouyang, Y.,
1638 Ficarro, S. B., Marto, J. A., Danial, N. N., DeBerardinis, R. J., & Rutter, J. (2022).
1639 Mitochondrial pyruvate supports lymphoma proliferation by fueling a glutamate pyruvate

transaminase 2-dependent glutaminolysis pathway. *Sci Adv*, *8*(39), eabq0117. https://doi.org/10.1126/sciadv.abq0117

Wei, Z., Liu, X., Cheng, C., Yu, W., & Yi, P. (2020). Metabolism of Amino Acids in Cancer. *Front Cell Dev Biol*, *8*, 603837. https://doi.org/10.3389/fcell.2020.603837

Weiss, R. C., Menezes, T. N., & McCommis, K. S. (2023). Metabolic Drivers and Rescuers of Heart Failure. *Mo Med*, *120*(5), 354-358. https://www.ncbi.nlm.nih.gov/pubmed/37841572

Xue, Y. W., Itoh, H., Dan, S., & Inoue, M. (2022). Gramicidin A accumulates in mitochondria, reduces ATP levels, induces mitophagy, and inhibits cancer cell growth. *Chem Sci*, *13*(25), 7482-7491. https://doi.org/10.1039/d2sc02024f

Yiew, N. K. H., & Finck, B. N. (2022). The mitochondrial pyruvate carrier at the crossroads of intermediary metabolism. *Am J Physiol Endocrinol Metab*, *323*(1), E33-E52. https://doi.org/10.1152/ajpendo.00074.2022

Yoo, H. C., Yu, Y. C., Sung, Y., & Han, J. M. (2020). Glutamine reliance in cell metabolism. *Exp Mol Med*, *52*(9), 1496-1516. https://doi.org/10.1038/s12276-020-00504-8

Zangari, J., Petrelli, F., Maillot, B., & Martinou, J. C. (2020). The Multifaceted Pyruvate Metabolism: Role of the Mitochondrial Pyruvate Carrier. *Biomolecules*, *10*(7). https://doi.org/10.3390/biom10071068

Zhang, S., Zatulovskiy, E., Arand, J., Sage, J., & Skotheim, J. M. (2022). The cell cycle inhibitor RB is diluted in G1 and contributes to controlling cell size in the mouse liver. *Front Cell Dev Biol*, *10*, 965595. https://doi.org/10.3389/fcell.2022.965595

Zhang, Y., Taufalele, P. V., Cochran, J. D., Robillard-Frayne, I., Marx, J. M., Soto, J., Rauckhorst, A. J., Tayyari, F., Pewa, A. D., Gray, L. R., Teesch, L. M., Puchalska, P., Funari, T. R., McGlauflin, R., Zimmerman, K., Kutschke, W. J., Cassier, T., Hitchcock, S., Lin, K., . . . Abel, E. D. (2020). Mitochondrial pyruvate carriers are required for myocardial stress adaptation. *Nat Metab*, *2*(11), 1248-1264. https://doi.org/10.1038/s42255-020-00288-1

Zheng, H., Yang, X., & Xi, Y. (2016). Fat body remodeling and homeostasis control in Drosophila. *Life Sci*, *167*, 22-31. https://doi.org/10.1016/j.lfs.2016.10.019

Zhu, J., & Thompson, C. B. (2019). Metabolic regulation of cell growth and proliferation. *Nat Rev Mol Cell Biol*, *20*(7), 436-450. https://doi.org/10.1038/s41580-019-0123-5

1686 **Table 1- Key Resource Table**

| Reagent type (species) or resource | Designation | Source or reference | Identifiers | Additional Information |
|---|---|---|---|---|
| Strain (*Drosophila melanogaster*) | *UAS-MPC1-P2A-MPC2* | Schell et al., 2017 | BDSC, #84087 | Expresses Drosophila *Mpc1* and *Mpc2* cDNA separated by P2A cleavage site |
| Strain (*D. melanogaster*) | *hs-Flp1.22* | Bloomington *Drosophila* Stock Center | BDSC, #77928 | |
| Strain (*D. melanogaster*) | *Act>CD2>Gal4, UAS-GFP* | Bloomington *Drosophila* Stock Center | BDSC, #4413 | Ay-Gal4 fly stock used to induce mosaics in fat body |
| Strain (*D. melanogaster*) | *CG-Gal4* | Bloomington *Drosophila* Stock Center | BDSC, #7011 | |
| Strain (*D. melanogaster*) | *UAS-S6k*$^{STDETE}$ | Bloomington *Drosophila* Stock Center | BDSC, #6914 | Drives constitutively active *S6k* expression |
| Strain (*D. melanogaster*) | *UAS-Rheb*$^{PA}$ | Bloomington *Drosophila* Stock Center | BDSC, #9689 | Drives Rheb overexpression |
| Strain (*D. melanogaster*) | *UAS-Myc*$^{OE}$ | Bloomington *Drosophila* Stock Center | BDSC, #9675 | Drives *Myc* overexpression |
| Strain (*D. melanogaster*) | *UAS-JF01761* | Bloomington *Drosophila* Stock Center | BDSC, #25783 | Drives Myc dsRNA, used as *UAS-Myc*$^{RNAi}$ |
| Strain (*D. melanogaster*) | *UAS-PI3K93E*$^{.ExcelI}$ | Bloomington *Drosophila* Stock Center | BDSC, #8287 | Drives *PI3K93* overexpression |
| Strain (*D. melanogaster*) | *UAS-Pi3K92E.A2860C* | Bloomington *Drosophila* Stock Center | BDSC, #8288 | Drives *PI3K93* dominant negative |
| Strain (*D. melanogaster*) | *UAS-Tsc1*$^{RNAi}$ | Bloomington *Drosophila* Stock Center | BDSC, #31314 | Drives *Tsc1* dsRNA, used as *UAS-Tsc1*$^{RNAi}$ |

| | | | | |
|---|---|---|---|---|
| Strain (*D. melanogaster*) | *UAS-hPC* | Bloomington *Drosophila* Stock Center | BDSC, #77928 | Drives human PC cDNA |
| Strain (*D. melanogaster*) | *UAS-HMC04104* | Bloomington *Drosophila* Stock Center | BDSC, #56883 | Drives *Pc* dsRNA, used as *UAS-PC*$^{RNAi}$ |
| Strain (*D. melanogaster*) | *UAS-HMS00200* | Bloomington *Drosophila* Stock Center | BDSC, #36915 | Drives *Pepck2* dsRNA, used as *UAS-Pepck2*$^{RNAi}$ |
| Strain (*D. melanogaster*) | *UAS-HMC03445* | Bloomington *Drosophila* Stock Center | BDSC, #51871 | Drives *Fbp* dsRNA, used as *UAS-Fbp*$^{RNAi}$ |
| Strain (*D. melanogaster*) | *UAS-GL00009* | Bloomington *Drosophila* Stock Center | BDSC, #35142 | Drives *Pdk* dsRNA, used as *UAS-Pdk*$^{RNAi}$ |
| Strain (*D. melanogaster*) | *UAS-NMNAT* | Bloomington *Drosophila* Stock Center | BDSC, #39702 | Drives *Nmnat* cDNA |
| Strain (*D. melanogaster*) | *UAS-CintNDX* | Bloomington *Drosophila* Stock Center | BDSC, #93883 | Drives *Cionia intestinalis* NDX cDNA |
| Strain (*D. melanogaster*) | *UAS-ScerNDI1* | Bloomington *Drosophila* Stock Center | BDSC, #93878 | Drives *Saccharomyces cerevisiae* NDI cDNA |
| Strain (*D. melanogaster*) | *UAS-slif* | Bloomington *Drosophila* Stock Center | BDSC, #52661 | Drives *slimfast* cDNA |
| Strain (*D. melanogaster*) | *UAS-HMS05873* | Bloomington *Drosophila* Stock Center | BDSC, #78778 | Drives *Got2* dsRNA, used as *UAS-Got2*$^{RNAi}$ |
| Strain (*D. melanogaster*) | *UAS-Mpc1*$^{RNAi}$ | Bricker et. al, 2012 | | Drives *Mpc1* dsRNA |
| Strain (*D. melanogaster*) | *UAS-Pdha*$^{RNAi}$ | National Institute of Genetics, Japan | NIG 7010R-3 | Drives *Pdha* dsRNA |
| Strain (*D. melanogaster*) | *UAS-Dlat*$^{RNAi}$ | National Institute of Genetics, Japan | NIG 5261R-3 | Drives *Dlat* dsRNA |
| Strain (*D. melanogaster*) | *w*$^{1118}$ | Bloomington *Drosophila* Stock Center | BDSC:3605 | Wild-type fly strain |
| Strain (*D. melanogaster*) | *UAS-GOT2* | This paper | see materials and methods | Drives *Got2* cDNA |

| | | | | |
|---|---|---|---|---|
| Strain (*D. melanogaster*) | *Pcb KO* | This paper | see materials and methods | *Pcb* CRISPR deletion fly stock, |
| Strain (*D. melanogaster*) | *Pepck2 KO* | This paper | see materials and methods | *Pepck2* CRISPR deletion fly stock, |
| Cell line (Homo *sapiens*) | HepG2 | ATCC | Cat# HB-8065 | a hepatocellular carcinoma cell line |
| Primary hepatocytes | Cryopreserved Rat Hepatocytes | Lonza | Cat# RWCP01 | Plateable, Rat Wistar Hannover Hepatocytes, cryopreserved |
| Antibody | anti-puromycin [3RH11] (host: mouse monoclonal) | Kerafast | Cat# EQ0001 | Dilution factor 1:1000 for western blot And 1:200 for immunofluorescence |
| Antibody | anti-MPC1 (*Drosophila*) (host: rabbit monoclonal) | gift from R. Kletzein | | Dilution factor 1:200 for immunofluorescence |
| Antibody | anti-MPC2 (*Drosophila*) (host: rabbit monoclonal) | gift from R. Kletzein | | Dilution factor 1:200 for immunofluorescence |
| Antibody | anti-p-S6 (host: rabbit monoclonal) | gift from A. Teleman | | Dilution factor 1:200 for immunofluorescence |
| Antibody | anti-dFoxo (host: rabbit monoclonal) | gift from P. Bellosta | | Dilution factor 1:500 for immunofluorescence |
| Antibody | anti-p-4EBP (host: rabbit monoclonal) | Cell Signaling Technologies | Cat# 2855 | Dilution factor 1:1000 for western blot And 1:500 for immunofluorescence |
| Antibody | anti-p-eIF2$\alpha$ (host: rabbit monoclonal) | Cell Signaling Technologies | Cat# 9721 | Dilution factor 1:500 for immunofluorescence |

| | | | | |
|---|---|---|---|---|
| Antibody | Cy3 conjugated anti-rabbit (host: donkey polyclonal) | Jacksons Immuno Research Laboratories | Cat# 711–165-152 | Dilution factor 1:400 for immunofluorescence |
| Antibody | Cy3 conjugated anti-mouse (host: donkey polyclonal) | Jacksons Immuno Research Laboratories | Cat# 115-165-166 | Dilution factor 1:400 for immunofluorescence |
| Antibody | anti-MPC1 (host: rabbit monoclonal) | Cell Signaling Technologies | Cat# 14462 | Dilution factor 1:1000 for western blot |
| Antibody | anti-MPC2 (host: rabbit monoclonal) | Cell Signaling Technologies | Cat# 46141 | Dilution factor 1:1000 for western blot |
| Antibody | anti-PDH (host: rabbit monoclonal) | Cell Signaling Technologies | Cat# 3205 | Dilution factor 1:1000 for western blot |
| Antibody | anti- p-PDH (host: rabbit monoclonal) | Cell Signaling Technologies | Cat# 31866 | Dilution factor 1:1000 for western blot |
| Antibody | anti-PC (host: rabbit monoclonal) | Cell Signaling Technologies | Cat# 66470 | Dilution factor 1:1000 for western blot |
| Antibody | anti-PEPCK2 (D3E11) (host: rabbit monoclonal) | Cell Signaling Technologies | Cat# 8565 | Dilution factor 1:1000 for western blot |
| Antibody | anti-Got2 (host: rabbit monoclonal) | Sigma | Cat# HPA018139 | Dilution factor 1:1000 for western blot |
| Antibody | anti-tubulin (DM1A) (host: mouse monoclonal) | Cell Signaling Technologies | Cat# 3873 | Dilution factor 1:1000 for western blot |
| Antibody | anti- Flag M2 (host: mouse monoclonal) | Sigma Aldrich | Cat# F1800 | Dilution factor 1:10000 for western blot 1:1000 for |
| Antibody | IRDye 680RD anti-mouse (host: Donkey monoclonal) | Li-COR | Cat# 926-68072 | Dilution factor 1:5000 for western blot immunofluorescence |
| Antibody | IRDye 800RD anti-Rabbit (host: Donkey monoclonal) | Li-COR | Cat# 926-32213 | Dilution factor 1:5000 for western blot |
| Recombinant DNA reagent | pUAST-aatB | | | |

| | | | | |
|---|---|---|---|---|
| Recombinant DNA reagent | pLVX-TetOne-Zeocin | Takara | | |
| Recombinant DNA reagent | Gag-Pol | Addgene | | |
| Recombinant DNA reagent | VSVG | Addgene | | |
| Recombinant DNA reagent | pMD2.G | Addgene | | |
| Recombinant DNA reagent | pLenti-CMV-Blast | Addgene | Cat# 17486 | |
| Recombinant DNA reagent | pLVX-TetOne-HA-MPC2-P2A-T2A-MPC1-FLAG-Zeo | This paper | HA-tagged MPC2 and Flag-tagged MPC1 cDNA separated by P2A/T2A cleavage site cloned into pLenti-CMV-Blast | |
| Recombinant DNA reagent | pLenti-CMV-PC-V5-Blast | This paper | V5-tagged PC cDNA cloned into pLenti-CMV-Blast | |
| Recombinant DNA reagent | pLenti-CMV-GOT2-V5-Blast | This paper | V5-tagged GOT2 cDNA cloned into pLenti-CMV-Blast | |
| Recombinant DNA reagent | PB-CAG-GFPd2 | Addgene | Cat# 115665 | |
| Recombinant DNA reagent | PMXS-NDI | Addgene | Cat# 72876 | |
| Recombinant DNA reagent | pLenti-CMV-d2GFP-Blast | This paper | d2GFP cloned into pLenti-CMV-Blast | |
| Recombinant DNA reagent | pLenti-CMV-NDI-V5-Blast | This paper | V5-tagged NDI cloned into pLenti-CMV-Blast | |
| Recombinant DNA reagent | pLenti-CMV-SLC1A3-V5-Blast | This paper | V5-tagged SLC1A3 cDNA cloned into pLenti-CMV-Blast; see materials and methods | |
| Recombinant DNA reagent | lentiCRISPRv2-blasticidin | Addgene | Cat# 83480 | |
| Recombinant DNA reagent | lentiCRISPRv2-hPCg5e-blast | This paper | sgRNA targeting human PC exon 5 in lentiCRISPRv2 vector; see Materials and methods | |

| | | | | |
|---|---|---|---|---|
| Recombinant DNA reagent | lentiCRISPRv2-hPCg6e-blast | This paper | sgRNA targeting human PC exon 6 in lentiCRISPRv2 vector; see Materials and methods | |
| Recombinant DNA reagent | lentiCRISPRv2-hPEPCK2g2e-blast | This paper | sgRNA targeting human PEPCK2 exon 2 in lentiCRISPRv2 vector; see Materials and methods | |
| Recombinant DNA reagent | lentiCRISPRv2-hPEPCK2g3e-blast | This paper | sgRNA targeting human PEPCK2 exon 3 in lentiCRISPRv2 vector; see Materials and methods | |
| Recombinant DNA reagent | lentiCRISPRv2-hGOT2ga-blast | This paper | sgRNA a targeting human GOT2 in lentiCRISPRv2 vector; see Materials and methods | |
| Recombinant DNA reagent | lentiCRISPRv2-hGOT2gb-blast | This paper | sgRNA b targeting human GOT2 in lentiCRISPRv2 vector; see Materials and methods | |
| Recombinant DNA reagent | pUAST-aatB-*dGOT2* | This paper | *dGOT2* cDNA was cloned into pLenti-CMV-Blast | |
| Commercial assay or kit | Annexin V/PI staining kit | Molecular Probes | Cat# V13241 | |
| Commercial assay or kit | Click-iT Plus OPP Alexa Fluor 594 kit | Molecular Probes | Cat# C10457 | |
| Commercial assay or kit | Click-iT HPG Alexa Fluor 594 kit | Molecular Probes | Cat# C10429 | |
| Commercial assay or kit | Triglycerides Reagen | Thermo Fisher Scientific | Cat# TR22421 | |
| Commercial assay or kit | BCA Protein Assay Reagent | Thermo Fisher Scientific | Cat# 23225 | |

| | | | | |
|---|---|---|---|---|
| Commercial assay or kit | TRIzol Reagent | Thermo Fisher Scientific | Cat# 15596026 | |
| Commercial assay or kit | Amplite Fluorimetric NAD/NADH ratio assay kit | AAT Bioquest | Cat# 15263 | |
| Commercial assay or kit | Click-iT Plus EdU Alexa Fluor 594 | Molecular Probes | Cat# C10639 | |
| Commercial assay or kit | NucleoSpin RNA kit | Takara Bio USA, Inc | Cat# 740955.50 | |
| Commercial assay or kit | Autokit Glucose reagent | Wako | Cat# 997-03001 | |
| Commercial assay or kit | Amplex Red Glucose Assay Kit | Thermo Fisher Scientific | Cat# A22189 | |
| Chemical compound, drug | paraformaldehyde | Sigma Aldrich | Cat# P6148 | |
| Chemical compound, drug | Rhodamine Phalloidin | Thermo Scientific | Cat# R418 | |
| Chemical compound, drug | DAPI-supplemented VectaShield | Vector Labs | Cat# H1200 | |
| Chemical compound, drug | Normal Goat Serum | Jackson ImmunoResearch Laboratories | Cat# 005-000-121 | |
| Chemical compound, drug | Human Plasma-Like Medium | Gibco | Cat# 765090 | |
| Chemical compound, drug | doxycycline | Sigma Aldrich | Cat# #D5207 | |
| Chemical compound, drug | UK5099 | Sigma Aldrich | Cat# PZ0160-5MG | |
| Chemical compound, drug | glycine | Sigma Aldrich | Cat# G7403 | |
| Chemical compound, drug | alanine | Sigma Aldrich | Cat# A7469 | |
| Chemical compound, drug | asparagine | Sigma Aldrich | Cat# A4159 | |

| | | | | |
|---|---|---|---|---|
| Chemical compound, drug | aspartic acid | Sigma Aldrich | Cat# A7219 | |
| Chemical compound, drug | glutamic acid | Sigma Aldrich | Cat# G8415 | |
| Chemical compound, drug | proline | Sigma Aldrich | Cat# P5607 | |
| Chemical compound, drug | serine | Sigma Aldrich | Cat# S4311 | |
| Chemical compound, drug | AZD7545 | MedChemExpress, | Cat# HY-16082 | |
| Chemical compound, drug | dichloroacetate | Sigma Aldrich | Cat# 347795 | |
| Chemical compound, drug | duroquinone | Sigma Aldrich | Cat# D223204 | |
| Chemical compound, drug | gramicidin | Sigma Aldrich | Cat# G5002 | |
| Chemical compound, drug | nicotinamide riboside | Sigma Aldrich | Cat# SMB00907 | |
| Chemical compound, drug | MEM non-essential amino acids | Gibco | Cat# 11140050 | |
| Chemical compound, drug | Nicotinamide mononucleotide | Sigma Aldrich | Cat# N3501 | |
| Chemical compound, drug | Vybrant® DyeCycle™ Violet stain | Molecular Probes | Cat# V35003 | |
| Chemical compound, drug | Eagle's Minimal Essential Medium | ATCC | Cat# 30-2003 | |
| Chemical compound, drug | Camptothecin | MedChemExpress | Cat# HY-16560 | |
| Chemical compound, drug | Shields Sang M3 Insect Media | Sigma Aldrich | Cat# S8398 | |
| Chemical compound, drug | puromycin | Sigma Aldrich | Cat# P4512 | |

| | | | | |
|---|---|---|---|---|
| Chemical compound, drug | methionine-free DMEM | Gibco | Cat# 21013024 | |
| Chemical compound, drug | LipidTOX Red | Invitrogen | Cat# H34351 | |
| Chemical compound, drug | SuperScript II Reverse Transcriptase | Molecular Probes | Cat# 18064-022 | |
| Chemical compound, drug | PowerUp SYBR Green Master Mix | Applied Biosystems | Cat# 2828831 | |
| Chemical compound, drug | $^{13}$C Glucose | Millipore Sigma | Cat# 389374 | |
| Chemical compound, drug | DMEM, no glucose, no glutamine and no phenol red | Gibco | Cat# A1443001 | |
| Chemical compound, drug | Sodium L-Lactate-C13 solution | Millipore Sigma | Cat# 490040 | |
| Chemical compound, drug | Hepatocyte Plating Medium | Lonza | Cat# MP100 | |
| Chemical compound, drug | Hepatocyte Basal Medium | Lonza | Cat# CC-4182 | |
| Chemical compound, drug | Lipofectamine 3000 | Invitrogen | Cat# L3000001 | |
| Chemical compound, drug | Triton X-100 | Sigma Aldrich | Cat# X100 | |
| Chemical compound, drug | FBS | Sigma Aldrich | Cat# F0926 | |
| Chemical compound, drug | PenStrep | Thermo Fisher Scientific | Cat# 15140 | |
| Chemical compound, drug | NP-40 | Millipore | Cat# 492018 | |
| Chemical compound, drug | sodium deoxycholate | Sigma Aldrich | Cat# D6750 | |

| | | | | |
|---|---|---|---|---|
| Chemical compound, drug | SDS | Sigma Aldrich | Cat# L3771 | |
| Chemical compound, drug | EDTA | Sigma Aldrich | Cat# E9884 | |
| Chemical compound, drug | Tris-HCl | Roche | Cat# 10812846001 | |
| Software | FIJI | NIH Image | RRID: SCR_002285 | https://fiji.sc/ |
| Software | Prism | GraphPad | RRID:SCR_002798 | http://www.graphpad.com/ |
| Software | FlowJo | FlowJo | RRID: SCR_008520 | https://www.flowjo.com/solutions/flowjo/downloads |
| other | Ultra Low Cluster, 96 well, Ultra Low Attachment Polystyrene | Costar | Cat# 7007 | |
| other | Dumont 5 forceps | Fine Science Tools | Cat# 11254-20 | |

1687
1688
1689 **Table 2-Oligos for *Drosophila* genes**
1690

| Name of gene | Sequence | Additional Information |
|---|---|---|
| *rp49* | GACGCTTCAAGGGA CAGTATCTG | QPCR- forward primer |
| *rp49* | AAACGCGGTTCTGCATGA | QPCR- reverse primer |
| *Pyk* | TCTTGGTGACTGGCTGAAGG | QPCR- forward primer |
| *Pyk* | GCCGTTCTTCTTTCCGAC | QPCR- reverse primer |
| *Mpc1* | CTCAAAGGAGTGGCGGGATT | QPCR- forward primer |
| *Mpc1* | CAGGGTCAGAGCCAATGTCA | QPCR- reverse primer |
| *Mpc2* | CAGCTGGTCCCAAGACGATA | QPCR- forward primer |
| *Mpc2* | CGCATCCAGACACGGAGAT | QPCR- reverse primer |

| | | |
|---|---|---|
| *Pdha* | ATCATCTCGGCGTACCGTG | QPCR- forward primer |
| *Pdha* | GCCTCCGTAGAAGTTCGGTG | QPCR- reverse primer |
| *Dlat* | CTGGAGTCCAAGACACAACTG | QPCR- forward primer |
| *Dlat* | TGAAGTCGTTTACAGAGACGC | QPCR- reverse primer |
| *Pepck* | TGATCCCGAACGCACCATC | QPCR- forward primer |
| *Pepck* | CTCAGGGCGAAGCACTTCTT | QPCR- reverse primer |
| *Pepck2* | AATGCTGGGTAACTGGATAGCC | QPCR- forward primer |
| *Pepck2* | GGTGCGACCTTTCATGCAG | QPCR- reverse primer |
| *Pc-KO* | ATACATTTAAGTCCTAGGC | CRISPR 5' guide |
| *Pc-KO* | TCGATTGATCCTGGAAACA | CRISPR 3' guide |
| *Pepck2-KO* | AAAGGGTGCACATCTGTGA | CRISPR 5' guide |
| *Pepck2-KO* | TTTGGGGCGTGGCCTAGAC | CRISPR 3' guide |
| *Got2* | GAATTC ATGAGTAGAACCATTATTATGACGCTTAAGGAC | Primer for cDNA clone |
| *Got2* | CTCGAG CTTGGTAACCTTGTGTATGCTCTCAGCCAGG | Primer for cDNA clone |

**Table 3-Oligos for human genes**

| Name of gene | Sequence | Additional Information |
|---|---|---|
| PC | GAATTC ATGCTGAAGTTCCGAACAGTCCATGGG | Forward Primer for cDNA clone |
| PC | GGATCC CTCGATCTCCAGGATGAGGTCGTCACC | Reverse Primer for cDNA clone |
| SLC1A3 | GGATCC ATGACTAAAAGCAATGGAGAAGAGC | Forward Primer for cDNA clone |
| SLC1A3 | CTACATCTTGGTTTCAATGTCGATGG | Reverse Primer for cDNA clone |
| GOT2 | GGATCC ATGGCCCTGCTGCACTCCGG | Forward Primer for cDNA clone |
| GOT2 | TCTAGA CTTGGTGACCTGGTGAATGGCATGG | Reverse Primer for cDNA clone |
| PC | GAAGCCTATCTCATCGGCCG *CGG* | CRISPR guide targeting exon 5 |
| PC | CGAAGTCCGCTCGCTCAGAG *AGG* | CRISPR guide targeting exon 6 |

| | | |
|---|---|---|
| PEPCK2 | ATCTCCACTAAGCACTCGCA *GGG* | CRISPR guide targeting exon 2 |
| PEPCK2 | CATGCGTATTATGACCCGAC *TGG* | CRISPR guide targeting exon 3 |
| GOT2 | GAGTGGCCGGGTAAGCTGAGCAG *AGG* | CRISPR guide a |
| GOT2 | GGAGTGGACCCGCTCCGGAACAG *TGG* | CRISPR guide b |

## Fly genotypes

**Figure 1**

| # | acronym | Detailed genotype |
|---|---|---|
| b-d | *w*$^{1118}$ | *w*$^{1118}$ |
| f | Control | *hs-Flp 1.22; +/+; act>CD2>Gal4, UAS-GFP/+* |
| | MPC+ | *hs-Flp 1.22; UAS-MPC1-P2A-MPC2/+; act>CD2>Gal4, UAS-GFP/+* |
| g | Control | *hs-Flp 1.22; +/+; act>CD2>Gal4, UAS-GFP/+* |
| | MPC+ | *hs-Flp 1.22; UAS-MPC1-P2A-MPC2/+; act>CD2>Gal4, UAS-GFP/+* |
| | *Mpc1*-KD | *hs-Flp 1.22; UAS-Mpc1*$^{RNAi}$*/+; act>CD2>Gal4, UAS-GFP/+* |
| h | Control | *hs-Flp 1.22; +/+; act>CD2>Gal4, UAS-GFP/+* |
| | MPC+ | *hs-Flp 1.22; UAS-MPC1-P2A-MPC2/+; act>CD2>Gal4, UAS-GFP/+* |
| l | Control | *hs-Flp 1.22; +/+; act>CD2>Gal4, UAS-GFP/+* |
| | MPC+ | *hs-Flp 1.22; UAS-MPC1-P2A-MPC2/+; act>CD2>Gal4, UAS-GFP/+* |
| | *Mpc1*-KD | *hs-Flp 1.22; UAS-Mpc1*$^{RNAi}$*/+; act>CD2>Gal4, UAS-GFP/+* |
| j | Control | *hs-Flp 1.22; +/+; act>CD2>Gal4, UAS-GFP/+* |
| | MPC+ | *hs-Flp 1.22; UAS-MPC1-P2A-MPC2/+; act>CD2>Gal4, UAS-GFP/+* |
| k | Control | *y, w; CG-Gal4/UAS-GFP; tubGal*$^{80ts20}$*/+* |
| | MPC+ | *y, w; CG-Gal4/ UAS-MPC1-P2A-MPC2; tubGal*$^{80ts20}$*/+* |
| l&m | Control | *hs-Flp 1.22; +/+; act>CD2>Gal4, UAS-GFP/+* |
| | MPC+ | *hs-Flp 1.22; UAS-MPC1-P2A-MPC2/+; act>CD2>Gal4, UAS-GFP/+* |

**Supplementary Figure 1**

| # | acronym | Detailed genotype |
|---|---|---|
| a-c | *w*$^{1118}$ | *w*$^{1118}$ |

**Supplementary Figure 2**

| # | acronym | Detailed genotype |
|---|---|---|
| b&c. | Control | *y, w; CG-Gal4/UAS-GFP; tubGal*$^{80ts20}$*/+* |
| | MPC+ | *y, w; CG-Gal4/ UAS-MPC1-P2A-MPC2; tubGal*$^{80ts20}$*/+* |
| e&f | MPC+ | *hs-Flp 1.22; UAS-MPC1-P2A-MPC2/+; act>CD2>Gal4, UAS-GFP/+* |
| g | Control | *hs-Flp 1.22; +/+; act>CD2>Gal4, UAS-GFP/+* |
| | MPC+ | *hs-Flp 1.22; UAS-MPC1-P2A-MPC2/+; act>CD2>Gal4, UAS-GFP/+* |
| h-k | Control | *y, w; CG-Gal4/UAS-GFP; tubGal*$^{80ts20}$*/+* |
| | MPC+ | *y, w; CG-Gal4/ UAS-MPC1-P2A-MPC2; tubGal*$^{80ts20}$*/+* |
| l-n | Control | *hs-Flp 1.22; +/+; act>CD2>Gal4, UAS-GFP/+* |
| | MPC+ | *hs-Flp 1.22; UAS-MPC1-P2A-MPC2/+; act>CD2>Gal4, UAS-GFP/+* |
| o&p | Control | *hs-Flp 1.22; +/+; act>CD2>Gal4, UAS-GFP/+* |
| | MPC+ | *hs-Flp 1.22; UAS-MPC1-P2A-MPC2/+; act>CD2>Gal4, UAS-GFP/+* |

1703 **Figure 2**

| # | acronym | Detailed genotype |
|---|---|---|
| b&c | S6K+ | *hs-Flp 1.22; UAS-S6K$^{STDETE}$/+; act>CD2>Gal4, UAS-GFP/+* |
| | Control | *hs-Flp 1.22; +/+; act>CD2>Gal4, UAS-GFP/+* |
| | MPC+ | *hs-Flp 1.22; UAS-MPC1-P2A-MPC2/+; act>CD2>Gal4, UAS-GFP/+* |
| d&e | Rheb+ | *hs-Flp 1.22; +/+; act>CD2>Gal4, UAS-GFP/ UAS-Rheb$^{PA}$* |
| | Control | *hs-Flp 1.22; +/+; act>CD2>Gal4, UAS-GFP/+* |
| | MPC+ | *hs-Flp 1.22; UAS-MPC1-P2A-MPC2/+; act>CD2>Gal4, UAS-GFP/+* |
| f&g | *Myc*-KD | *hs-Flp 1.22; +/+; act>CD2>Gal4, UAS-GFP/ UAS-Myc$^{RNAi}$* |
| | Control | *hs-Flp 1.22; +/+; act>CD2>Gal4, UAS-GFP/+* |
| | MPC+ | *hs-Flp 1.22; UAS-MPC1-P2A-MPC2/+; act>CD2>Gal4, UAS-GFP/+* |
| h&i | Control | *hs-Flp 1.22; +/+; act>CD2>Gal4, UAS-GFP/+* |
| | MPC+ | *hs-Flp 1.22; UAS-MPC1-P2A-MPC2/+; act>CD2>Gal4, UAS-GFP/+* |

1704

1705 **Supplementary Figure 3**

| # | acronym | Detailed genotype |
|---|---|---|
| a | Control | *y, w; CG-Gal4/UAS-GFP; tubGal$^{80ts20}$/+* |
| | MPC+ | *y, w; CG-Gal4/ UAS-MPC1-P2A-MPC2; tubGal$^{80ts20}$/+* |
| b | PI3K-DN | *hs-Flp 1.22; +/+; act>CD2>Gal4, UAS-GFP/ UAS-Pi3K92E.A2860C* |
| | Control | *hs-Flp 1.22; +/+; act>CD2>Gal4, UAS-GFP/+* |
| | MPC+ | *hs-Flp 1.22; UAS-MPC1-P2A-MPC2/+; act>CD2>Gal4, UAS-GFP/+* |
| c | Control | *hs-Flp 1.22; +/+; act>CD2>Gal4, UAS-GFP/+* |
| | MPC+ | *hs-Flp 1.22; UAS-MPC1-P2A-MPC2/+; act>CD2>Gal4, UAS-GFP/+* |
| | *PI3K*+ | *hs-Flp 1.22; +/+; act>CD2>Gal4, UAS-GFP/ UAS-PI3K93E$^{.Excel}$* |
| | MPC+, *PI3K*+ | *hs-Flp 1.22; UAS-MPC1-P2A-MPC2/+; act>CD2>Gal4, UAS-GFP/ UAS-PI3K93E$^{.Excel}$* |
| d | Control | *hs-Flp 1.22; +/+; act>CD2>Gal4, UAS-GFP/+* |
| | MPC+ | *hs-Flp 1.22; UAS-MPC1-P2A-MPC2/+; act>CD2>Gal4, UAS-GFP/+* |
| | *Tsc1*-KD | *hs-Flp 1.22; +/+; act>CD2>Gal4, UAS-GFP/ UAS-Tsc1$^{RNAi}$* |
| | MPC+, *Tsc1*-KD | *hs-Flp 1.22; UAS-MPC1-P2A-MPC2/+; act>CD2>Gal4, UAS-GFP/ UAS-Tsc1$^{RNAi}$* |
| e | Control | *hs-Flp 1.22; +/+; act>CD2>Gal4, UAS-GFP/+* |
| | MPC+ | *hs-Flp 1.22; UAS-MPC1-P2A-MPC2/+; act>CD2>Gal4, UAS-GFP/+* |
| | *Myc*+ | *hs-Flp 1.22; +/+; act>CD2>Gal4, UAS-GFP/ UAS-Myc* |
| | MPC+, *Myc*+ | *hs-Flp 1.22; UAS-MPC1-P2A-MPC2/+; act>CD2>Gal4, UAS-GFP/ UAS-Myc* |
| f | Control | *hs-Flp 1.22; +/+; act>CD2>Gal4, UAS-GFP/+* |
| | MPC+ | *hs-Flp 1.22; UAS-MPC1-P2A-MPC2/+; act>CD2>Gal4, UAS-GFP/+* |
| | *Myc*-KD | *hs-Flp 1.22; +/+; act>CD2>Gal4, UAS-GFP/ UAS-Myc$^{RNAi}$* |
| | MPC+, *Myc*-KD | *hs-Flp 1.22; UAS-MPC1-P2A-MPC2/+; act>CD2>Gal4, UAS-GFP/ UAS-Myc$^{RNAi}$* |

1706

1707 **Figure 4**

| # | acronym | Detailed genotype |
|---|---|---|
| e | MPC+ | *hs-Flp 1.22; UAS-MPC1-P2A-MPC2/+; act>CD2>Gal4, UAS-GFP/+* |
| | MPC+, *Pcb*-KD | *hs-Flp 1.22; UAS-MPC1-P2A-MPC2/+; act>CD2>Gal4, UAS-GFP/ UAS- -Pcb$^{RNAi}$* |

| | | |
|---|---|---|
| | *Pcb*+ | *hs-Flp 1.22; +/+; act>CD2>Gal4, UAS-GFP/ UAS-hPC* |
| f | Control | *hs-Flp 1.22; +/+; act>CD2>Gal4, UAS-GFP/+* |
| | MPC+ | *hs-Flp 1.22; UAS-MPC1-P2A-MPC2/+; act>CD2>Gal4, UAS-GFP/+* |
| | *Pcb*+ | *hs-Flp 1.22; +/+; act>CD2>Gal4, UAS-GFP/ UAS-hPC* |
| | MPC+, *Pcb*+ | *hs-Flp 1.22; UAS-MPC1-P2A-MPC2/+; act>CD2>Gal4, UAS-GFP/ UAS-hPC* |
| | *Pcb*-KD | *hs-Flp 1.22; +/+; act>CD2>Gal4, UAS-GFP/ UAS-Pcb$^{RNAi}$* |
| | MPC+, *Pcb*-KD | *hs-Flp 1.22; UAS-MPC1-P2A-MPC2/+; act>CD2>Gal4, UAS-GFP/ UAS--Pcb$^{RNAi}$* |
| g&h | Control | *y, w; CG-Gal4/UAS-GFP; tubGal$^{80ts20}$/+* |
| | MPC+ | *y, w; CG-Gal4/ UAS-MPC1-P2A-MPC2; tubGal$^{80ts20}$/+* |
| n | MPC+ | *hs-Flp 1.22; UAS-MPC1-P2A-MPC2/+; act>CD2>Gal4, UAS-GFP/+* |
| | MPC+, *Pepck2*-KD | *hs-Flp 1.22; UAS-MPC1-P2A-MPC2/+; act>CD2>Gal4, UAS-GFP/UAS-Pepck2$^{RNAi}$* |
| o | Control | *hs-Flp 1.22; +/+; act>CD2>Gal4, UAS-GFP/+* |
| | MPC+ | *hs-Flp 1.22; UAS-MPC1-P2A-MPC2/+; act>CD2>Gal4, UAS-GFP/+* |
| | *Pepck2*-KD | *hs-Flp 1.22; +/+; act>CD2>Gal4, UAS-GFP/UAS-Pepck2$^{RNAi}$* |
| | MPC+, *Pepck2*-KD | *hs-Flp 1.22; UAS-MPC1-P2A-MPC2/+; act>CD2>Gal4, UAS-GFP/UAS-Pepck2$^{RNAi}$* |
| | *Fbp*-KD | *hs-Flp 1.22; +/+; act>CD2>Gal4, UAS-GFP/UAS-Fbp$^{RNAi}$* |
| | MPC+, *Fbp*-KD | *hs-Flp 1.22; UAS-MPC1-P2A-MPC2/+; act>CD2>Gal4, UAS-GFP/UAS-Fbp2$^{RNAi}$* |
| p | MPC+ | *hs-Flp 1.22; UAS-MPC1-P2A-MPC2/+; act>CD2>Gal4, UAS-GFP/+* |
| | MPC+, *Pcb*-KD | *hs-Flp 1.22; UAS-MPC1-P2A-MPC2/+; act>CD2>Gal4, UAS-GFP/ UAS-Pcb$^{RNAi}$* |
| | MPC+, *Pepck2*-KD | *hs-Flp 1.22; UAS-MPC1-P2A-MPC2/+; act>CD2>Gal4, UAS-GFP/UAS-Pepck2$^{RNAi}$* |
| q | Control | *hs-Flp 1.22; +/+; act>CD2>Gal4, UAS-GFP/+* |
| | MPC+ | *hs-Flp 1.22; UAS-MPC1-P2A-MPC2/+; act>CD2>Gal4, UAS-GFP/+* |
| | *Pcb*-KD | *hs-Flp 1.22; +/+; act>CD2>Gal4, UAS-GFP/ UAS-Pcb$^{RNAi}$* |
| | MPC+, *Pcb*-KD | *hs-Flp 1.22; UAS-MPC1-P2A-MPC2/+; act>CD2>Gal4, UAS-GFP/ UAS-Pcb$^{RNAi}$* |
| | *Pepck2*-KD | *hs-Flp 1.22; +/+; act>CD2>Gal4, UAS-GFP/UAS-Pepck2$^{RNAi}$* |
| | MPC+, *Pepck2*-KD | *hs-Flp 1.22; UAS-MPC1-P2A-MPC2/+; act>CD2>Gal4, UAS-GFP/UAS-Pepck2$^{RNAi}$* |

**Supplementary Figure 6**

| # | acronym | Detailed genotype |
|---|---|---|
| a | Control | *hs-Flp 1.22; +/+; act>CD2>Gal4, UAS-GFP/+* |
| | MPC+ | *hs-Flp 1.22; UAS-MPC1-P2A-MPC2/+; act>CD2>Gal4, UAS-GFP/+* |
| | *Pcb*-KO | *hs-Flp 1.22; Pcb-KO/+; act>CD2>Gal4, UAS-GFP/+* |

| | | |
|---|---|---|
| | MPC+, *Pcb*-KO | *hs-Flp 1.22; UAS-MPC1-P2A-MPC2/ Pcb-KO; act>CD2>Gal4, UAS-GFP/+* |
| c | MPC+ | *hs-Flp 1.22; UAS-MPC1-P2A-MPC2/+; act>CD2>Gal4, UAS-GFP/+* |
| | *Pdha*-KD | *hs-Flp 1.22; UAS-Pdha$^{RNAi}$ /+; act>CD2>Gal4, UAS-GFP/ UAS-hPC* |
| | MPC+, *Pdk*-KD | *hs-Flp 1.22; UAS-MPC1-P2A-MPC2/+; act>CD2>Gal4, UAS-GFP/ UAS-Pdk$^{RNAi}$* |
| d | Control | *hs-Flp 1.22; +/+; act>CD2>Gal4, UAS-GFP/+* |
| | MPC+ | *hs-Flp 1.22; UAS-MPC1-P2A-MPC2/+; act>CD2>Gal4, UAS-GFP/+* |
| | *Pdha*-KD | *hs-Flp 1.22; UAS-Pdha$^{RNAi}$ /+; act>CD2>Gal4, UAS-GFP/ UAS-hPC* |
| | MPC+, *Pdha*-KD | *hs-Flp 1.22; UAS-MPC1-P2A-MPC2/ UAS-Pdha$^{RNAi}$; act>CD2>Gal4, UAS-GFP/+* |
| | *Dlat*-KD | *hs-Flp 1.22; UAS-Dlat$^{RNAi}$ /+; act>CD2>Gal4, UAS-GFP/ UAS-hPC* |
| | MPC+, *Dlat*-KD | *hs-Flp 1.22; UAS-MPC1-P2A-MPC2/ UAS-Dlat$^{RNAi}$; act>CD2>Gal4, UAS-GFP/+* |
| | *Pdk*-KD | *hs-Flp 1.22; +/+; act>CD2>Gal4, UAS-GFP/ UAS-Pdk$^{RNAi}$* |
| | MPC+, *Pdk*-KD | *hs-Flp 1.22; UAS-MPC1-P2A-MPC2/+; act>CD2>Gal4, UAS-GFP/ UAS-Pdk$^{RNAi}$* |

**Figure 5**

| # | acronym | Detailed genotype |
|---|---|---|
| a | Control | *y, w; CG-Gal4/UAS-GFP; tubGal$^{80ts20}$/+* |
| | MPC+ | *y, w; CG-Gal4/ UAS-MPC1-P2A-MPC2; tubGal$^{80ts20}$/+* |
| c | MPC+ | *hs-Flp 1.22; UAS-MPC1-P2A-MPC2/+; act>CD2>Gal4, UAS-GFP/+* |
| | MPC+, *Nmnat*+ | *hs-Flp 1.22; UAS-MPC1-P2A-MPC2/ UAS-Nmnat; act>CD2>Gal4, UAS-GFP/+* |
| d | Control | *hs-Flp 1.22; +/+; act>CD2>Gal4, UAS-GFP/+* |
| | MPC+ | *hs-Flp 1.22; UAS-MPC1-P2A-MPC2/+; act>CD2>Gal4, UAS-GFP/+* |
| | *Nmnat*+ | *hs-Flp 1.22; UAS-Nmnat/+; act>CD2>Gal4, UAS-GFP/+* |
| | MPC+, *Nmnat*+ | *hs-Flp 1.22; UAS-MPC1-P2A-MPC2/ UAS-Nmnat; act>CD2>Gal4, UAS-GFP/+* |
| e | MPC+ | *hs-Flp 1.22; UAS-MPC1-P2A-MPC2/+; act>CD2>Gal4, UAS-GFP/+* |
| | MPC+, NDI+ | *hs-Flp 1.22; UAS-MPC1-P2A-MPC2/+; act>CD2>Gal4, UAS-GFP/ UAS-NDI* |
| | MPC+, NDX+ | *hs-Flp 1.22; UAS-MPC1-P2A-MPC2/+; act>CD2>Gal4, UAS-GFP/ UAS-NDX* |
| f | Control | *hs-Flp 1.22; +/+; act>CD2>Gal4, UAS-GFP/+* |
| | MPC+ | *hs-Flp 1.22; UAS-MPC1-P2A-MPC2/+; act>CD2>Gal4, UAS-GFP/+* |
| | NDI+ | *hs-Flp 1.22; +/+; act>CD2>Gal4, UAS-GFP/ UAS-NDI* |
| | MPC+, NDI+ | *hs-Flp 1.22; UAS-MPC1-P2A-MPC2/+; act>CD2>Gal4, UAS-GFP/ UAS-NDI* |
| | NDX+ | *hs-Flp 1.22; +/+; act>CD2>Gal4, UAS-GFP/ UAS-NDX* |
| | MPC+, NDX+ | *hs-Flp 1.22; UAS-MPC1-P2A-MPC2/+; act>CD2>Gal4, UAS-GFP/ UAS-NDX* |
| i | MPC+ | *hs-Flp 1.22; UAS-MPC1-P2A-MPC2/+; act>CD2>Gal4, UAS-GFP/+* |
| | MPC+, NDX+ | *hs-Flp 1.22; UAS-MPC1-P2A-MPC2/+; act>CD2>Gal4, UAS-GFP/ UAS-NDX* |
| j | Control | *hs-Flp 1.22; +/+; act>CD2>Gal4, UAS-GFP/+* |

| | | |
|---|---|---|
| | MPC+ | *hs-Flp 1.22; UAS-MPC1-P2A-MPC2/+; act>CD2>Gal4, UAS-GFP/+* |
| | NDX+ | *hs-Flp 1.22; +/+; act>CD2>Gal4, UAS-GFP/ UAS-NDX* |
| | MPC+, NDX+ | *hs-Flp 1.22; UAS-MPC1-P2A-MPC2/+; act>CD2>Gal4, UAS-GFP/ UAS-NDX* |

**Figure 6**

| # | acronym | Detailed genotype |
|---|---|---|
| d | MPC+ | *hs-Flp 1.22; UAS-MPC1-P2A-MPC2/+; act>CD2>Gal4, UAS-GFP/+* |
| e | Control | *hs-Flp 1.22; +/+; act>CD2>Gal4, UAS-GFP/+* |
| | MPC+ | *hs-Flp 1.22; UAS-MPC1-P2A-MPC2/+; act>CD2>Gal4, UAS-GFP/+* |
| f | MPC+ | *hs-Flp 1.22; UAS-MPC1-P2A-MPC2/+; act>CD2>Gal4, UAS-GFP/+* |
| | MPC+, *slif*+ | *hs-Flp 1.22; UAS-MPC1-P2A-MPC2/+; act>CD2>Gal4, UAS-GFP/ UAS-slif* |
| g | Control | *hs-Flp 1.22; +/+; act>CD2>Gal4, UAS-GFP/+* |
| | MPC+ | *hs-Flp 1.22; UAS-MPC1-P2A-MPC2/+; act>CD2>Gal4, UAS-GFP/+* |
| | *slif*+ | *hs-Flp 1.22; +/+; act>CD2>Gal4, UAS-GFP/ UAS-slif* |
| | MPC+, *slif*+ | *hs-Flp 1.22; UAS-MPC1-P2A-MPC2/+; act>CD2>Gal4, UAS-GFP/ UAS-slif* |
| i | MPC+ | *hs-Flp 1.22; UAS-MPC1-P2A-MPC2/+; act>CD2>Gal4, UAS-GFP/+* |
| | *Got2*-KD | *hs-Flp 1.22; +/+; act>CD2>Gal4, UAS-GFP/ UAS-Got2$^{RNAi}$* |
| | MPC+, *Got2*+ | *hs-Flp 1.22; UAS-MPC1-P2A-MPC2/+; act>CD2>Gal4, UAS-GFP/UAS-Got2* |
| j | Control | *hs-Flp 1.22; +/+; act>CD2>Gal4, UAS-GFP/+* |
| | MPC+ | *hs-Flp 1.22; UAS-MPC1-P2A-MPC2/+; act>CD2>Gal4, UAS-GFP/+* |
| | *Got2*-KD | *hs-Flp 1.22; +/+; act>CD2>Gal4, UAS-GFP/ UAS-Got2$^{RNAi}$* |
| | MPC+, *Got2*-KD | *hs-Flp 1.22; UAS-MPC1-P2A-MPC2/+; act>CD2>Gal4, UAS-GFP/ UAS-Got2$^{RNAi}$* |
| | *Got2*+ | *hs-Flp 1.22; +/+; act>CD2>Gal4, UAS-GFP/UAS- Got2+* |
| | MPC+, *Got2*+ | *hs-Flp 1.22; UAS-MPC1-P2A-MPC2/+; act>CD2>Gal4, UAS-GFP/UAS-Got2+* |

## Author Information

**Ashish G. Toshniwal**
Department of Biochemistry, The University of Utah, Salt Lake City, United States
**Contribution**
Conceptualization, Data curation, Formal analysis, Validation, Investigation, Visualization, Methodology, Writing – original draft, Writing – review and editing
**0000-0001-8957-7970**
**ashish.toshniwal@biochem.utah.edu**

**Geanette Lam**
Department of Biochemistry, The University of Utah, Salt Lake City, United States
**Contribution**
Methodology

**Ahmad A Cluntun**
Department of Biochemistry, The University of Utah, Salt Lake City, United States
**Contribution**
Investigation, Methodology
0000-0001-7612-8375
Present address: Department of Biochemistry & Molecular Biology, Rutgers Robert Wood Johnson Medical School, Piscataway, NJ 08854
Ahmad.cluntun@rutgers.edu

**Alex J. Bott**
Department of Biochemistry, The University of Utah, Salt Lake City, United States
**Contribution**
Investigation, Methodology
**0000-0003-2273-8922**

**Hyuck-Jin Nam**
Department of Human Genetics, University of Utah, Salt Lake City, UT 84132, USA
**Contribution**
Methodology
**hjin@genetics.utah.edu**
**0000-0002-9489-6439**

**Rachel Skabelund**
Department of Biochemistry, The University of Utah, Salt Lake City, United States
**Contribution**
Methodology
**rachel.skabelund@biochem.utah.edu**
**0000-0001-6533-8887**

**Dona R. Wisidagama,**
Department of Human Genetics, University of Utah, Salt Lake City, UT 84132, USA
**Contribution**
Investigation
**roonalika@gmail.com**

**0009-0002-7029-3294**

**Carl S. Thummel**
Department of Human Genetics, University of Utah, Salt Lake City, UT 84132, USA
**Contribution**
Conceptualization, Resources, Supervision, Funding acquisition, Writing – review and editing
cthummel@genetics.utah.edu
0000-0001-8112-4643

**Jared Rutter**
1. Department of Biochemistry, The University of Utah, Salt Lake City, United States
2. Howard Hughes Medical Institute, University of Utah, Salt Lake City, United States

**Contribution**
Conceptualization, Resources, Supervision, Funding acquisition, Writing – original draft, Project administration, Writing – review and editing
**Lead contact**
**0000-0002-2710-9765**
**Rutter@biochem.utah.edu**

## Funding

**American Heart Association (24POST1201210)**
Ashish G Toshniwal
**National Institutes of Health (K00CA212445)**
Alex J. Bott
**National Institutes of Health (1K99HL168312-01)**
Ahmad A Cluntun
**National Institutes of Health (R01CA228346)**
Carl Thummel
**Howard Hughes Medical Institute and National Institutes of Health (R01CA228346)**
Jared Rutter
The funders had no role in study design, data collection and interpretation, or the decision to submit the work for publication.

## Acknowledgements

We thank the University of Utah core facilities, especially James Cox, PhD, at the Metabolomics core, Li Ying, PhD, at the Metabolic Phenotyping core, James Marvin, PhD, at the Flow Cytometry Core, Brian Dalley, PhD, at the High-Throughput Genomics Core, and the DNA/Peptide Synthesis Core. We thank members of the Rutter lab for discussion and feedback on the manuscript. Several of the figures were created with BioRender.com. This study was supported by 24POST1201210 to AGT; K00CA212445 to AJB; 1K99HL168312-01 To AAC, R01 CA228346 to CT and JR. JR is an Investigator of the Howard Hughes Medical Institute.

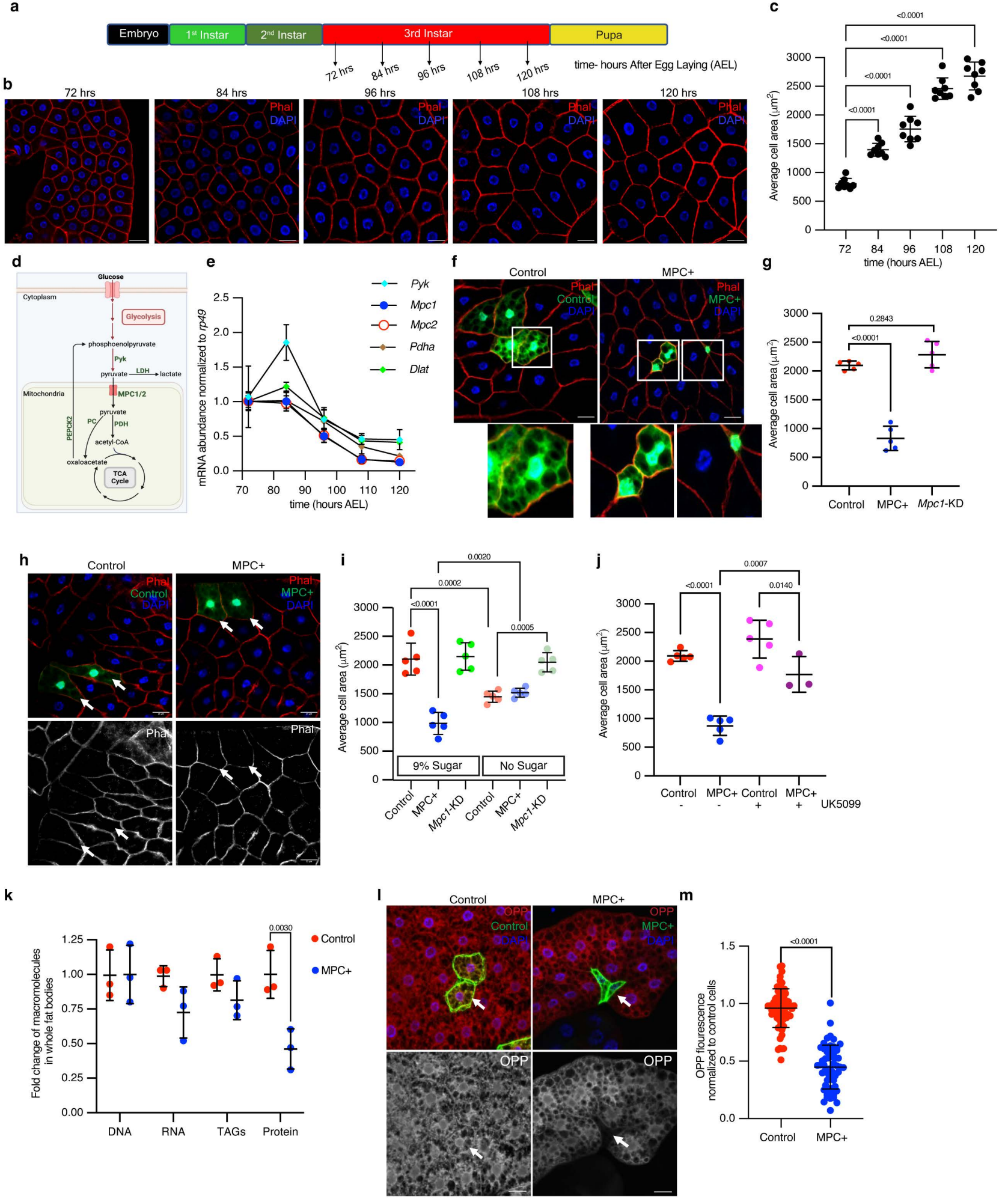


**Figure 1: Increased mitochondrial pyruvate transport reduces size of *Drosophila* fat body cells**

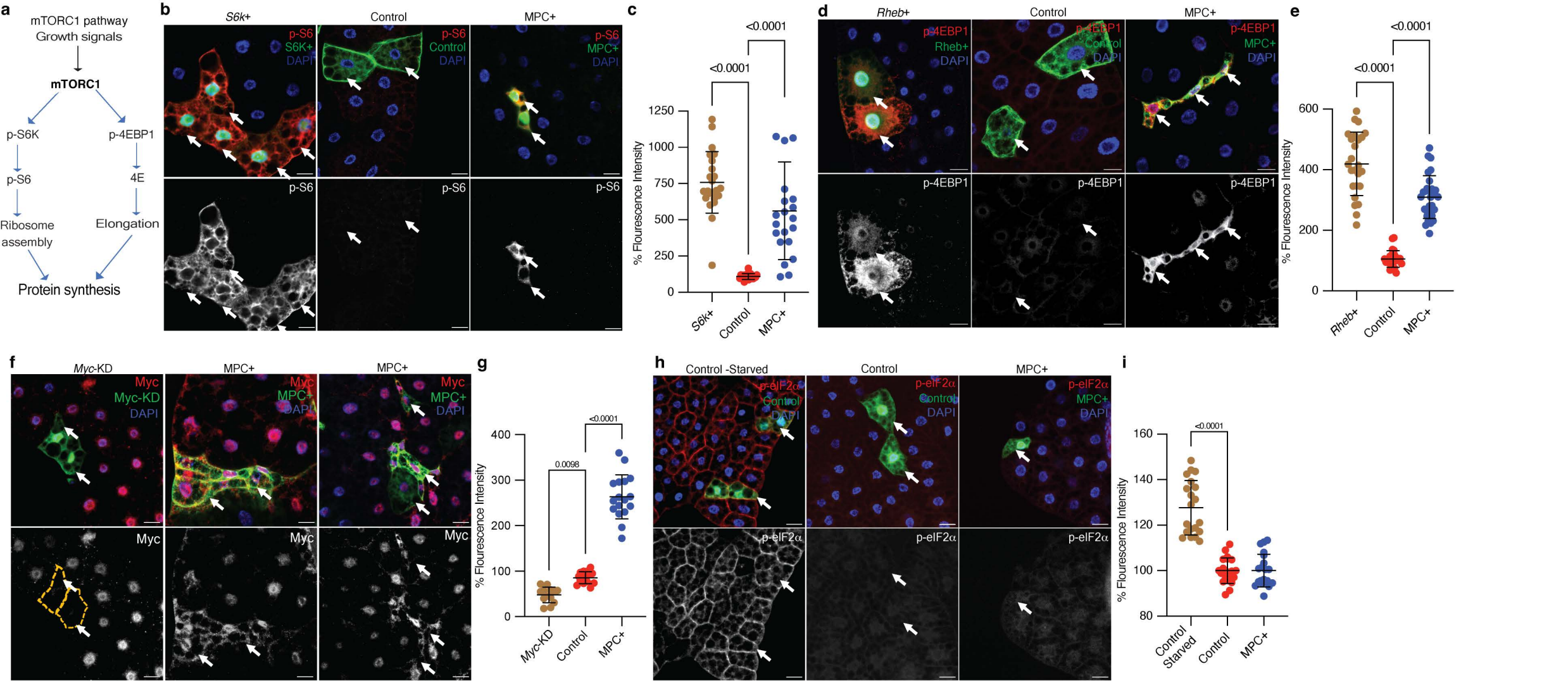


**Figure 2 – mTORC1 and Myc pathways are hyperactivated in MPC expressing fat body cells.**

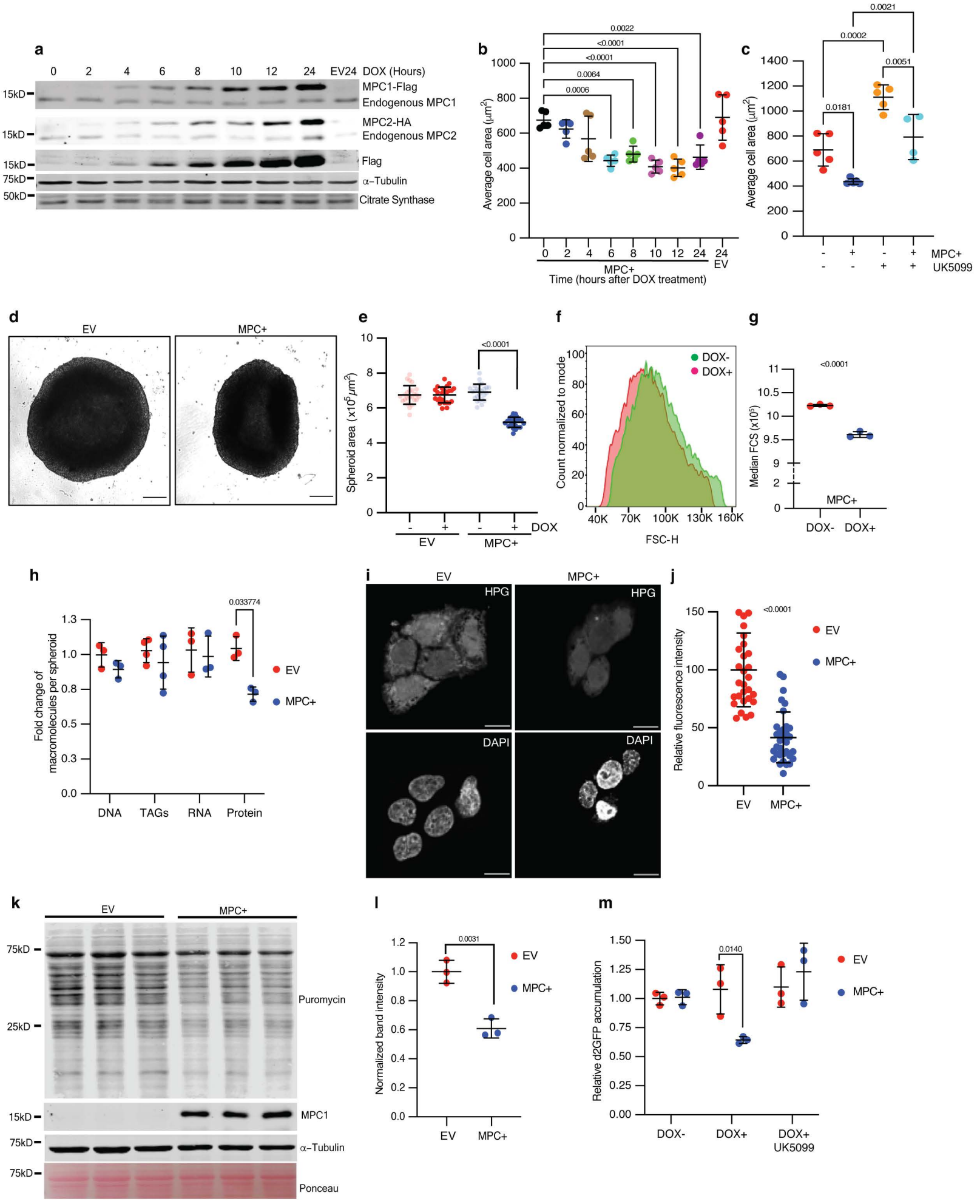


**Figure 3 – Increased mitochondrial pyruvate transport reduces size of HepG2 spheroids.**

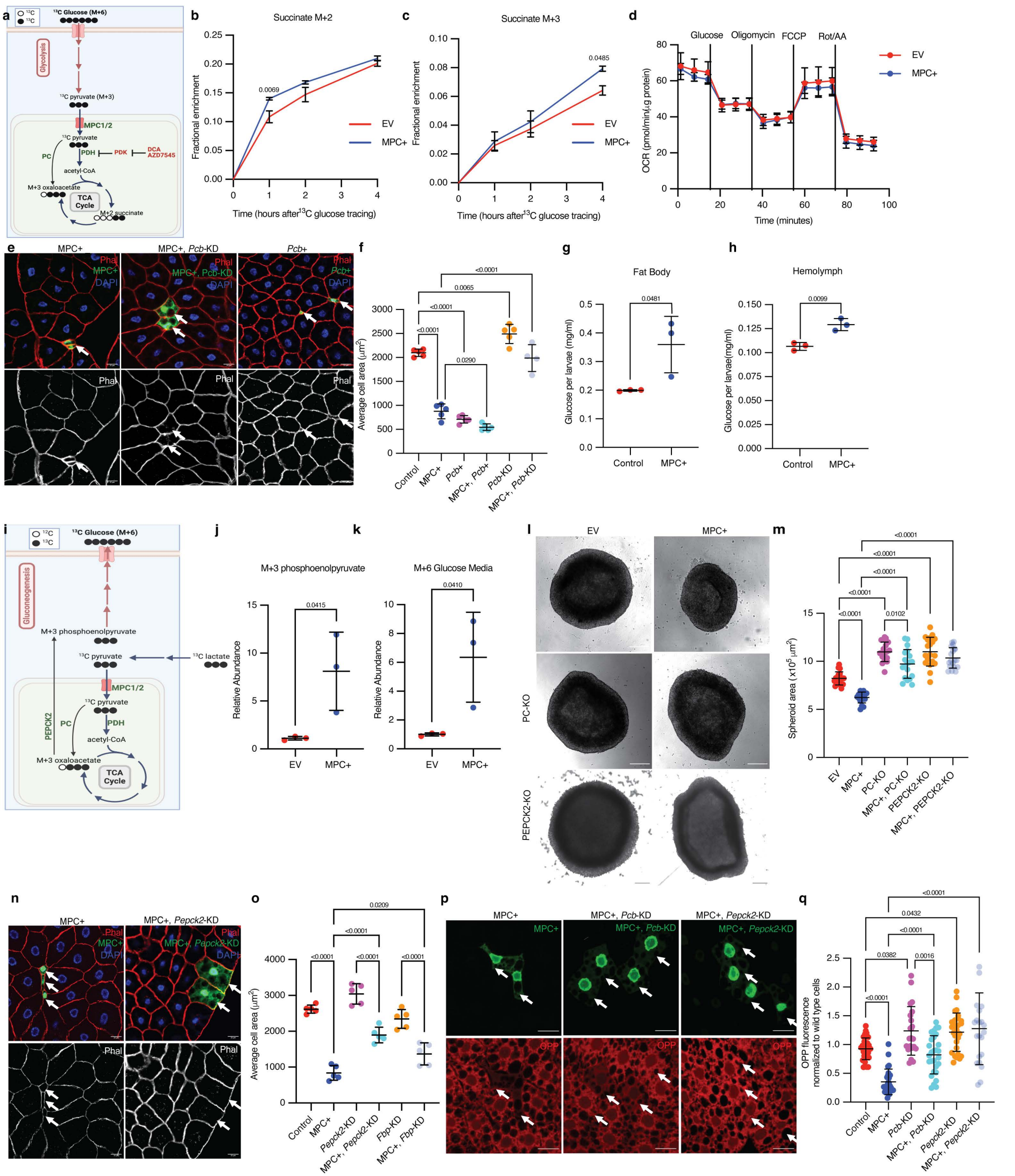


**Figure 4: Increased mitochondrial pyruvate metabolism promotes gluconeogenesis via pyruvate carboxylase to suppress protein synthesis**

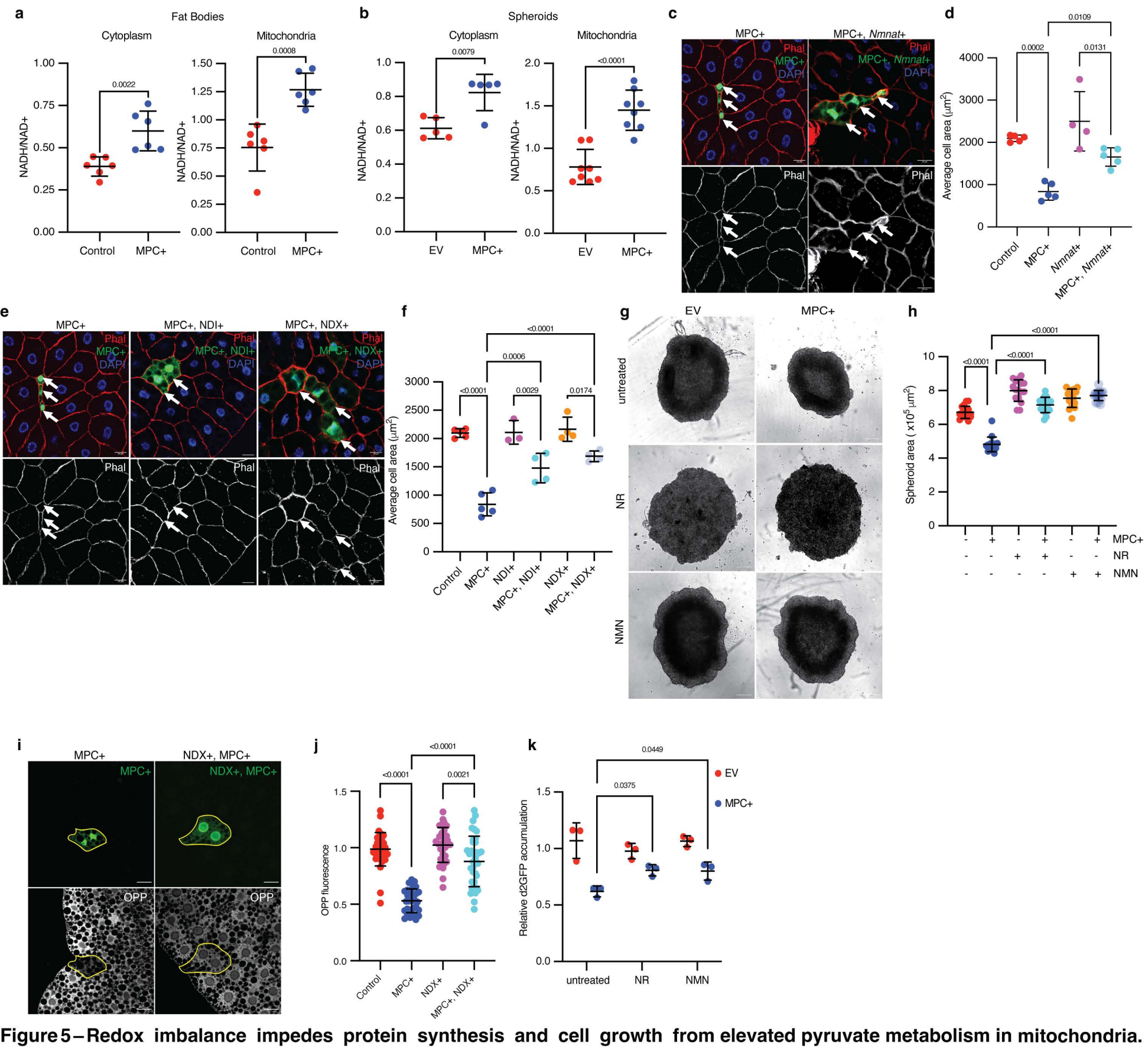


**Figure 5 – Redox imbalance impedes protein synthesis and cell growth from elevated pyruvate metabolism in mitochondria.**

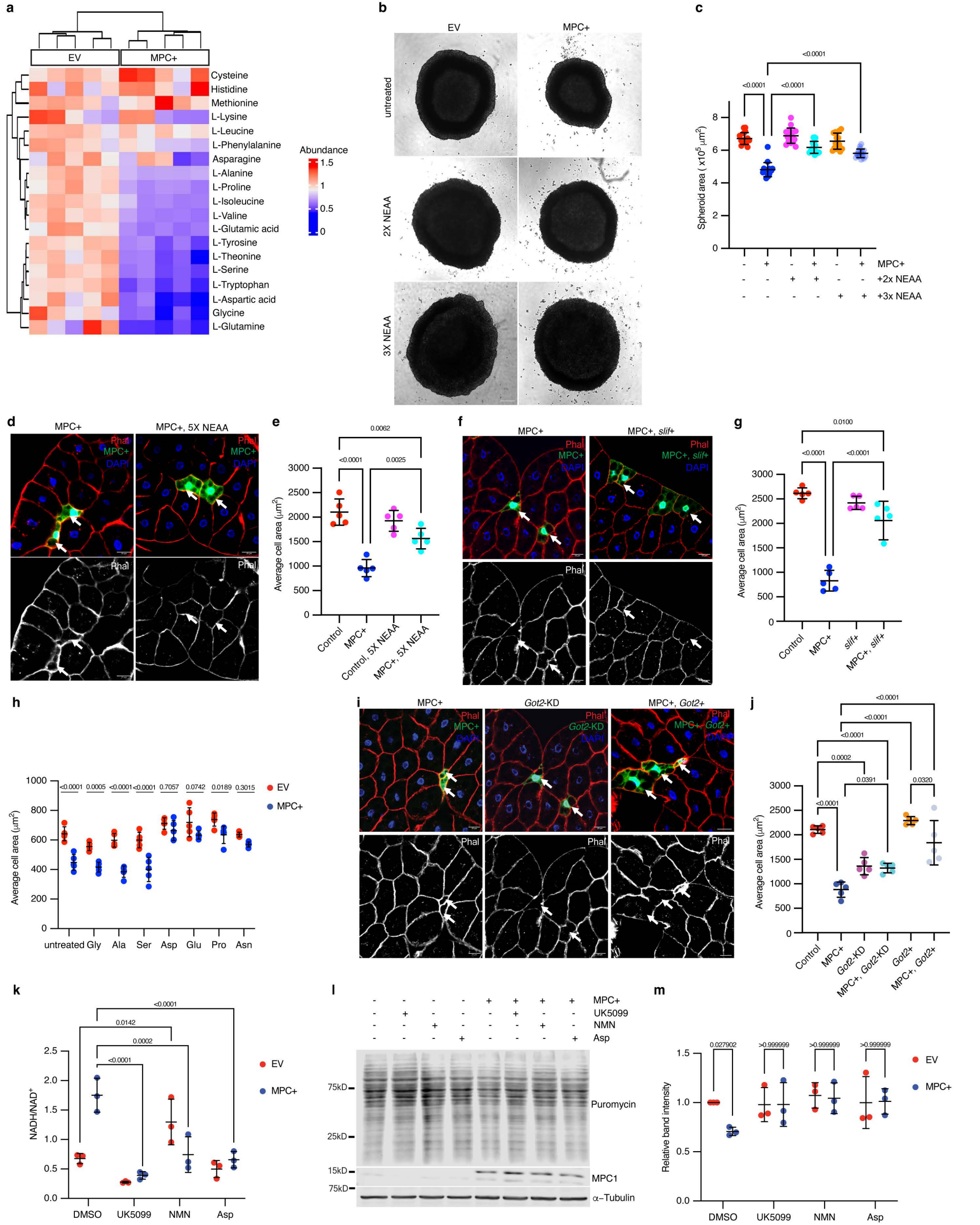


**Figure 6 – Reduced amino acid abundance impairs size of MPC-expressing cells**

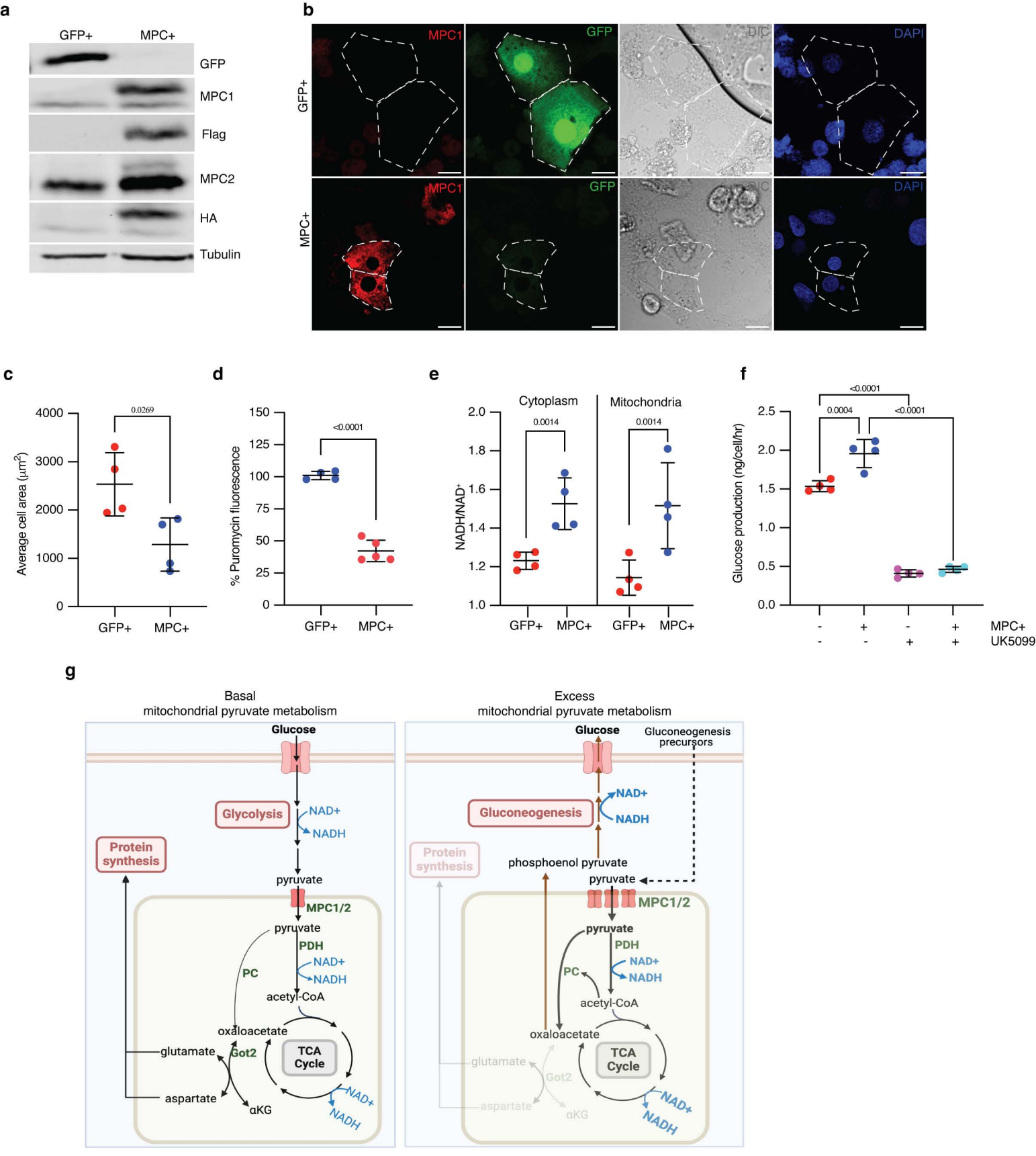


**Figure 7– Increased mitochondrial pyruvate transport rewires metabolism and redox status to reduce protein synthesis and cell size in rat primary hepatocytes**

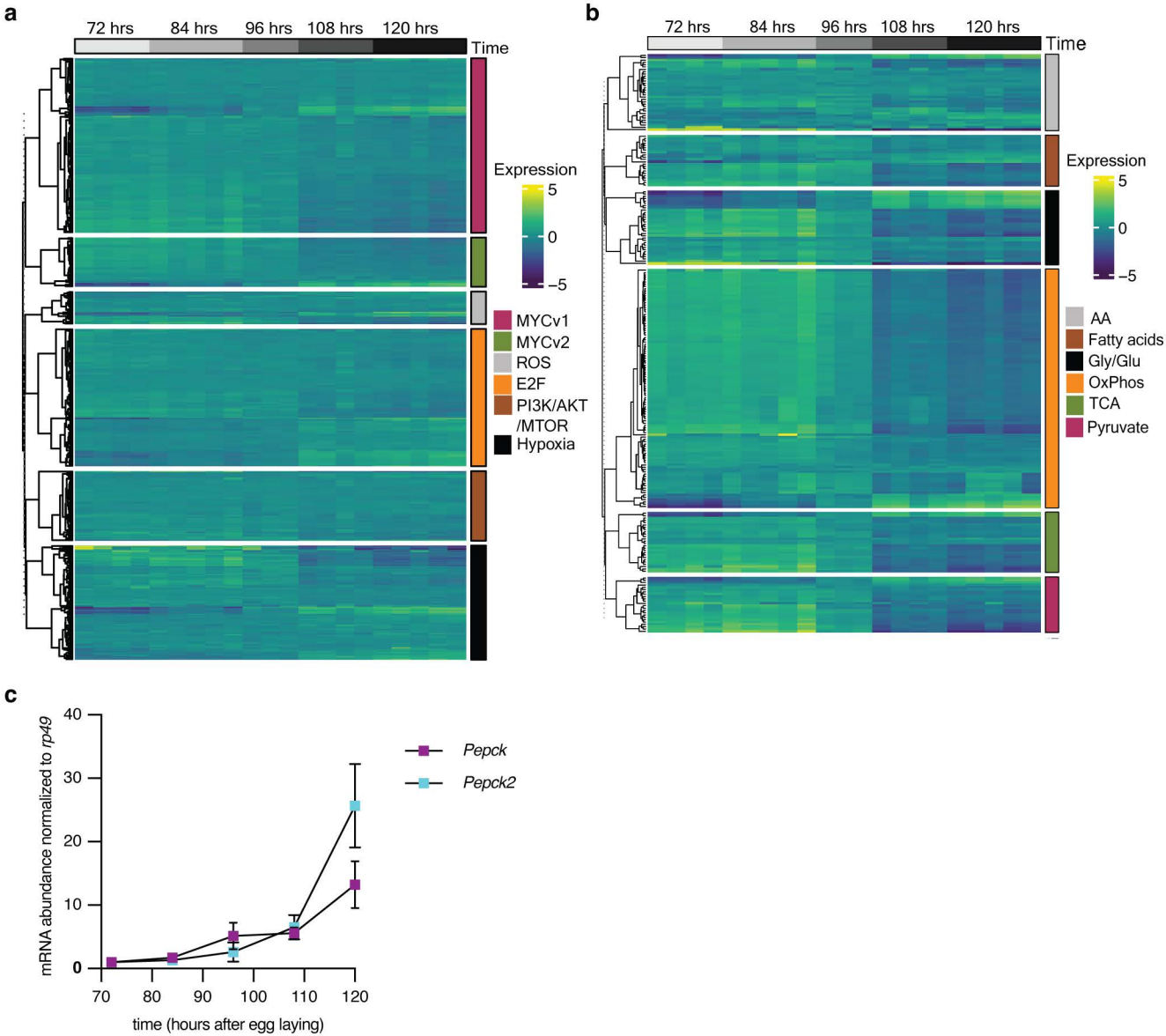


**Supplementary Figure 1 – Transcriptomic changes in fat body during larval development (related to Main Figure 1)**

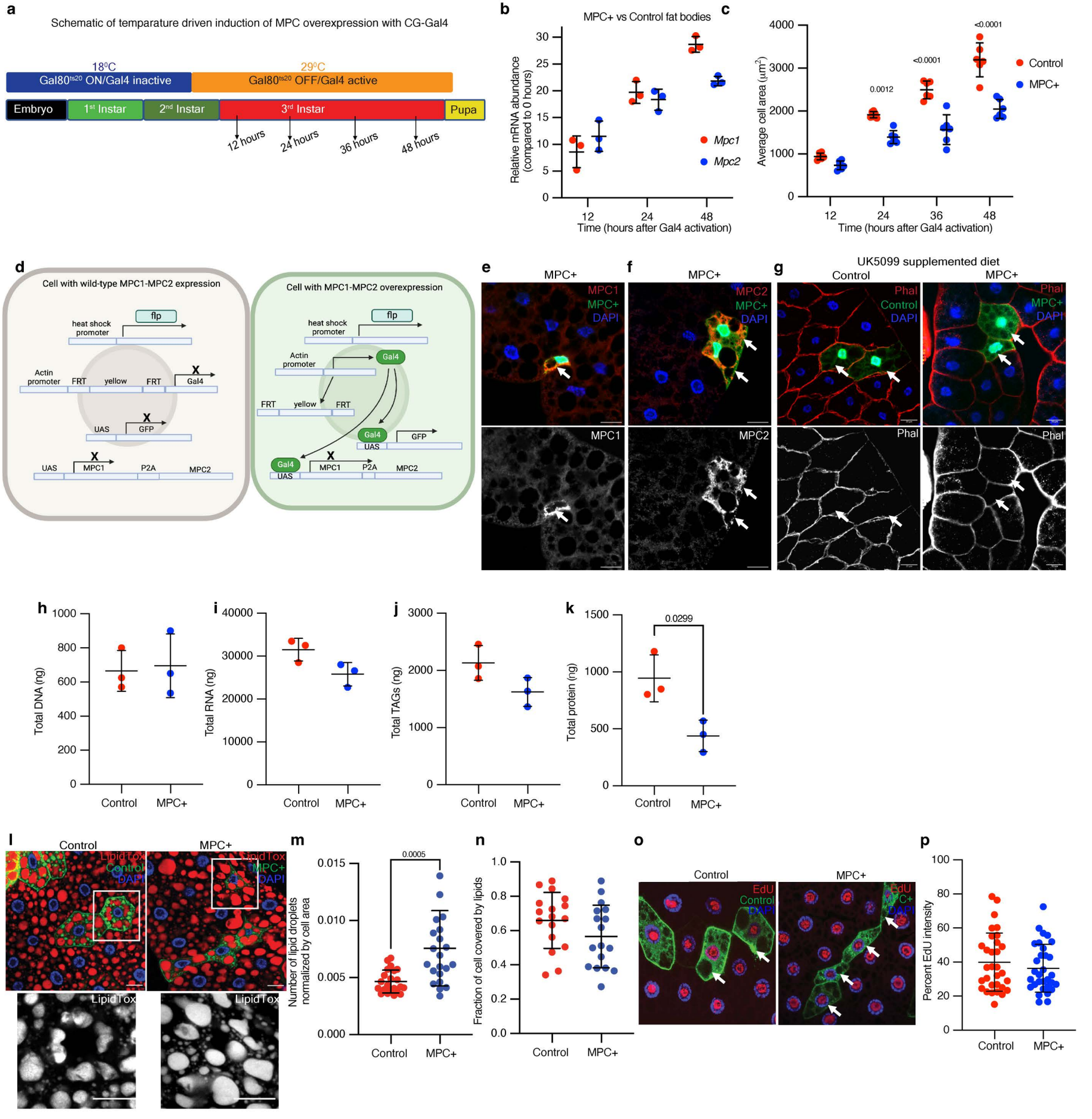


**Supplementary Figure 2 – MPC expression reduces size of *Drosophila* fat body cells. (related to Main Figure 1)**

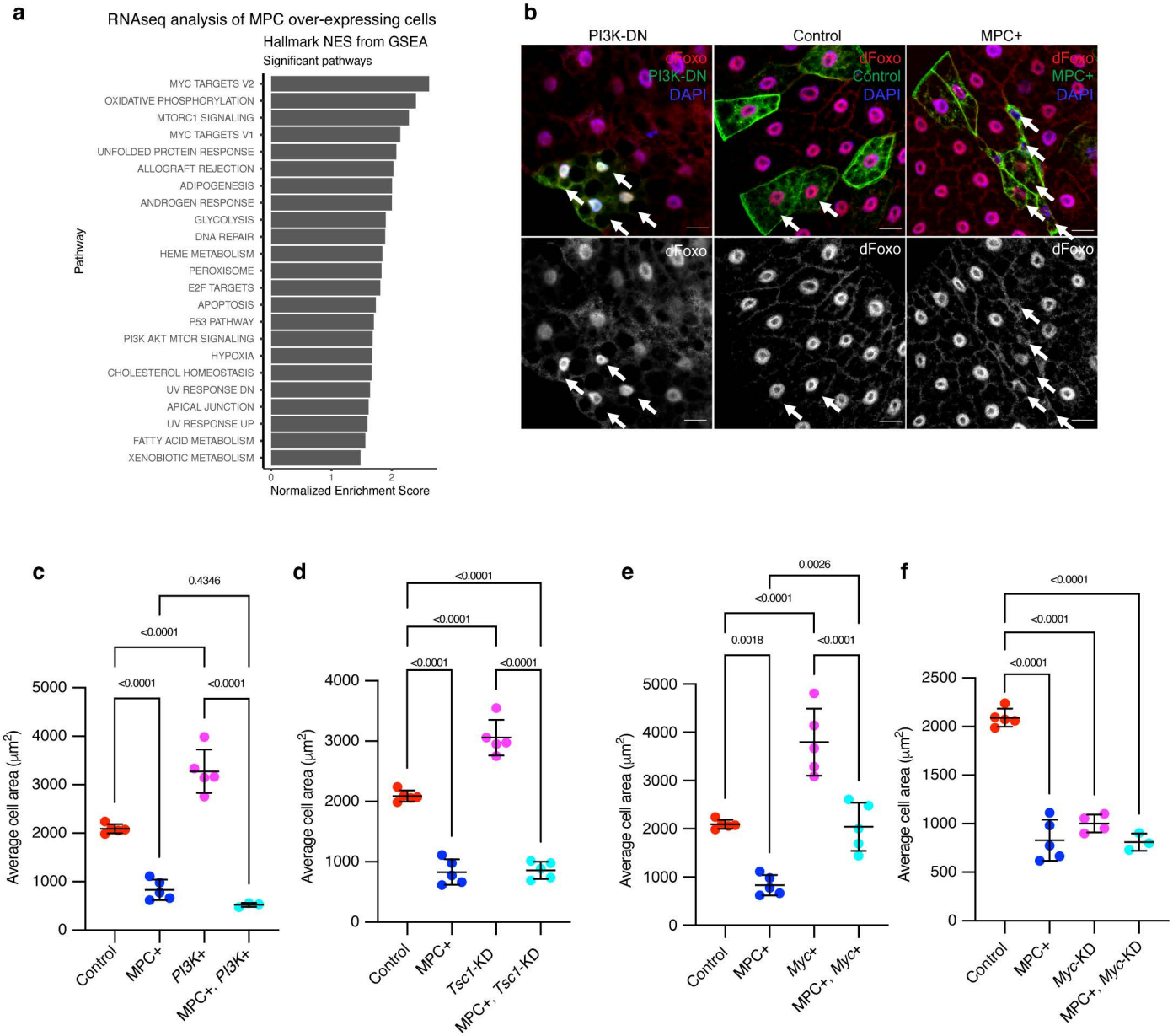


**Supplementary Figure 3 – mTORC1 and Myc pathways are hyperactivated in MPC expressing fat body cells. (related to Main Figure 2)**

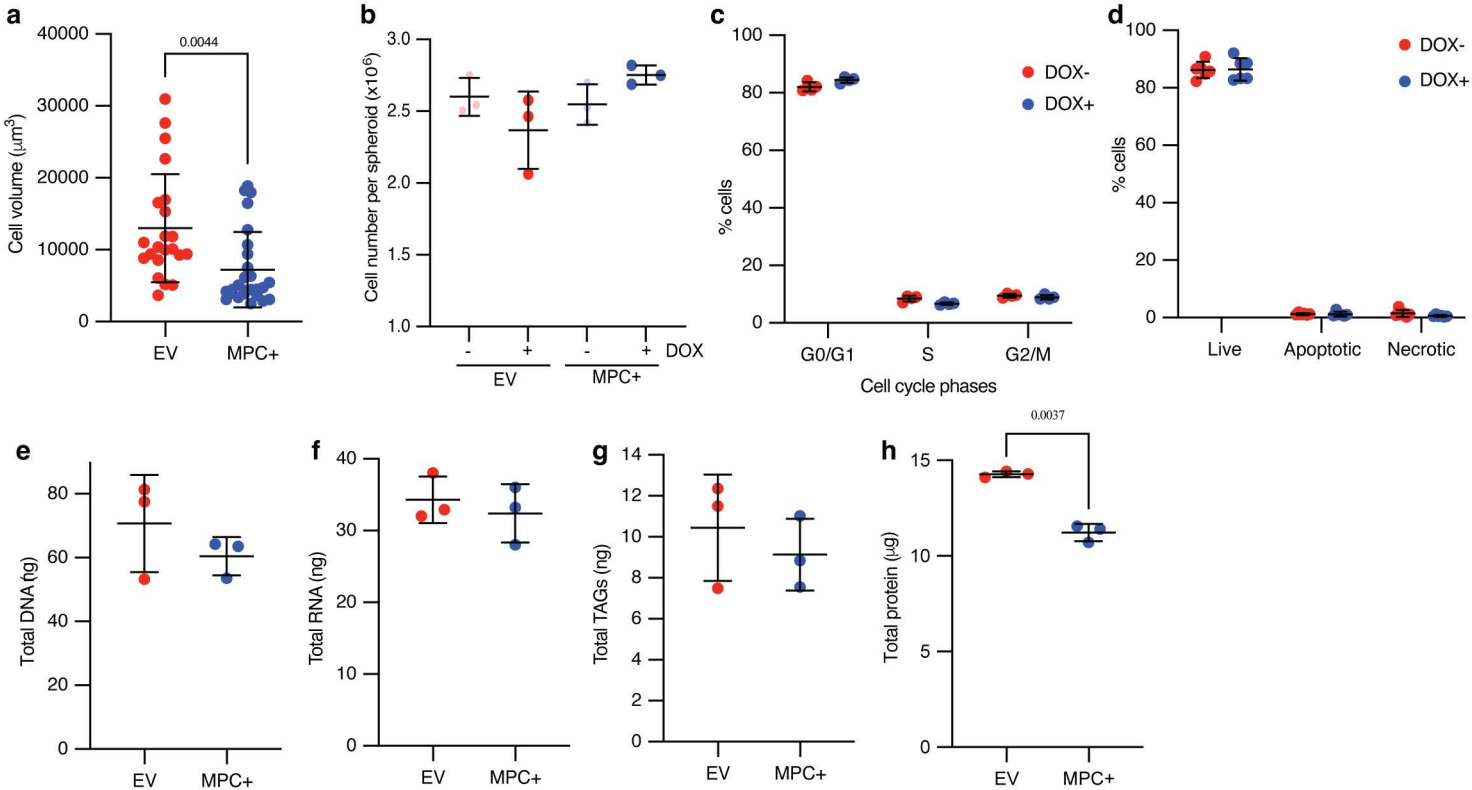


**Supplementary Figure 4 – MPC expression reduces size of HepG2 cells in 2D and spheroid culture (Related to Main Figure 3).**

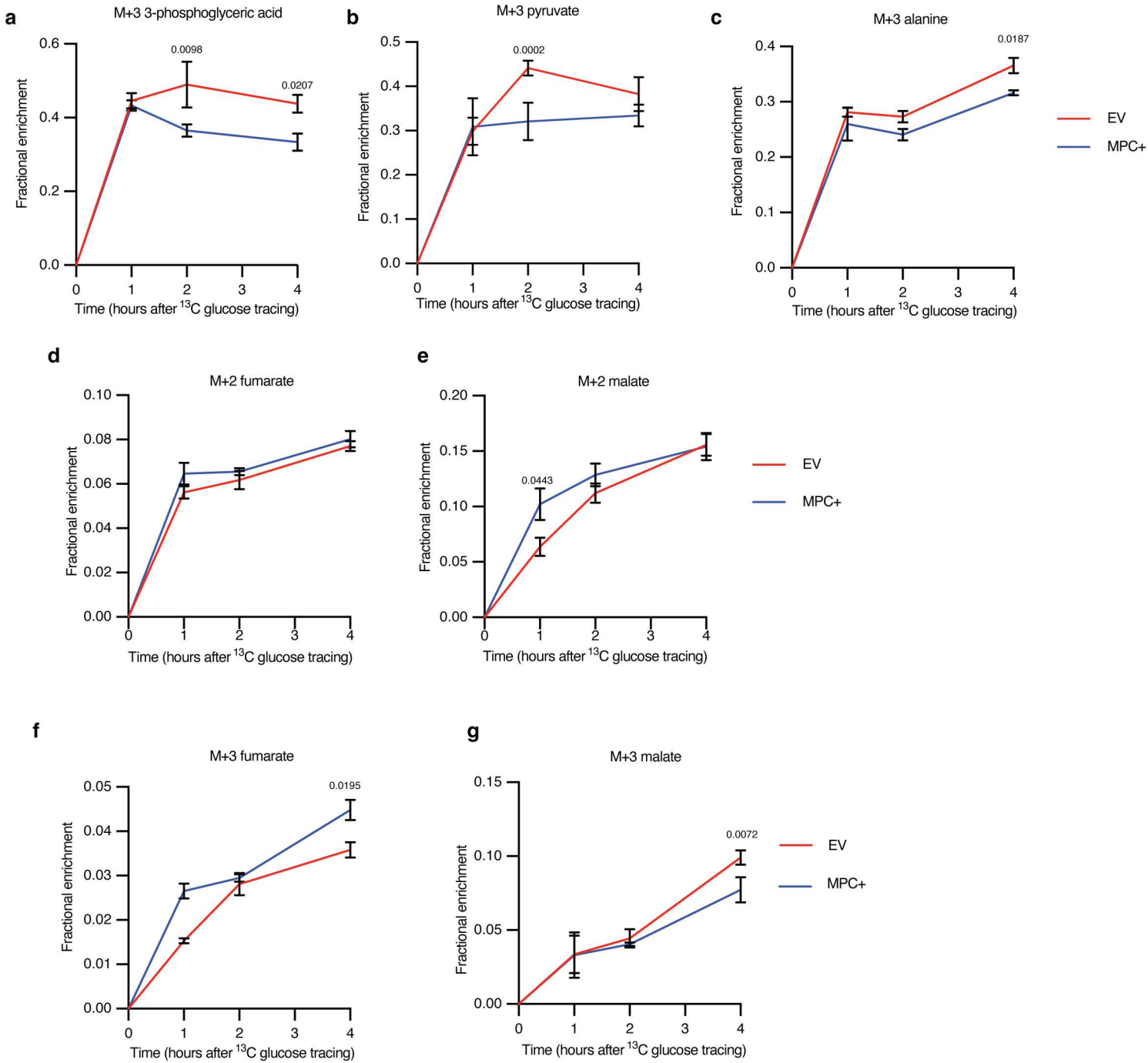


**Supplementary Figure 5: $^{13}$C glucose tarcing in MPC expressing HepG2 cells. (related to Main Figure 4)**

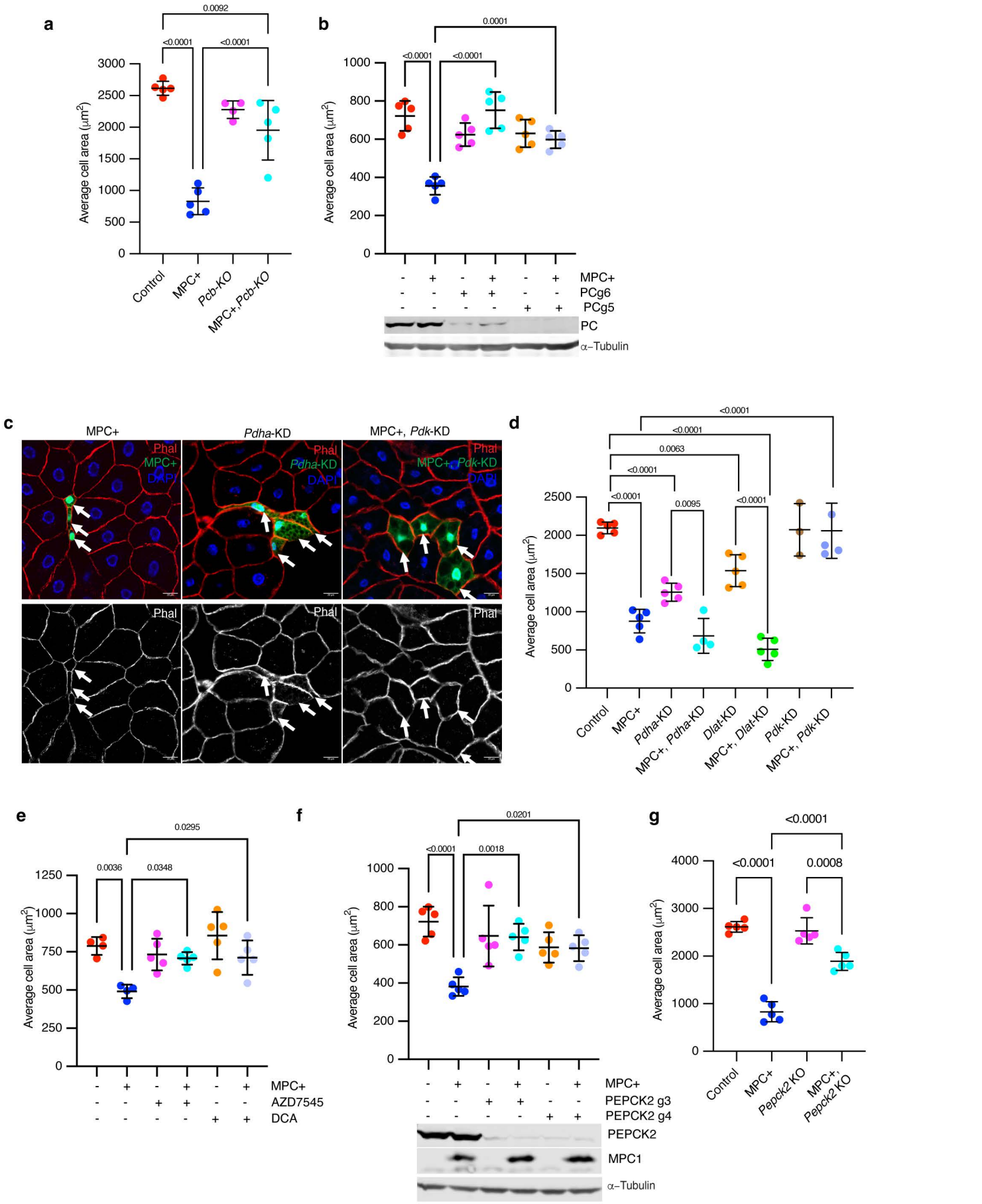


**Supplementary Figure 6 - Elevated mitochondrial pyruvate transport increases gluconeogenesis. (related to figure 4)**

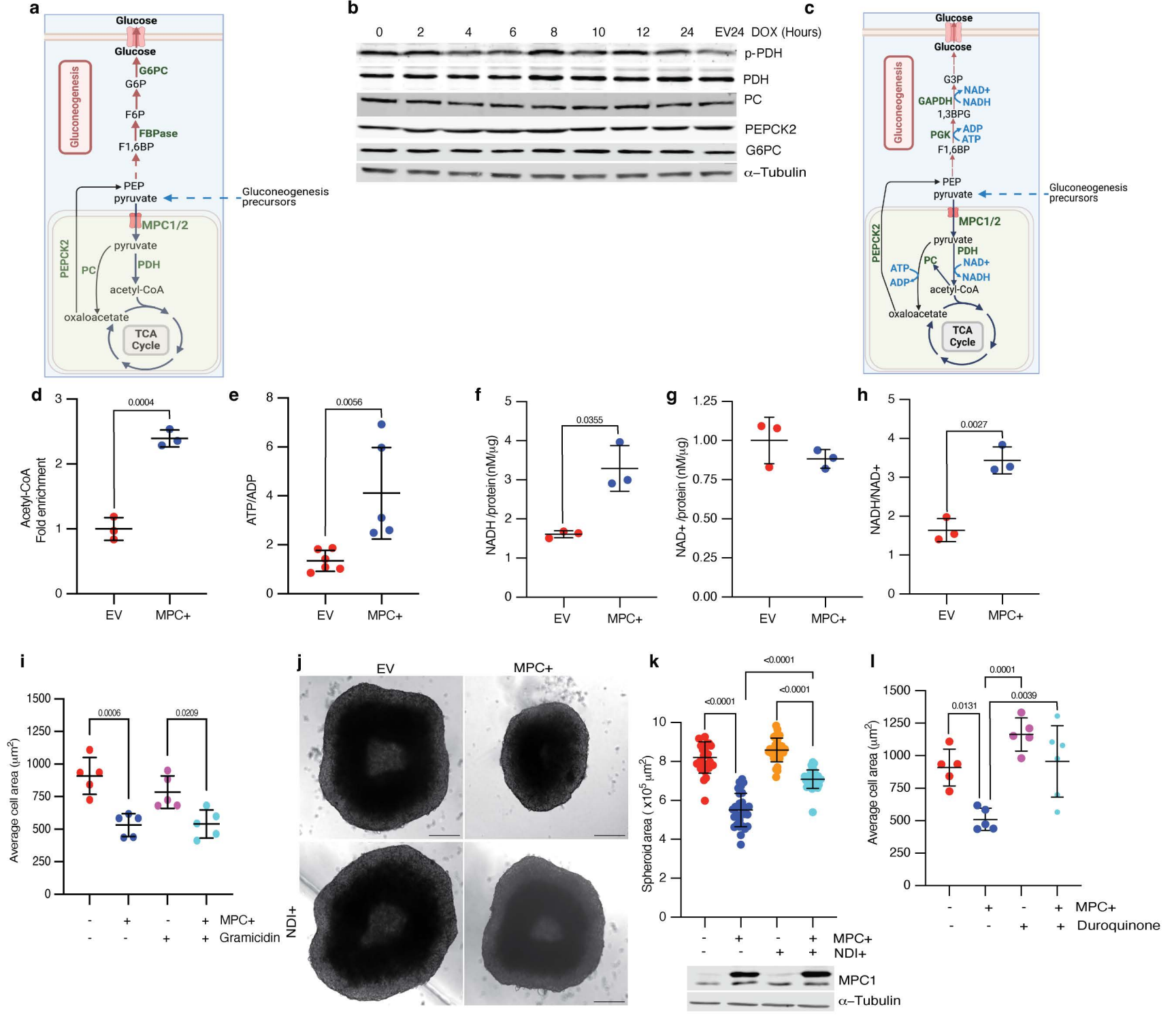


**Supplementary Figure 7 – Redox imbalance impedes protein synthesis and cell growth from elevated pyruvate metabolism in mitochondria. (Related to figure 5)**

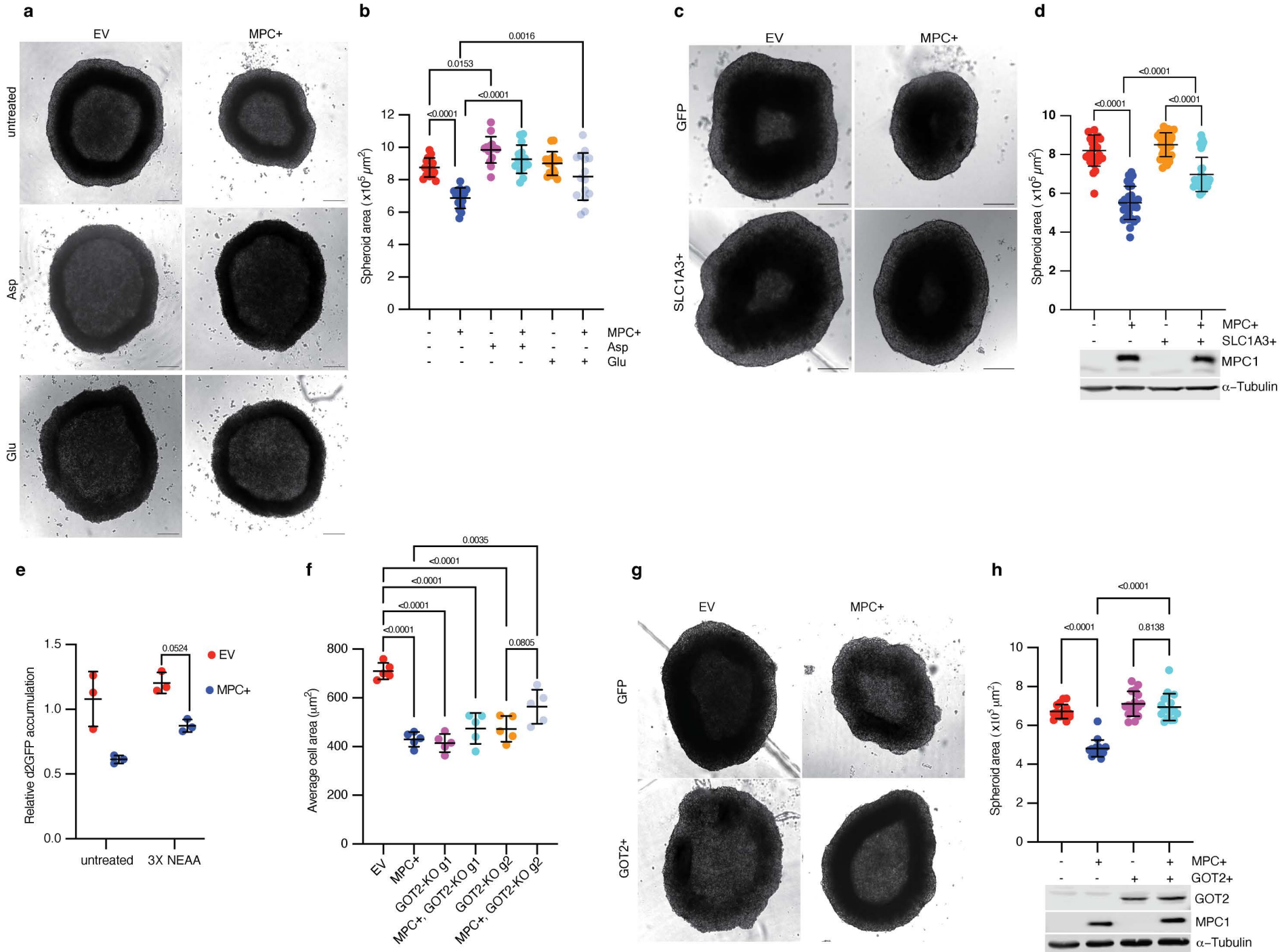


**Supplementary Figure 8 – Reduced aspartate-glutamate abundance impairs size of MPC-expressing cells. (Related to figure 6)**